Evaluation and Performance Prediction of a Wind Turbine Blade

by

Warrick Tait Pierce

Thesis presented in partial fulfilment of the requirements for the degree M.Sc. Engineering at the University of Stellenbosch

Supervisor: Prof. T.W. von Backström

Department of Mechanical Engineering

University of Stellenbosch

Stellenbosch, South Africa

December 2008

Declaration

I, the undersigned, hereby declare that the work contained in this thesis is my own original work and that I have not previously in its entirety or in part submitted it any university for a degree.

Signature:………………………………

         Warrick Tait Pierce

Date:……………………………………..

Abstract

The aerodynamic performance of an existing wind turbine blade optimised for low wind speed conditions is investigated. The aerodynamic characteristics of four span locations are determined from surface pressure measurements and wake surveys with a traversed five-hole probe performed in a low speed wind tunnel for chord Reynolds numbers ranging from 360,000 - 640,000.

Two-dimensional modelling of the wind tunnel tests is performed with the commercial computational fluid dynamics code FLUENT. The predictive accuracies of five eddy-viscosity turbulence models are compared. The computational results are compared to each other and experimental data. It is found that agreement between computational and experimental results varies with turbulence model. For lower Reynolds numbers, the Transitional-SST turbulence model accurately predicted the presence of laminar separation bubbles and was found to be superior to the fully turbulent models considered. This highlighted the importance of transitional modelling at lower Reynolds numbers. With increasing angles of attack the bubbles were found to move towards the leading edge and decrease in length. This was validated with experimental data. For the tip blade section, computations implementing the k-ε realizable turbulence model best predicted experimental data. The two-dimensional panel method code, XFOIL, was found to be optimistic with significantly higher lift-to-drag ratios than measured.

Three-dimensional modelling of the rotating wind turbine rotor is performed with the commercial computational fluid dynamics code NUMECA. The Coefficient of Power (C_P) predicted varies from 0.440 to 0.565 depending on the turbulence model. Sectional airfoil characteristics are extracted from these computations and compared to two-dimensional airfoil characteristics. Separation was found to be suppressed for the rotating case. A lower limit of 0.481 for C_P is proposed based on the experimental data.

Opsomming

Die aërodinamiese vertoning van 'n bestaande windturbine-vleuel wat geoptimeer is vir lae wind toestande word ondersoek. Die aërodinamiese eienskappe by vier posises langs die span van die lem word ondsoek deur oppervlakte drukmetings en naloop-opnames met 'n dwarsbeweegde vyfgat sensor uit te voer in 'n laespoed windtonnel vir koord-Reynoldsgetale wat strek van 360,000 tot 640,000.

Tweedimensionele modelering van die windtonneltoetse word uitgevoer met die kommersiële berekeningsvloeidinamika kode FLUENT. Die voorspelingsakkuraatheid van vyf-werwelviskositeitsturbulensie modelle word vergelyk met mekaar en met eksperimentele data. Daar word gevind dat ooreenstemming tussen berekende en eksperimentele resultate verskil met die turbulensiemodelle. Vir lae Reynoldsgetale het die oorgangs-SST turbulensiemodel die teenwoordigheid van laminêre wegbreekselle akkuraat voorspel. Dit het die belangrikheid van oorgangsmodellering uitgelig. Met toenemende aanvalshoek is gevind dat die wegbreekselle toenemend na die leirand beweeg en langer geword het. Dit is bevestig met eksperimentele data. Vir die lempuntseksie het berekeninge met die "k-ε-realizable" turbulensiemodel die eksperimentele meetings die beste voorspel. Daar is gevind dat die tweedimensionele paneelmetode kode, XFOIL, optimisties was, met beduidend hoër hef-tot-sleur verhoudings as gemeet.

Driedimensionele modellering van die roterende turbine rotor is uitgevoer met die kommersiële berekeningsvloeidinamika kode, NUMECA. Die voorspelde drywingskoëffisiënt, C_P, het gevariëer van 0.440 to 0.565, afhangende van die turbulensiemodel. Seksie-eienskappe van die vleuelprofiele word geneem uit die berekeninge en vergelyk met tweedimensionele vleuelprofiel-eienskappe. Daar is gevind dat wegbreking onderdruk is in die roterende geval. 'n Onderste limiet vir C_P van 0.481 word voorgestel gebaseer op die eksperimentele data.

Acknowledgments

Praise to the Lord Jesus Christ for He is worthy

Isaiah 53:5   But He was wounded for our transgressions. He was bruised for our iniquities; the chastisement for our peace was upon Him, and by His stripes we are healed.

Mark 12:33   "And to love Him with all my heart, with all my understanding, with all my soul, and with all my strength, and to love one's neighbour as oneself, is more than all the burnt offerings and sacrifices."

Proverbs 1:7   The fear of the Lord is the beginning of knowledge, but fools despise wisdom and instruction.

Proverbs 3:5-6   Trust in the Lord with all your heart, lean not on your own understanding; in all your ways acknowledge Him, and He shall direct your paths.

Our Father in heaven, hallowed be your name. Your Kingdom come. Your will be done on earth as it is in heaven. All glory and power to Him forever and ever. Amen

Contents

List of Tables

List of Figures

Nomenclature

Latin Symbols

A	area
a_c	axial induction factor limit
C_D	total drag coefficient
C_{D_f}	viscous drag coefficient
C_{D_p}	pressure drag coefficient
C_L	total lift coefficient
C_P	coefficient of power
C_p	pressure coefficient
c	blade chord
D	drag force
d	diameter
d_p	probe diameter
$E(\kappa)$	spectral energy
F_T	tangential force
H	shape factor
k	turbulent kinetic energy
k_s	surface roughness height
L_w	obstacle width
L	lift force
ℓ	characteristic length (length scale)
N_f	total normal force per unit length
P	pressure
Q_{EQS}	equi-angle skew
R	specific gas constant
Re	Reynolds number
r	radius
T	temperature
T_q	torque
T_f	total tangential force per unit length
t	thickness
U	mean velocity
u	instantaneous velocity
u'	fluctuating velocity component
V	free stream velocity

Greek Symbols

α	angle of attack
Δ	difference
δ	boundary layer thickness
ϵ	error
η	length scale of small eddies
θ	momentum thickness
ϑ	characteristic velocity
ε	rate of dissipation of turbulent energy
$\kappa = 2\pi/\lambda$	wavenumber
λ	wavelength
μ_t	turbulent viscosity
ν	kinematic viscosity
ν_t	turbulent kinematic viscosity
ρ	air density
Ω	rotational speed
ω	specific turbulence rate (turbulence frequency)

Subscripts

a	axial
rel	relative
t	tangential
te	trailing edge
w	wake
∞	free stream value

Abbreviations

2-D	two-dimensional
3-D	three-dimensional
AOA	angle of attack
BEMT	blade element momentum theory
CFD	computational fluid dynamics
CNC	computer numerical control
DES	detached eddy simulation
EFD	experimental fluid dynamics
GCI	grid convergence index

HAWT	Horizontal axis wind turbine(s)
LSSTQ	low speed shaft torque
N-S	Navier-Stokes
RANS	Reynolds-averaged Navier-Stokes
RSM	Reynolds stress model
S-A	Spalart-Allmaras
SST	shear stress transport
SU-M&M	Department of Mechanical Engineering, University of Stellenbosch

1. Introduction

The world's energy demands are increasing exponentially, due to, *inter alia*, the drastic human population increase and industrialization. These needs have in recent times been met with fossil fuel derivatives. Although conflicting estimates of fossil fuel reserves have been made, the fact remains that fossil fuels are depleting. This and the before mentioned increase in energy demands will lead to energy requirements not being met. Thus, the current energy generation setup is unsustainable.

Hence, a shift from the present dependency on fossil fuels needs to be taken. The shift should be towards a renewable form of energy; a sustainable solution. Large amounts of resources would be required. Conventional and proven nuclear power generation could be used as a work horse until renewable energy forms are sufficiently developed; in terms of both technology maturity and necessary production and implementation of renewable energy generation plants. Integration of these generation plants into the current electrical grid is another aspect that requires attention.

Additionally, recent global awareness has lead to the intensified promotion and development of renewable and sustainable energy technologies. These cleaner power generation technologies are sought to limit the adverse impact of power generation on the environment.

The following renewable energy forms, *inter alia*, have been identified: solar, hydro, wave and current, and wind. All these energy forms are significantly influenced by the sun. For instance, the generation of wind results from the uneven heating of the earth's surface by the sun and from the rotation of the earth on its own axis. Wind in turn generates waves. This dependency does not decree solar as the ultimate renewable energy form; for the respective harnessing capabilities need also to be considered.

The global installed wind energy capacity is rapidly increasing, Figure 1. This trend is predicted to continue. In South Africa specifically, the World Wind Energy Conference held in November 2003 in Cape Town asserted the imperative role of wind energy for future power generation, specifically in South Africa. The West Coast of South Africa has been identified as a viable location for wind farms

(grouping of wind turbines). This is evident with the erection of the 13 MW Darling wind farm and the upcoming establishment of another located near Vredendal.
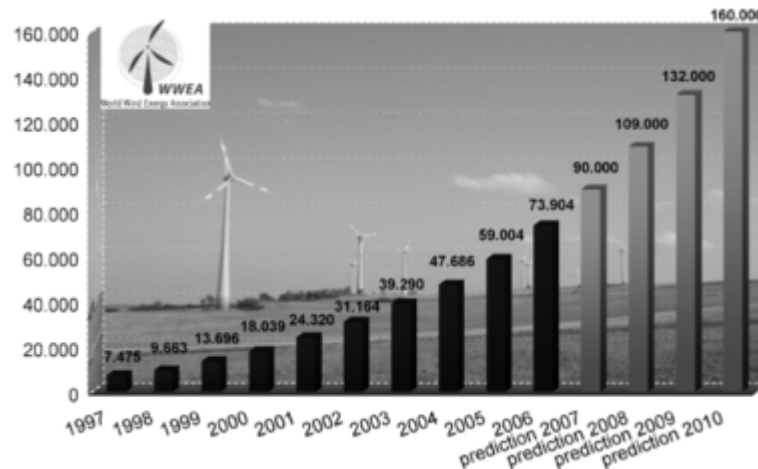
Figure 1: Installed wind energy capacity [MW] worldwide and prediction, © WWEA

1.1 Background to Wind Turbine Aerodynamics

In this section a few significant advancements in the development of wind turbine aerodynamics over the last century are presented.

In 1915, Lanchester [1915LAN] was first to predict the maximum efficiency of an ideal wind turbine of 59.3 % (16/27). In 1920 both the German scientist, Betz, and the Russian scientist, Joukowsky, derived this maximum efficiency independently of each other and unaware of the findings of Lanchester [2007GIJ]. Nevertheless, this limit is known as the Betz limit. The efficiency of a wind turbine is quantified with the coefficient of power , which is the ability of the wind turbine to extract energy from the free stream wind.

In 1935, a major break-through was achieved by Glauert [1935GLA], by formulating the blade element momentum method (BEMT). In BEMT, the wind turbine blade is divided into separate blade segments and analyzed from a two-dimensional perspective. Most prediction tools in industry are based on this method, with semi-empirical correlations to account for the three-dimensional effects, boundary layer separation, and unsteady flow conditions. These methods are beneficial in terms of their relatively low computational costs compared to computational fluid dynamics (CFD) simulations. The wind turbine performance predicted with BEMT has been found to be pessimistic compared to that encountered in the field [2002TAN]. Nevertheless, BEMT is widely applied in the wind turbine industry.

The discrepancies between BEMT predictions and field investigations results have been attributed to the effect of rotation on the wind turbine blade boundary layer distribution. Du and Selig [1999DU] concluded that the stall is postponed due to rotation and the separation point is delayed as a result of increasing rotational speed or decreasing blade spanwise position (refer to Section 4.1.6).

Recently, with the aid of current computing resources, advancements in the prediction of wind turbine aerodynamics have been achieved with the numerical solutions of the discretized Navier-Stokes and continuity equations. Earlier authors such as Wolfe and Ochs [1995WOL], and Ramsey *et al*. [1995RAM] focused on airfoil performance as a preliminary step to the computations of wind turbines. More recently, full Navier-Stokes computations of wind turbine rotors have been performed by several authors using different models and CFD codes [2004PAP], [2004JOH].

Reliable and detailed experimental data are necessary to assess the numerical results obtained. For this, large test campaigns have been conducted to collect experimental data, for instance the test campaign conducted in 2000 by the National Renewable Energy Laboratory (NREL) in the National Aeronautics and Space Administration (NASA) Ames wind tunnel and the European Union (EU)-funded project 'Mexico' in the Deutsch-Niederlandische Windanlage (German-Dutch Wind Tunnels).

Despite the advancements in the field of wind turbine aerodynamics, some of the most basic aerodynamic mechanisms governing the power output are not yet fully understood. The accurate prediction of wind turbine aerodynamics is still challenging [2002LEI]. This was clearly indicated with the initial modelling efforts by the international community, using the NREL measurements [2001FIN] as a reference. Results from the NREL blind comparisons were found to be extremely mixed [2001SIM], with considerable deficiencies noted between the predictions for blade loads and power output from the wind turbine, even for the simplest unyawed and unstalled operating conditions as shown in Figure 2. The results for power (torque) output ranged from a 60 % under prediction to more than a 150 % over prediction. Even using similar predictive methods with essentially the same medley of sub-component models, there were significant differences between the results. This suggests unresolved deficiencies in the models, perhaps even at a first-order level.

Numerical calculations of wind turbine aerodynamics have shown good agreement with experimental data. However, current state-of-the-art codes, cannot accurately predict highly separated wind turbine flow [2005TON], [2004JOH].

As mentioned, three-dimensional numerical computations of wind turbines have been performed. However, no literature on the evaluation of a wind turbine blade designed for low wind speed conditions was available at the time of writing.
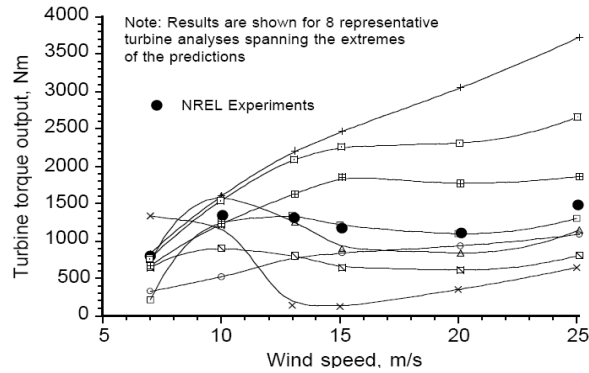
Figure 2: Representative "in the blind" predictions of turbine power output as a function of wind speed compared to experimental measurements [200LEI]

1.2 Research Problem and Objectives

According to a wind resource assessment executed by the Council for Scientific and Industrial Research (CSIR) and the Department of Minerals and Energy (DME), typical South African wind speeds are in the region of 4 to 7 m/s. However, these typical wind speeds present at the sites identified for wind farms in South Africa, such as the West Coast, are less than the typical wind speeds used to design horizontal axis wind turbines (HAWT). This is unfortunate for two reasons. Firstly as indicated by Equation (1.1), the power generation of a wind turbine is proportional to the free stream wind speed to the third power. Secondly the efficiency of HAWT decreases as it is not operating under design conditions. The focus of this study will be on the investigation of a proposed possible solution to the second point.

$$Power \propto Velocity^3 \qquad \qquad \text{(1.1)}$$

Cencelli masters' study [2006CEN] was done on the aerodynamic optimisation of a wind turbine blade for low wind speed conditions (summary given Appendix A). The primary aim of this study is to investigate the aerodynamic performance of the HAWT blade design of [2006CEN] at a low wind speed condition of 5.5 m/s. This can be formulated by two main objectives:

1. Obtain aerodynamic characteristics of the blade sections which constitute the proposed wind turbine blade
2. Predict the C_P of a wind turbine utilizing the proposed blade design at operating conditions

1.3 Thesis Outline

This section presents the basic layout of this thesis and provides a short description for each chapter. This report is divided into three main sections.

Section A: Introduction
In Chapter 1, a brief introduction to the field of renewable energy, specifically HAWT for wind energy generation is given. The research problem and objectives, and the thesis outline are also described. Key concepts in the form of drag prediction methods and turbulence is presented in Chapter 2 to provide a basis for this thesis.

Section B: Modelling
The experimental work of the two-dimensional wind tunnel testing of the blade sections is presented in Chapter 3. The findings of this chapter in the form of the aerodynamic characteristics are used to validate the CFD findings of Section 4.1. Section 4.2 considers the numerical modelling of the three-dimensional HAWT used to predict C_P.

Section C: Data Presentation and Discussion
This section presents the results, conclusions and recommendations that stem from the work done in this thesis.

2 Key Concepts

2.1 Drag Prediction Methods

This section begins with the formulation of aerodynamic force followed by the presentation and assessment of drag prediction methods typically implemented by CFD code. The methods used to calculate drag from experimental data are presented in Section 3.3.6

A fluid flowing past a body causes the fluid to divert from its original path, such deflections lead to changes in the pressure and the velocity of the fluid. These deflections are visualized with smoke techniques as seen in Figure 3, below.
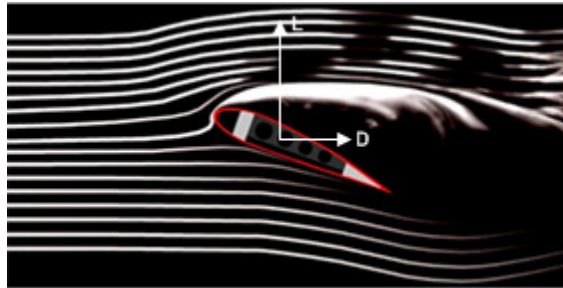
Figure 3: Streamlines past an airfoil visualized by smoke techniques

Frictional forces which resist the flow of the fluid result from the viscosity of the fluid. This force and the force arising from the pressure over the surface of the body is collectively the resultant force exerted by the fluid on the body, known as the aerodynamic force.

The aerodynamic force is customarily resolved into two orthogonal components that are directionally referenced to the free stream velocity:

- Drag - component parallel to the direction of the relative motion
- Lift - component perpendicular to the direction of the relative motion

The lift (L) and drag (D) force components are depicted in Figure 3.

Recently, CFD has achieved significant progress owing to advances in numerical schemes and computing resources. However, the accurate drag prediction in CFD is still a major challenge as shown at the meeting of AIAA Drag Prediction Workshop [2004HEM]. Hence, the remainder of this section will be dedicated to the discussion of drag prediction methods used to compute the drag components. In Figure 4, the drag prediction methods (shown in italics) decompose the total drag into the corresponding components.
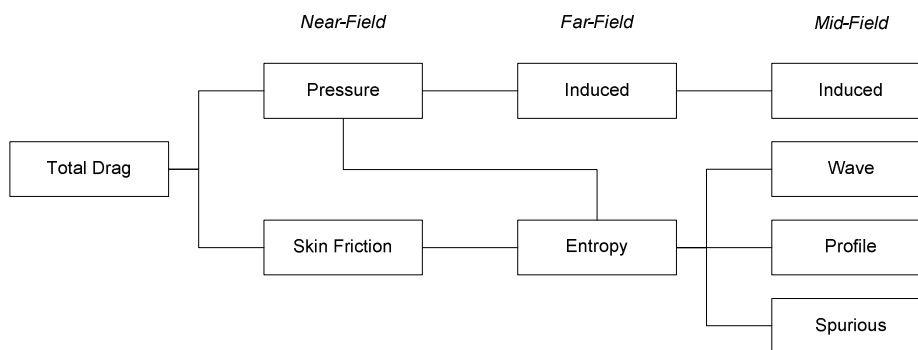
Figure 4: Drag components and the classification of drag prediction (top)

The wave drag is associated with the formation of shock waves in high-speed flows; transonic and supersonic flow. The profile drag is defined as a drag component based on the entropy production due to the effect of the boundary layer and the wake.

The three drag prediction methods in Figure 4 will now be presented with the focus on the Near-Field Method as it is utilized in the CFD computations of Chapter 4. With the following section reference was made to [2006YAM].

2.1.1 Near-Field Method

Traditionally, surface integration of the pressure and stress tensor on the surface of the body, which is called the 'Surface Integration' or 'Near-Field Method' is used for lift and drag force prediction in CFD computations. However, it has been shown that the computed total drag utilizing this method includes inaccuracies (spurious drag) relating to numerical diffusion and error, and that it is not possible to isolate these inaccuracies.

2.1.2 Far and Mid-Field Methods

Recently, two advanced drag prediction methods based on the theory of momentum conservation around the body have been presented, namely the 'Wake Integration' or 'Far-Field Method', and 'Flow-Field Integration' or 'Mid-Field Method'. Both the far and mid-field methods are closely related to the surface integration techniques (near-field) and all three are derived from momentum integral theory.

The far-field method computes drag components by means of the surface integration on the wake plane downstream of the body.

The mid-field method is derived from the far-field method by applying the divergence theorem, also known as the Gauss' theorem. This method computes the drag components from volume integration around the body. The spurious drag component, which is due to the spurious entropy production based on numerical diffusion, can be computed and isolated from the total drag; enabling more accurate drag prediction. Yamazaki *et al.* investigated the influence of the mesh resolution on the drag predictions of the mid-field method. It was found that the physical drag components are almost independent of the mesh resolution [2008YAM] as can be seen in Figure 5, below.
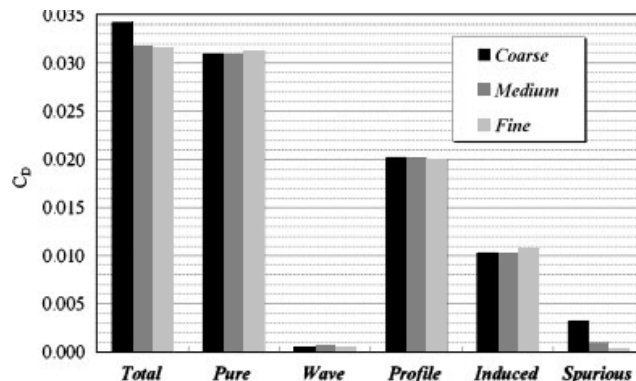
Figure 5: Comparison of drag components of DLR-F6 wing-body configuration with the mid-field method [2008YAM]

2.1.3 Assessment of Performance

Near and far field methods should ideally produce the same values for the lift and the drag forces. However, numerical approximations may render the results differently.

An advantage of the far field method is that more details on the sources of the drag are provided; decomposed into components that correspond to the physical sources of drag. This information can

assist in minimizing drag and understanding the design tradeoffs involved between the various physical components of drag.

Choa and Dam [2006CHA] implemented the far field method to predict the aerodynamic characteristics of three-dimensional wings in viscous subsonic and transonic flows. They concluded that in all cases the lift coefficients predicted by far and near field methods are in excellent agreement, and for the drag coefficients good agreement is achieved between integration methods.

2.2 Turbulence

Firstly a general description of the physics and nature of turbulence is given, followed by the presentation and brief assessment of numerical methods used to simulate the effects due to turbulence. With the following section reference was made to [2007VER], [1994WIL] and [1993SCH].

2.2.1 Basic Description

Virtually all flows of practical engineering interest are turbulent. In 1937, Taylor and von Kármán proposed the following definition of turbulence: " Turbulence is an irregular motion which in general makes its appearance in fluids, gaseous or liquid, when they flow past solid surfaces or even when neighbouring streams of the same fluid flow past or over one another" [1938GOL].

The instantaneous velocity is decomposed into a mean and a fluctuating part:

$$u(x, y, z, t) = U(x, y, z) + u'(x, y, z, t)$$
(2.1)

This is called Reynolds decomposition. The fluctuations in a turbulent flow are random and are not correlated with the boundary conditions. The ratio of the root-mean-squared value of u' and the mean velocity is known as the turbulence intensity. The average value of u' is zero.

The irregular variations in the motion are not necessarily small with respect to either time or space. For instance, the instantaneous velocity fluctuations in the wake of a bluff body can be in the order of magnitude of the free stream velocity.

Careful analysis of solutions of the Navier-Stokes (N-S) equations, or more typically of its boundary-layer form, show that turbulence develops as an instability of the laminar flow. For a real (i.e. viscous) fluid, the instabilities result from interaction between the N-S equation's non-linear inertial and viscous terms.

Hence, the type of flow (laminar or turbulent) is strongly influenced by the Reynolds number of the flow. The interaction is very complex because it is rotational, fully three-dimensional and time dependent.

In principle, the time dependent, three-dimensional N-S equations contain all the physics of a given turbulent flow. Unfortunately an analytical solution of the non-linear N-S equation has eluded science. Turbulence remains the most noteworthy unsolved scientific problem of the twentieth and the twenty-first century.

Some insight into the reasons for the intractability of the N-S is given when considering the most significant characteristics of turbulent flow, as proposed by Schetz [1993SCH]. These characteristics are presented as sub-headings.

2.2.1.1 Turbulent Eddies

There is a general swirling motion of the flow, involving indistinct lumps of fluid known as eddies. An eddy can be defined as a local swirling motion with the local turbulence scale as its characteristic dimension. There is a wide range in the size of eddies occurring at the same time or at the same place. Eddies can have length scales which are comparable to the flow boundaries or be of intermediate and small size.

Vortex stretching is the process by which the largest turbulent eddies interact with and extract energy from the mean flow. The presence of mean velocity gradients in sheared flows distorts the rotational turbulent eddies. Suitably aligned eddies are stretched as one end is forced to move faster than the other.

The characteristic velocity ϑ and length ℓ of the larger eddies are of the same order as the velocity scale U and length scale L of the mean flow. From this and as the kinematic viscosity is essentially constant throughout the flow field (assuming constant flow medium temperature), the large eddies are dominated by the inertia effects and the viscous effects are negligible (high Reynolds number). Therefore, the large eddies are effectively inviscid.

Hence angular momentum is conserved during vortex stretching. This causes the rotation rate to increase and the radius of their cross sections to decrease. Thus the process creates motions at smaller traverse lengths and smaller time scales. The energy which maintains the turbulence is provided by the stretching work done by the mean flow on the large eddies during these events. Turbulence features a cascading process whereby kinetic energy is transferred from larger to smaller eddies. Smaller eddies are stretched strongly by somewhat larger eddies and more weakly by the mean flow. Ultimately, the smallest eddies' (with length scales known as Kolmogorov microscales) kinetic energy dissipate into heat through the action of molecular viscosity. Thus, turbulent flows are dissipative. This dissipation results in increased energy losses compared to laminar flow. The rate of production of turbulent flow has to be broadly in balance with the rate of dissipation to prevent unlimited growth of the turbulence energy.

The spectral energy $E(\kappa)$ as a function of the wavenumber $\kappa = 2\pi/\lambda$, where λ is the wavelength of the eddies is presented in Figure 6. The spectral energy $E(\kappa)$ is the kinectic energy per unit mass and per unit wavenumber of fluctuations around the wavenumber κ. The figure shows that the larger eddies are the most energetic and the smallest eddies have the lowest energy content.

On dimensional grounds, the spectral energy of the large eddies are given by $E(\kappa = 1/\ell) \propto \vartheta\ell^2$ [1972TEN]. Since the length scale ℓ is related to the length scale of turbulence producing processes, for example the boundary layer thickness δ, obstacle width L_w, surface roughness height k_s, the structure of the largest eddies is highly anistropic (directional) and strongly affected by the boundary conditions.

Figure 6: Energy spectrum of wave turbulence behind a grid [2007VER]

The structure of the smallest eddies, hence, their spectral energy $E(\kappa)$ is only dependent on the rate of dissipation of turbulent energy ε and the kinematic viscosity of the fluid ν, as shown by dimensional analysis: $E(\kappa = 1/\eta) \propto \nu^{5/4}\varepsilon^{1/4}$. The diffusive action of viscosity tends to smear out directionality at small scales. Therefore, at high mean Reynolds numbers the smallest eddies in a turbulent flow are isotropic (non-directional).

2.2.1.2 Unsteady

Turbulence is unsteady. A deterministic approach to the problem is not possible as turbulence is characterised by random fluctuations. Statistical methods are implemented resulting in statistical correlations in the equations of motion that cannot be determined *a priori*. This is known as the closure problem.

2.2.1.3 Instantaneous Boundary

The instantaneous boundary between the turbulent region and the non-turbulent, outer, inviscid flow is sharp. The position of the edge of the turbulent zone is determined by the (time dependent) passage of individual large eddies. Near this edge the larger eddies occasionally penetrate into the surrounding region. During the resulting bursts of turbulent activity in the outer region – known as intermittency – fluid from the surroundings is drawn into the turbulent zone. This process is termed entrainment and is the main cause of the spreading of turbulent flows (including wall boundary layers) in the flow direction.

2.2.1.4 Three-Dimensional

Turbulence is three-dimensional. Even in flows where the mean velocities and pressures vary in only in one or two space dimensions, turbulent fluctuations always have a three-dimensional spatial character.

Perhaps the most important feature of turbulence from an engineering perspective is its enhanced diffusivity. This is achieved by the effective mixing by the eddying motions in turbulent flow. Turbulent diffusion. On the other hand, as mentioned, dissipation results in increased energy losses.

Additional stresses on the fluid, known as the Reynolds stresses, are induced by the velocity fluctuations. Apparent stresses often develop in turbulent flows that are several orders of magnitude larger than in corresponding laminar flows.

2.2.2 Models

Numerical methods have been developed to attempt to simulate the effects due to turbulence. The models for the Reynolds stress terms can be grouped into three main categories. These categories are used as sub-headings and presented in order of increasing required computational costs. Section 2.2.2.1 will be the focus of this section as the turbulence models used in this investigation are from this group. The latter two will only be briefly discussed.

2.2.2.1 Turbulence models for Reynolds-averaged Navier-Stokes (RANS) equations

Extra terms (Reynolds stresses) appear in the Reynolds-averaged flow equations due to interactions between various turbulent fluctuations. These equations are called the Reynolds averaged Navier-Stokes (RANS) equations. These extra terms are modelled with classical turbulence models, amongst others: the k-ε model and the Reynolds stress model (RSM).

A common approach to modelling the Reynolds stresses is to apply the Boussinesq hypothesis [1975HIN] to relate the Reynolds stresses to the mean velocity gradients. These turbulence models are known as eddy-viscosity turbulence models. The advantage of this approach is the relatively low computational cost associated with the computation of the turbulent viscosity μ_t. In the case of the Spalart-Allmaras model, one additional transport equation for the kinematic turbulent viscosity ν_t is solved. For the k-ε and k-ω models, two additional transport equations for the turbulent kinetic energy k and either the rate of dissipation of turbulent energy ε or the specific turbulence rate (turbulence frequency) ω are solved.

The disadvantage of the Boussinesq hypothesis is that μ_t is assumed to be an isotropic scalar quantity which is strictly not true. An alternative approach, embodied in the RSM, is to solve transport equations for each of the terms in the Reynolds stress tensor. An additional scale-determining equation is also required; resulting in five and seven additional transport equations for two and three-dimensional flows, respectively. RSM is clearly superior for situations in which the anisotropy of turbulence has a dominant

effect on the mean flow. Such cases include highly swirling flows and stress driven secondary flows [2006FLU].

RANS turbulence models are classified on the basis of the number of additional transport equations that need to be solved in addition to the RANS flow equations. Some of these models are indicated in Table 1. The respective length ϑ and velocity scales ℓ, and the formulation of μ_t are also presented in the table below, where $f_{v1} = f_{v1}(\nu_t/\mu_t)$ is the wall damping function, which tends to unity for high Reynolds numbers and is zero at the wall and C_μ is a dimensionless constant.

Table 1: Classification of turbulence models (RANS)

No. of additional transport equations	Name of model	ϑ	ℓ	μ_t
One	Spalart-Allmaras	n/a	algebraic	$\rho \nu_t f_{v1}$
Two	$k\text{-}\varepsilon$	$\sqrt{k}$	$\dfrac{k^{\frac{3}{2}}}{\varepsilon}$	$\rho C_\mu \dfrac{k^2}{\varepsilon}$
	$k\text{-}\omega$	$\sqrt{k}$	$\dfrac{\sqrt{k}}{\omega}$	$\rho \dfrac{k}{\omega}$

In 1992, Mentor [1992MEN] proposed a hybrid model using (i) a transformation of $k\text{-}\varepsilon$ model into a $k\text{-}\omega$ model in the near-wall region as the performance of the $k\text{-}\varepsilon$ model in the near-wall region for boundary layers with adverse pressure gradients is unsatisfactory and (ii) the standard $k\text{-}\varepsilon$ model in the fully turbulent region far from the wall as the results of the $k\text{-}\varepsilon$ model are less sensitive than the $k\text{-}\omega$ model to the assumed (arbitrary) values in the free stream. This model is known as the $k\text{-}\omega$ SST model. Mentor *et al.* [2003MEN], based on experience with the model in general purpose computation, summarised a series of modifications to optimise the performance of the $k\text{-}\omega$ SST model.

The remainder of this section deals with the assessment of the performance of turbulence models for RANS equations.

Benjanirat and Sankar [2003BEN] investigated the performance of four turbulence models for the prediction of wind turbine aerodynamics, namely the Baldwin-Lomax (zero-equation model), the Spalart-Allmaras and the $k\text{-}\varepsilon$ model with and without wall corrections. They concluded that the $k\text{-}\varepsilon$ model with Gorski near wall effects [1986GOR] gave the best agreement with measurements. They also remarked that the prediction of the transition point is expected to play a crucial role in power prediction (transition model effects were not investigated in their study).

2.2.2.2 Large eddy simulation (LES)

LES involves space filtering of the unsteady N-S equations prior to the computations. The filter pass the larger eddies and rejects the smaller eddies. The larger eddies are computed exactly and the rejected smaller eddies are modelled by means of a sub-grid scale model.

2.2.2.3 Direct numerical simulation (DNS)

The unsteady N-S equations are solved; the mean flow and all the turbulent velocity fluctuations are computed. Computations are performed on a sufficiently fine spatial grid which is able to resolve the Kolomogorov microscales and with time steps sufficiently small to resolve the period of the fastest fluctuations.

The drag prediction methods and the numerical methods used to model turbulence implemented in CFD have been discussed. This provides a basis for the CFD work of Chapter 4.

SECTION

B

Modelling

Increasingly CFD is becoming a vital component in the design of industrial products and processes [2007VER]. One of the advantages of CFD over EFD is the potential reduction of time and cost. Results obtained from CFD models should be validated; this is a large subject of discussion and investigation [2008HOU], [2007VAL].

CFD can be a useful tool to establish, *inter alia*, the flow behaviour of the fluid, but when applied incorrectly or in unusual cases, the results could be misleading.

The analysis program XFOIL was incorporated within the two-dimensional optimisation of blade sections of the base study. XFOIL is an interactive program for the design and analysis of subsonic, isolated airfoils. The XFOIL results obtained need to be validated. Hence, two-dimensional wind tunnel tests (EFD) of the four blade sections of [2006CEN] are performed (Chapter 3). The processed data of these tests are compared to the corresponding two-dimensional CFD modelling (Section 4.1) results. This in turn validates the CFD code. In order for good comparison, equivalence between the two-dimensional CFD models and wind tunnel tests needs to be attained.

However, the ultimate goal of this project is to predict the performance of the wind turbine rotor model supplied by the base study. This is a three-dimensional problem and is simulated as such with CFD (Section 4.2). Unfortunately there was no experimental data to verify the results, as it was beyond the project's scope to perform the required wind tunnel tests of the three dimensional wind turbine model.

3. Experimental Fluid Dynamics (EFD)

This chapter describes the equipment and methods used to obtain the two-dimensional EFD results required to verify the corresponding two-dimensional CFD modelling results.

3.1 EFD Models

For the wind tunnel tests a two-dimensional model for each of the four wind turbine blade sections needed to be manufactured. This section discusses the factors that are considered. These factors are shown in Figure 7. The *wind tunnel, setup* and *testing* steps are dealt with in Section 3.3.

The factors are inter-dependent. For instance the type of material would dictate the dimensions of the material which in turn influences the scaling factor and *vice versa*. Therefore the situation was dealt with as a whole. The testing of the model(s) was the ultimate goal of this section. For this discussion the prerequisite steps are dealt with in an input/output manner as displayed in Figure 7. The same process was followed for all four blade sections and therefore will only be considered once.
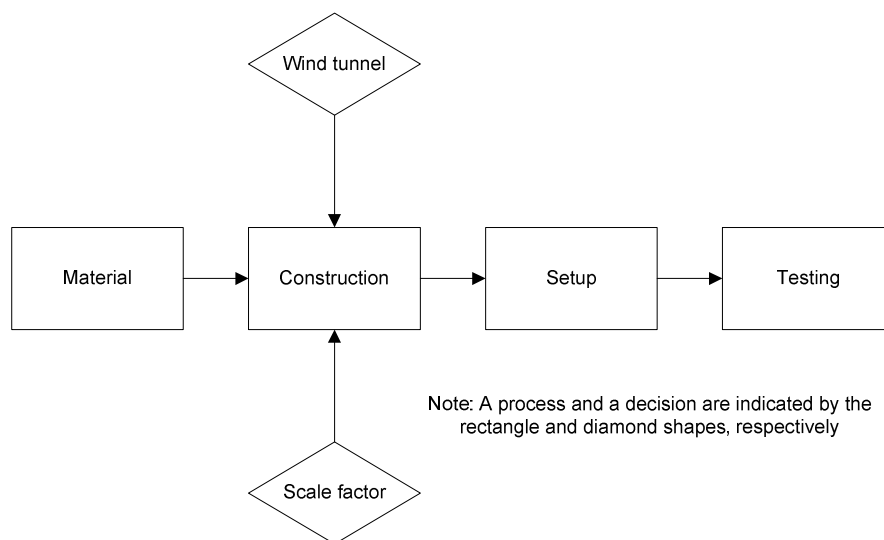
Figure 7: Flowchart of the construction process of the EFD model(s)

3.1.1 Material

The *material* step is a not only a physical input into the machining technique but also a decision and process in terms of the selection and preparation thereof, respectively. The selection of the material is now considered. The three materials considered are aluminium, wood and PVC (polyvinyl chloride). PVC was eliminated as it was noted from a previous study that the surface finished produced from the proposed machining technique (CNC) was unfavourable.

Aluminium is predominately the material of choice for airfoil models as it has favourable properties in terms of, *inter alia*, machinability and surface finish. Wood was however selected as it too has both these favourable properties and is more affordable in terms of lower material and machining costs (quicker feed rate resulting in lower operational time of machine, and less cutter wear).

Jelutong is the species of wood selected as it is considered suitable for model making. The maximum thickness and width available from the supplier is 60 and 300 mm, respectively.

3.1.2 Selection of Model Size (Scaling Factor)

Factors that are used to determine the scaling factor(s) of the two-dimensional blade sections

- The appropriate Reynolds number(s), at which XFOIL simulations were computed by Cencelli [2006CEN] for the respective blade section should be adhered to.
- The wind tunnel which is to be utilized has an approximate wind speed range between 15 and 100 m/s.
- Turntable insert to be used in wind tunnel has a diameter of 490 mm. It was decided that for simplification of the setup within the wind tunnel this diameter value would be taken as maximum chord length of the blade sections.
- Maximum amount of allowable blockage was taken as 7.5 percent [1999BAR].
- At least an angle of attack in the range of 15 to 20 ° should be able to be tested as to ensure stall of the airfoil.
- Thickness and chord length of models are limited by material dimensions.
- Maximum chord length, due to material availability width, is taken as 300 mm.
- From a previous project [2004ECK] it was shown that a chord length of 265 mm and thickness of 32 mm provided sufficient space for installation of required static pressure taps. A minimum chord length and thickness of 200 and 30 mm, respectively was stipulated.

With these factors the scale factors for the models are determined. Detailed calculations are presented in Appendix B.1. It was found that the material width was the limiting factor. Therefore, it was decided that the chord length of models would be slightly less than the material availability width; 290 mm. The

10 mm difference allowed for the clamping of the work piece during machining. When considering the allowable blockage the maximum allowable angle of attack for all four blade sections is 21 °. This is more than the specified 20 ° and therefore satisfactory. Respective scale factors are presented in Table 2, below.

Table 2: Blade sections scaling data

Section	Scale factor	V [m/s]	Thickness [m]
Root	0.408	17.5	0.058
Mid	0.636	23.1	0.048
Semi	0.773	27.6	0.044
Tip	0.866	31.2	0.047

3.1.3 Model Concepts

Before manufacturing could commence a concept for the EFD model(s) needed to be developed. The main requirements of the concept are:

- Enclose pressure orifices (flush orifices on blade surface). This includes necessary piping from points to pressure measuring devices.
- Comply to machining techniques.
- Able to be setup in wind tunnel.
- Withstand forces during wind tunnel testing.
- Minimal vibrations during data logging.

Numerous concepts were considered. A model to be manufactured from three parts, namely one middle and two sides with the interface of parts along the chord (see Figure 14), fulfilled the relevant requirements. Two support rods were used to both join the three parts of the blade section and provide structural rigidity during testing.

3.1.4 Construction

Numerous airfoil blades, both two- and three dimensional, have been manufactured at the Department of Mechanical Engineering, University of Stellenbosch (SU-M&M) [2006COE], [2004ECK]. These previous

tasks were achieved by implementing computer numerical control (CNC) manufacturing technology. The Leadwell VMC40 numerically controlled milling machine is also used in this project.

The requirements, setup and operation of this machine with regards to the manufacturing of the EFD model(s) will now be discussed.

3.1.4.1 Requirements

As mentioned, the coordinates for all four blade sections are provided. The trailing edges of models were modelled with a zero thickness. This is not possible in terms of manufacturing especially considering the model material is wood. A rounded (half circle) trailing edge type with a finite thickness is preferred. Considering the manufacturing techniques and model material the trailing edge thickness is selected for all four blade sections as 2 mm. A Matlab © program was written with the coordinates of the respective blade sections and required trailing edge thickness as inputs. The output of the program is a text file with the coordinates of the blade sections with adapted trailing edges.

Professor A.H. Basson from the SU-M&M developed the program NCBlade which generates CNC codes required to machine a blade profile for a 3-axis CNC machine. This program with the adapted blade sections' coordinates as inputs is implemented to generate the NC input programs for the CNC machine. The blade sections surfaces are cut with a 12 mm round nose cutter.

3.1.4.2 Preparation

The wood is squared with a milling machine. The work piece is then clamped onto the bed of the CNC machine. The machine is zeroed in the x-y direction and finally the cutter height (z direction) above the work piece is set.

3.1.4.3 Operation

The actual cutting of work piece is fully automatic. An initial rough-cut removes most of the waste. A secondary finer-cut is implemented to ensure a good surface finish. Total cutting time for one blade section is about five hours. The 1 mm holes for the static pressure taps are drilled perpendicular to the surface by hand as it was not feasible to perform this task with the CNC machine.

Care was taken to ensure a good surface finish (smooth) of the models.

3.2 Flow Measurement: Five Hole Probe

A five-hole-probe is used to capture wake survey data for the two-dimensional wind tunnel testing. In this section a brief introduction to flow measurement is given, followed by the description of the calibration process of the probe. Then the possible sources of error with regards to flow analysis with the probe are given. Lastly, the method by which the calibration data is implemented for the two-dimensional wind tunnel testing is discussed.

3.2.1 Introduction to Flow Measurement

Measurement of flow at a specific point in a known direction is simply performed by noting the difference between the total and static pressure at that point. This is traditionally performed with a Pitot-static tube which gives the dynamic pressure directly by measuring the difference between the total and static pressure. The total pressure is measured with the hole at the stagnation point of the probe and the static pressure is measured with two or more holes on the walls (no-slip condition which dictates zero velocity at the wall and thus total pressure is equal to static pressure) of the second tube which is coaxial to the Pitot tube.

Measurement of flow at a specific point in an unknown direction is achieved with the use of a probe with multiple pressure taps with angles relative to each another. For two-dimensional- and three-dimensional flow a three-hole probe and five-hole probe could be used respectively. It was decided to utilize a five-hole probe as to investigate if the flow is essentially two-dimensional. The actual forward facing cone five-hole probe used is shown in Figure 8. The diameter of the probe is 4 mm.

(a)   (b)
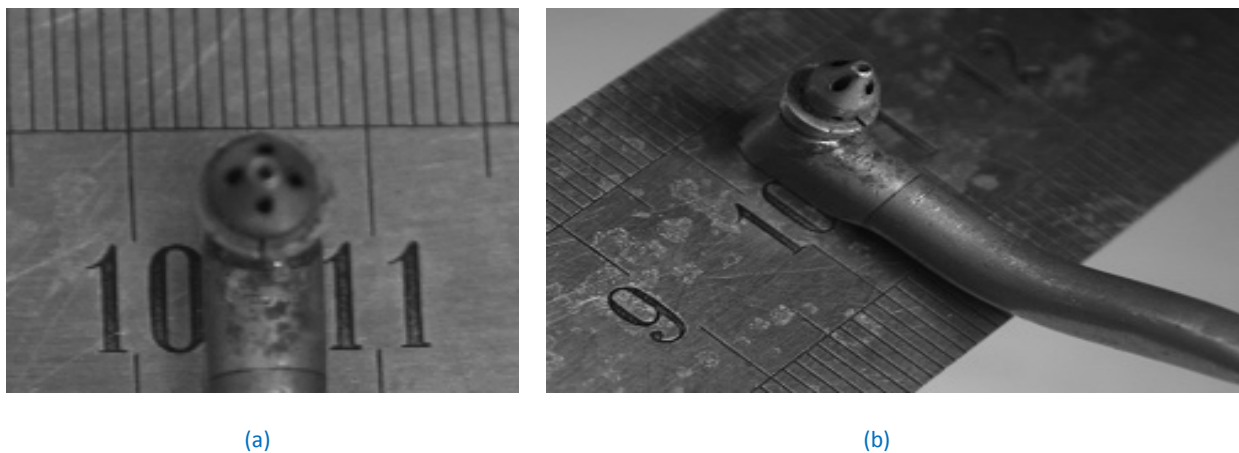
Figure 8: Five-hole probe used for two-dimensional wind tunnel tests as seen from (a) front and (b) below-side

3.2.2 Calibration

This section describes the experimental procedure required to calibrate the five-hole probe which is used for the two-dimensional wind tunnel tests. The objectives, instrumentation and finally the procedure of the five-hole probe calibration are dealt with individually.

3.2.2.1 Objectives

The required measurements for the calibration of the five-hole probe from the experiment are:

- Pressure readings of each of the five holes of the five-hole probe.
- Pressure readings from the Pitot-static tube.
- True relative flow angles.

A diagram of the test setup is shown in Figure 9. The positive pitch- and yaw angles as well as the hole numbering are indicated Figure 10.

3.2.2.2 Instrumentation

The necessary instrumentation to acquire required measurements is listed:

- Small wind tunnel.
- Adjustable mounting bracket for probe in small wind tunnel.
- Five-hole probe.
- Pitot-static tube.
- Computer with ADDA (Analogue to Digital/Digital to Analogue) card.
- Dedicated pressure transducers for each channels.

3.2.2.3 Experimental Procedure

The motor of the small wind tunnel is started and set to maximum operational speed (50 Hz). The resultant wind speed in the test section is approximately 36 m/s.

The mounting bracket is adjusted to the desired pitch- and yaw angle. All possible combinations within the extremities of ±20° (both pitch- and yaw angle) with 5° increments are tested. For each configuration the data of the seven channels (five for the five-hole probe and two for the Pitot-static tube) are recorded via the dedicated pressure transducers and the ADDA card. The pressure of the front hole of the probe (number 1 of Figure 10) is measured relative to atmosphere. The other holes' pressures are measured relative to number 1. The sampling rate and interval were 1 kHz and 1s, respectively.
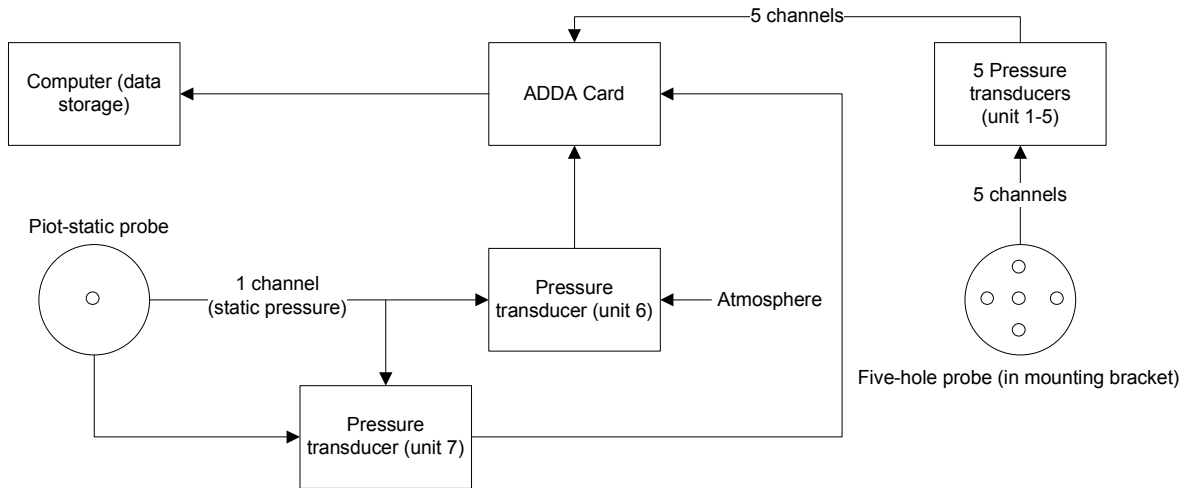
Figure 9: Arrangement of the data acquisition system used for calibration of five-hole probe

3.2.2.4 Data Analysis

The following section illustrates the analysis procedure and the equations used to convert the experimental data obtained into relevant data which is to be incorporated into the two-dimensional wind tunnel testing of the blade sections.

With the use of the individual calibration curves of the seven pressure transducers the stored experimental data is converted into relevant pressures. The pressure transducers were calibrated with a Betz water manometer. From these pressures, pressure coefficients are calculated for a range of pitch- and yaw angles. Wright [1970WRI] defined the pressure coefficients for the five-hole probe by means of Equations (3.1) to (3.5), below.
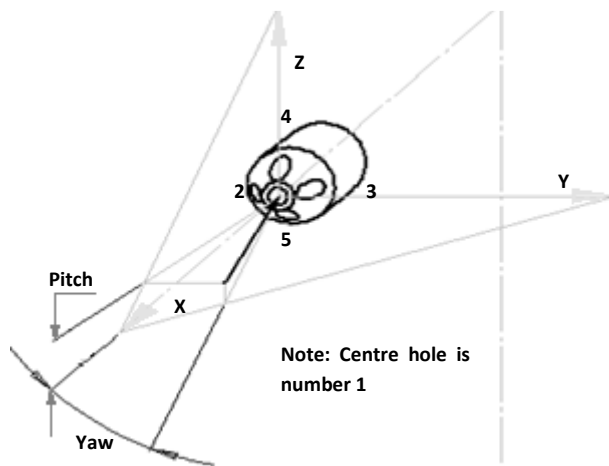
Figure 10: Hole and flow angle nomenclature of five-hole probe

$$\bar{P} = \frac{P_2 + P_3 + P_4 + P_5}{4} \tag{3.1}$$

$$C_{P_{centre}} = \frac{P_1 - P_{stat,pitot}}{P_{tot,pitot} - P_{stat,pitot}} \tag{3.2}$$

$$C_{P_{average}} = \frac{\bar{P} - P_{stat,pitot}}{P_{tot,pitot} - P_{stat,pitot}} \tag{3.3}$$

$$C_{P_{yaw}} = \frac{P_2 - P_3}{P_1 - \bar{P}} \tag{3.4}$$

$$C_{P_{pitch}} = \frac{P_4 - P_5}{P_1 - \bar{P}} \tag{3.5}$$

Here $P_{stat,pitot}$ and $P_{tot,pitot}$ are the static and total pressures, respectively measured upstream (without affecting the measured flow) of the model with a Pitot-static tube, respectively.

Calibration maps of the pressure coefficients are generated over the range of pitch- and yaw angles.

3.2.3 Sources of Errors

Sources of errors in the conventional-probe measurement of the relative flow were described by Siteram *et al.* [1981SIT]. The relevant errors to this project are presented and briefly discussed.

3.2.3.1 Turbulence effects

It should be noted that the five-hole probe used in this project was calibrated in a different wind tunnel to the wind tunnel used for subsequent experiments. The flow turbulence (turbulence intensity) of the small wind tunnel differs from the large wind tunnel. Turbulence is also generated by the models presence in the flow field.

Goldstein [1936GOL] theoretically investigated the direct effect of the turbulent velocity components on the pressure probe measurement. This analysis was modified by Siteram *et al.* [1981SIT]. With assumptions, it is shown that for a turbulence intensity of 10 %, the estimated value of error for total velocity is approximately 0.33 % and 0.67 % for $C_{P_{pitch}}$. With conditions prevalent to this project the estimated value of error for total velocity is below 0.33 % and thus can be considered negligible. The errors of the velocity components vary depending essentially on the pitch- and yaw angle. However, from the minimal variation of $C_{P_{pitch}}$ the velocity components need not be adjusted (can be considered to be equal to those obtained directly from measured data).

3.2.3.2 Reynolds and Mach number effects

The calibration of the five-hole probe shows appreciable variation with Reynolds number based on probe diameter (Re_d). The pressure coefficients for three test speeds are shown in Figure 11 (b). Pressure coefficients of medium- and high test speeds are similar. However, there is a significant variation between low- and medium test speeds. This indicating the sensitivity of the probe at lower test speeds. The probe should not be utilized at these low test speeds as readings would be inconsistent. This was also noted by Kirstein [2004KIR].

The calibration of the five-hole probe was performed over the Re_d region of the measured flow (wind tunnel tests). Hence, the Reynolds number effects are accounted for in the calibration.

(a)

(b)
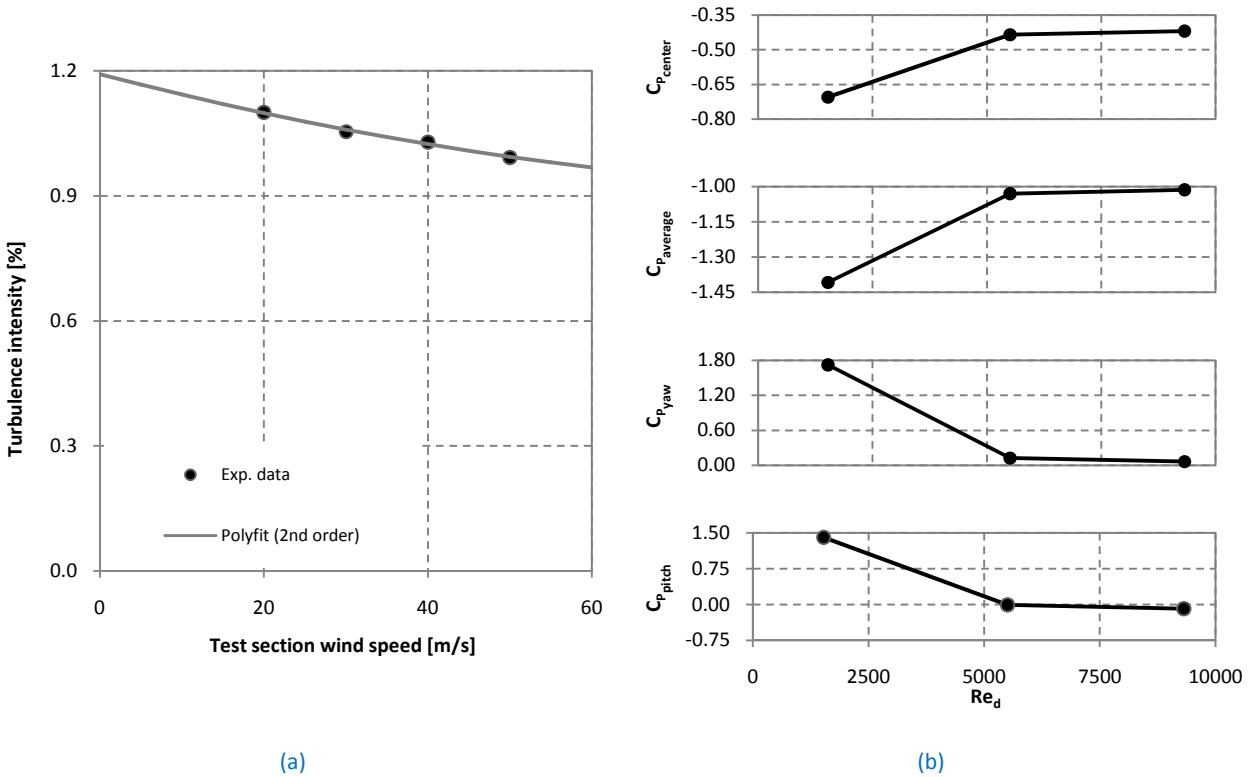
Figure 11: Possible sources of error (a) Turbulence intensity of large wind tunnel at different wind speeds, (b) Reynolds number effect for the five-hole probe in small wind tunnel (yaw- and pitch angle = 0°)

3.2.3.3 Effects of Pressure and Velocity Gradients

The five-hole probe is calibrated in an essentially uniform flow, but is used to measure relative flow with steep gradients in pressure and velocity present in the wake of the blade section (see Figure 17). Only the dominant effect of these gradients is considered. This dominant effect, spatial error, affects the probe performance. The other, lesser important effects are dealt with in [1981SIT]. The spatial error arises from each hole in a multi-hole probe being located in a differing pressure field.

The flow was found to be essentially two-dimensional with the preliminary analysis of the experimental data. Hence, the pitch angle(s) are ignored. Assuming the pressure gradient in the flow is known (dP_0/dn) then the yaw angle is corrected as follows [1981SIT]:

$$\epsilon = 13.2 \frac{d_p}{P_{tot,probe}} \left(\frac{d(P_{tot,probe})}{dn} \right) \tag{3.6}$$

where ϵ is error in degrees and d_p is the probe diameter.

The corrections in yaw angles revealed to be less than one tenth of a degree and thus are considered negligible (yaw angles are not adjusted). Sample calculations are shown in Appendix B.2.

3.2.3.4 Wall Vicinity Affects

Whenever a probe is located near a solid surface, the flow acceleration in that region introduces an additional error. Siteram *et al.* [1981SIT] showed that the error is negligible if the distance between the probe and blade is more than two probe diameters. The closest solid surface to the five-hole probe during testing was numerous times more than this and thus this error is negligible.

3.2.3.5 Effects of Blockage and Probe Stem

Probes used for flow measurement effectively block the flow area. This reduction causes the axial velocity to increase. The frontal area of the traverse mechanism with the five-hole probe locating bracket and the probe itself need to be included when considering the blockage. This frontal area is approximately 3.8 % of the area of the wind tunnel test section. It should be noted that the traverse mechanism was designed to have minimal effect on the test section flow. This was achieved by incorporating low drag components such as slender rods as well as positioning the probe 15 d_p upstream from the bulk of the traversing mechanism. From the factors mentioned, the blockage is considered negligible.

The probe stem supporting the probe causes interference with flow near the tip. Experimental results for pitot and static tubes indicate that this effect is negligible when the distance between the probe tip and the axis of the stem is more than four times the stem diameter. For the five-hole probe used this spacing is unfortunately only one stem diameter. However, the probe stem was present during calibration and thus the effects are accounted for.

3.2.4 Implementation of Calibration Data

A program based on the method developed by Wright [1970WRI] for the processing of calibration data from a five-hole probe, implementing Powells' method and golden section method for one-dimensional search is used. This program, with the calibration maps and pressures from the five-hole probe (obtained from further experiments) as inputs can calculate the total- and static pressure (and therefore velocity), and the pitch- and yaw angle of the flow at the tip of the probe. In Figure 12, a flow chart of the calibration program is shown.
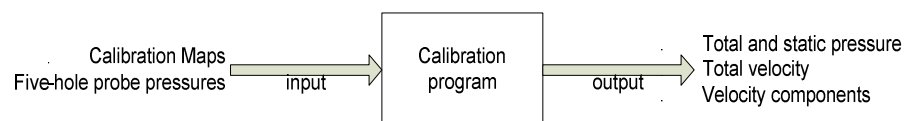
Figure 12: Flow chart of calibration program

As mentioned, the measured flow was found to be essentially two-dimensional. Thus, only the velocity components of the XY-plane needed to be considered (see Figure 10). The outcome being more accurate results, as optimisation techniques would not have to be utilised but rather simple curve fitting. This procedure is presented in Appendix C.

3.3 Experimental Test Setup

This section will describe the experimental test facility for the two-dimensional wind tunnel testing of the four blade sections and the setup thereof. The procedure used to obtain experimental data is also discussed. The chapter is concluded with the analysis of the experimental data, which is ultimately processed into performance parameters. The EFD results are presented in Section 5.1. The experimental test setup is shown in Figure 13, below.

Figure 13: Model mounted in wind tunnel test section.

3.3.1 Wind tunnel

The SU-M&M's low-speed wind tunnel is an open throat, no-return atmospheric facility. The test section is rectangular, 1 m high x 1.4 m wide, with filleted corners. The maximum test section speed is approximately 100 m/s. Blade section models are mounted vertically in the test section and are attached to a manually actuated turntable that allow the angle of attack to be set. The turntables are flush with the floor and ceiling and rotate with the model. The gaps between the turntables and test section floor and ceiling were sealed with grease. This proved to work well. The axis of rotation corresponds to the three-eighths of chord of the model. This is more than the traditional quarter-chord and is done to locate the models' leading- and trailing edge approximately equidistance from the edge of the turntables for installation of model convenience (model and two turntables are installed as a unit, Figure 14(a)).

The flow turbulence within the test section was measured with a hot wire probe. The recorded turbulence intensity of about 1 % is relatively high when compared to other wind tunnel specifications found in literature (typical value is 0.25 %). This could be due to, *inter alia*: the wind tunnel is of the open throat, no-return type; and non-ideal wind tunnel inlet configuration. Turbulence intensity is plotted against mean velocity in Figure 11 (a). The flow is assumed to be parallel to the sides at the inlet of test section.

3.3.2 Model

All four models have a chord length of 290 mm. The span is such that the models extended completely over the 1.0 m height of the test section. The construction of the two dimensional blade section models is described in Section 3.1.4. The root model is shown in Figure 14. Great care was taken to ensure that the models sufficiently represent the numerical models in terms of geometry and surface roughness (smooth).

(a)   (b)
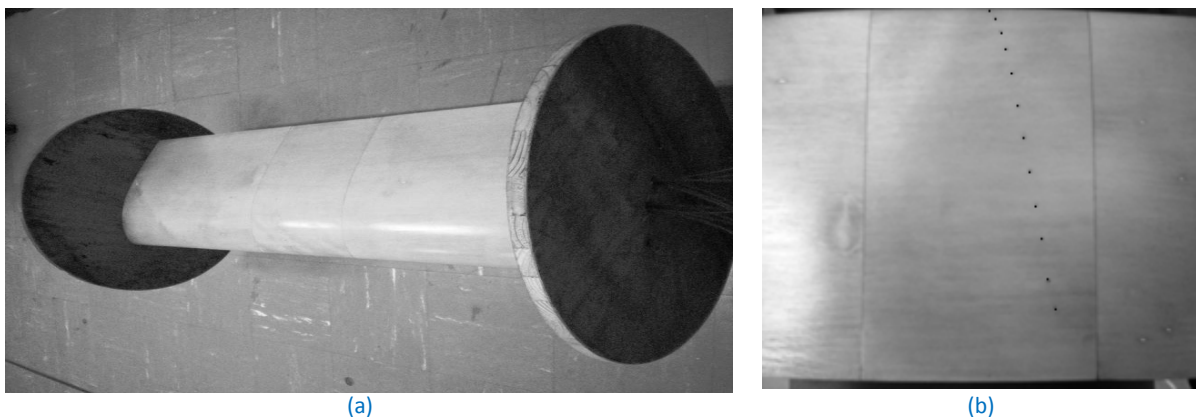
Figure 14: Root model (a) the unit which is installed in wind tunnel test section consisting of the three-part model and upper- and lower turntables (b) Staggered arrangement of static pressure taps on pressure side.

Each model has 13 pressure orifices on the upper surface and 12 on the lower surface (the leading edge is grouped with the upper surface and therefore surfaces have equal numbers of pressure orifices). As mentioned, each pressure orifices has a diameter of 1 mm and is drilled perpendicular to the surface.

The pressure orifices are concentrated near the leading edge. The spacing of the pressure orifices is based on the chord, in retrospect the surface length would have been a better parameter. The chord is divided into two regions, namely a growth factor and a constant region, Figure 15. The growth factor region is selected as the first third of the chord. Seven pressure orifices (upper and lower surface) are spaced within this region with a growth factor of 1.2. The location of the final pressure orifices is based on thickness of the blade section; for structural integrity and installation convenience of the piping which connects the pressure orifices to the pressure transducers. The constant region is simply taken from the end of growth factor region to the final pressure orifice. Six static pressure orifices are equally spaced in this region. To minimise flow disturbances, which may influence the flow and lead to premature transition, the static pressure taps are in a staggered arrangement along the span of the blade section (see Figure 14 (b)).

growth factor region   constant region
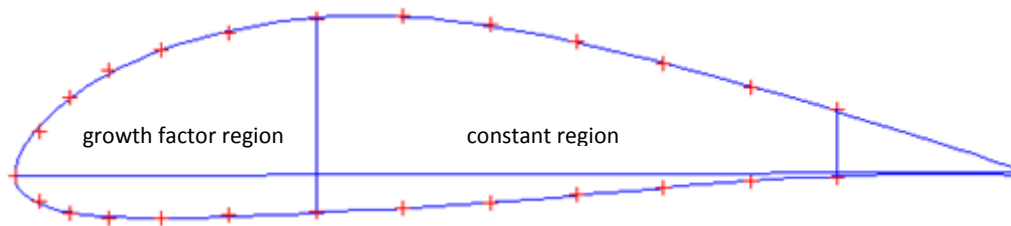
Figure 15: Location of static pressure taps on the root section

3.3.3 Wake Traverses

A traverse mechanism, shown in Figure 16, was designed and constructed to allow the five-hole probe to be traversed across the width of the wind tunnel test section. For these tests the probe is positioned vertically at the centreline of the wind tunnel test section (mid-span) with the tip of the probe located one chord length downstream of the model trailing edge, at 0° attack angle of the model. With the adjustment of the attack angle this spacing increased to 1.06 chord lengths at ± 20 ° attack angle. The probe is traversed manually by turning a handle which is connected to a threaded bar (bar 1) with a 2 mm pitch. By taking the spacing of the probe's holes into consideration it was decided that the smallest increment to be traversed would be 2 mm. It is possible to adjust the relative pitch angle of the probe during testing by rotating another threaded bar (bar 2) with a known pitch.
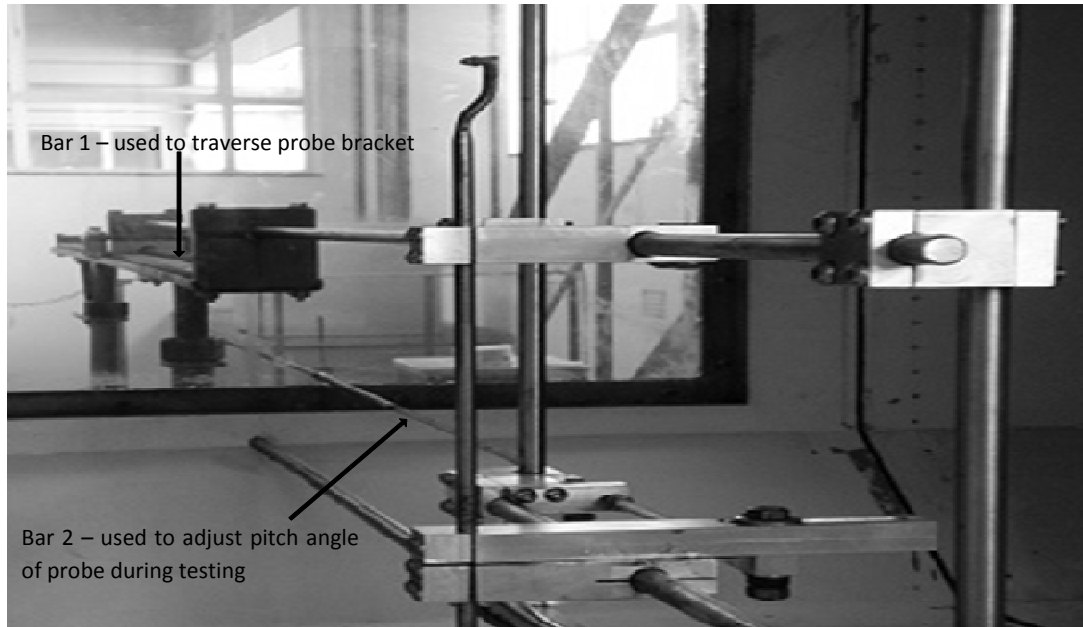
Figure 16: Five-hole probe located in traverse mechanism as seen from side of wind tunnel test section

The probe is traversed across the entire wake. The wake boundaries are considered at the traverse positions where the total pressure stabilizes (reaches the total pressure of the wind tunnel test section). An example of the relative total pressure measured over the wake is presented in Figure 17. The traverse location is aligned with the tunnel centre line (y=0). The pressures measured with the probe are relative to the total pressure measured by the Pitot-static tube located upstream of the model (without affecting the measured flow as seen in Figure 13).
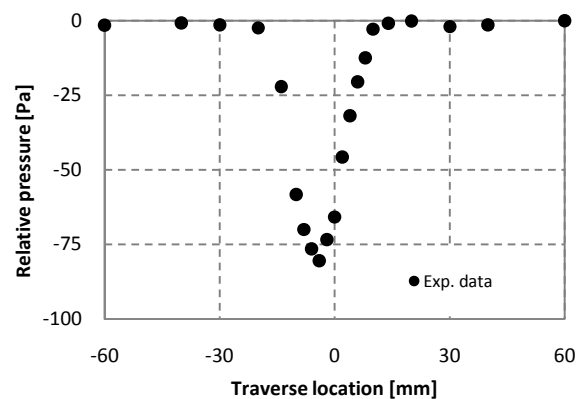
Figure 17: Total pressure of the probe over wake relative to the total pressure of Pitot-static probe located upstream of test object (mid section (α = 0°))

3.3.4 Data Acquisition System

The arrangement of the data acquisition system used is shown in Figure 18, below.
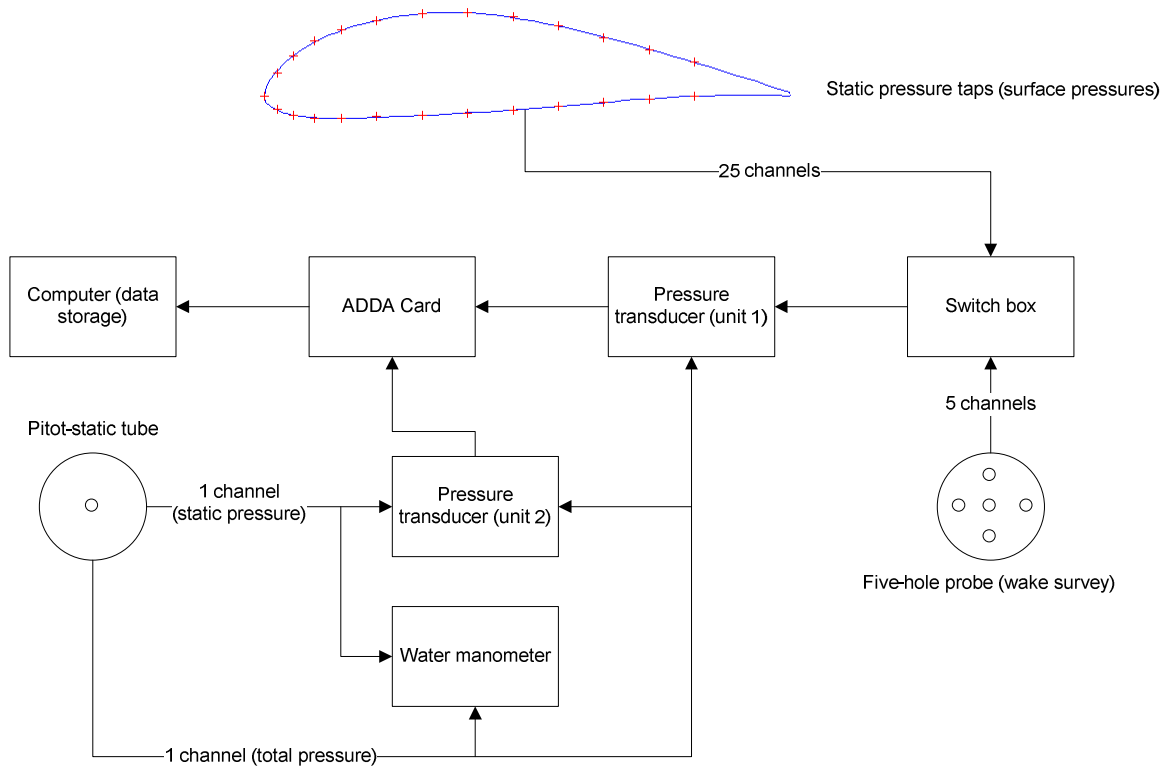
Figure 18: Arrangement of data acquisition system used for two-dimensional wind tunnel tests

3.3.4.1 Pressure Switch Box

The switch box allows pressure inputs to be read in sequence by a single pressure transducer. The switch box is a FCO 91 MkII selection box. It has 20 channels, with the integration of the slave unit an additional 20 channels are acquired. The channels are switched by means of solenoid valves by means of the Auto setting. This enables the count to be advanced by 1 step after a set time period. The set time period is 10 s. A lag was noted for the pressure measuring system. Hence, the first two data points were neglected resulting in the low variance (typically less than 1E-03) of the remaining eight data points. No trend in the data points was noted. This and preliminary tests showed leakage not to be an issue.

3.3.4.2 Transducers

Endress+Hauser™ Deltabar S pressure transducers are used for the two-dimensional wind tunnel tests. These pressure transducers calibrate themselves and require no additional amplification. Thus, no recalibration at regular intervals is required during testing. The pressure transducers are claimed by Endress+Hauser™ to have an accuracy of better than 0.1 % of the set span and stability better than 0.1 % of the upper range limit (URL) per year or 0.25 % of URL per 5 years. These pressure transducers are capable of measuring pressure differences between 0 and 2.5 kPa.

3.3.4.3 Laboratory Computer

A personal computer (PC) is used to store the pressure data via the ADDA card which is indirectly connected to the pressure transducers through the switch box. The sampling rate is 1 Hz (maximum sampling rate allowed by the setup). This provided 10 samples for each channel.

3.3.5 Experimental Procedure

All four blade sections are dealt with in a similar manner and thus the procedure is only covered once. The setup of the data acquisition system is not dealt with in this section; it is assumed that the layout according to Figure 18 is already in place. Only the model configuration will be dealt with in this section. The procedure followed to perform the two-dimensional wind tunnel tests is described by:

1. Install the model (model and turntables are installed as a unit (see Figure 14(a)) in the test section, secure the upper turntable to the manually actuated mechanism (situated on the ceiling of the test section) and locate the lower turntables to the floor locator of the test section.
2. Grease the gap between turntables and the wind tunnel test section.
3. Connect pressure points to the switch box via plastic tubing.
4. Close up the test section.
5. Perform necessary safety checks with regards to the wind tunnel.
6. Ensure that the mesh upstream of test section is free of debris.
7. Ensure the necessary pathways to the wind tunnel throat are not congested.
8. Ensure the doors used to regulate the wind speed in test section are fully closed.
9. Turn the wind tunnel axial fan on. Attain desired wind speed in test section by adjusting the doors. Wind speed is monitored with the Betz water manometer connected to the Pitot-static tube (see V_{wt} of Table 2).
10. Ensure that the lower turntable is not clamped to floor locator of test section.
11. Attain desired attack angle, refer to Table 3, by adjusting manual actuated mechanism.
12. Clamp the lower turntable to floor locator of test section.
13. Adjust relative pitch angle of the probe.
14. Traverse the probe across the width of test section and note the wake extremities and point of maximum total pressure loss (the wake crest), refer to Figure 17.

15. Capture surface pressure readings when the probe is located outside of the wake extremities and at the wake crest.
16. If required, perform wake traverse. Capturing data at designated points across the wake. Refer to Table 3.
17. Ensure data is saved.
18. Repeat steps 10 to 18, only perform traverse at chosen angles of attack, refer to Table 2.

As mentioned, step 2 worked well to seal test section. Step 12 is implemented to minimise vibration during data logging. Pressure transducer unit 1's (see Figure 18) visual display is referred to during step 14. Traverse measurements are, however, only recorded during step 16. The two sets of data acquired from step 15 are compared to investigate the influence of the location of the probe and the repeatability of the experiment. Results of this investigation are presented in Section 3.3.7.1.

Table 3: Tested angles of attack for blade sections

	Blade Section			
	Root	Mid	Semi	Tip
AOA Tested [°]	0	0	0	0
	7	9	7	7
	10	12	10	10
	13	15	15	15
	16			20

Additional wake traverses performed are indicated by filled cells

Note: Static pressure taps' data recorded for all AOA tested

3.3.6 Experimental Data Analysis

The following section illustrates the analysis procedure and the equations used to convert the experimental data into the relevant data such as the performance parameters.

3.3.6.1 Density, Pressure and Velocity
The air density, ρ, is calculated from the ideal gas law:

$$\rho = \frac{P}{RT}$$

(3.7)

where T [K] is the wind tunnel temperature, P is the total pressure upstream of model and R is the specific gas constant for air (287 [J/(kg·K)]). The temperature measured outside the wind tunnel is used in Equation (3.7) as it is assumed to be similar to the wind tunnel temperature.

The upstream dynamic pressure is calculated from:

$$P_{dyn,pitot} = P_{tot,pitot} - P_{stat,pitot} \tag{3.8}$$

where $P_{tot,pitot}$ [Pa] and $P_{stat,pitot}$ [Pa] are the Pitot-static tube total- and static pressure, respectively.

Upstream velocity $v_{upstream}$ from the Pitot-static tube is calculated from:

$$v_{upstream} = \sqrt{\frac{2(P_{dyn,pitot})}{\rho}} \tag{3.9}$$

3.3.6.2 Blade Section Forces from Pressure Distribution (Near-Field Method)

The blade section pressure coefficient $C_p(s)$ along the surface is calculated from:

$$C_p(s) = \frac{P(s) - P_{stat,pitot}}{P_{dyn,pitot}} \tag{3.10}$$

where $P(s)$ is the airfoil surface pressure around blade sections measured with static pressure taps.

The normal- C_N and the tangential force coefficient C_T are found from integration of $C_p(s)$:

$$C_N = \frac{N_f}{(p_{dyn,pitot})c} = \frac{1}{c} \oint C_p(s)\vec{t} \cdot \overrightarrow{ds}$$

$$\tag{3.11}$$

$$C_T = \frac{T_f}{(p_{dyn,pitot})c} = \frac{1}{c} \oint C_p(s)\vec{n} \cdot \overrightarrow{ds}$$

where N is the total normal force per unit length, T_f is the total tangential force per unit length, $\vec{t}$ is a unit vector aligned to the chord, $\vec{n}$ is a unit vector perpendicular to the chord, $\overrightarrow{ds}$ is running along the blade section surface and c is the chord length of blade section, Figure 19.
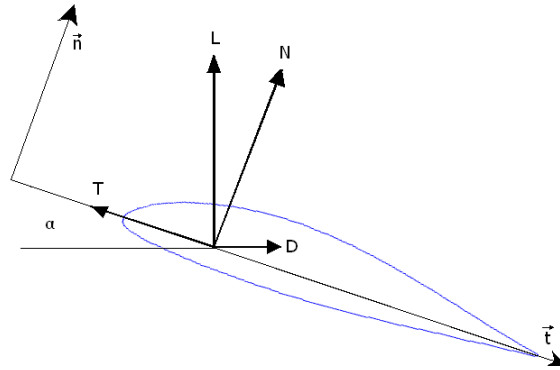
Figure 19: Sign convention for airfoil forces and unit vectors for integration of airfoil pressure

The lift and drag force are obtained by resolving N and T to the free stream flow by means of attack angle, α.

$$L = N\cos(\alpha) + T\sin(\alpha)$$

(3.12)

$$D_p = -T\cos(\alpha) + N\sin(\alpha)$$

From these values the lift- and drag coefficient are calculated

$$C_L = \frac{L}{(p_{dyn,pitot})c}$$

(3.13)

$$C_{D_p} = \frac{D_p}{(p_{dyn,pitot})c}$$

A Matlab © program was written to calculate the lift and drag coefficients. The inputs were the recorded voltages from the data acquisition system and the respective angles of attack. This program was verified by inputting $C_p(s)$ obtained from a CFD simulation and comparing the results. The results were similar, with 0.1 and 0.5 % difference for the drag and lift correlation, respectively (differences could be attributed to respective integration schemes). Thus, the program is functional.

3.3.6.3 Blade Section Forces from Wake Survey (Far-Field)

The total drag is calculated from the difference between momentum in the flow upstream and momentum in the flow measured downstream. Downstream data is acquired from wake survey performed with traversing five-hole probe. The flow was shown to be essentially two-dimensional. Hence, the following theory is applicable.

The total drag is calculated with two methods, namely the B.M. Jones' wake traverse method [1936JON] and the method developed by Maskell [1972MAS].

The Jones's method makes the assumption, *inter alia*, that the streamlines at the measuring station can be considered to be parallel, as seen in Figure 20. Only the magnitude of the velocity is thus required and therefore a Pitot-static is sufficient for the traverses. The probe is recommended to be at least 0.7 chord lengths downstream of the trailing edge of the model [1999BAR]. The total drag coefficient $C_{D_{Jones}}$ is calculated from:

$$C_{D_{Jones}} = 2 \int_w \sqrt{\frac{P_{tot,probe} - P_{stat,probe}}{P_{tot,pitot} - P_{stat,pitot}}} \left[1 - \sqrt{\frac{P_{tot,probe} - P_{stat,pitot}}{P_{tot,pitot} - P_{stat,pitot}}} \right] d\left(\frac{y}{c}\right) \qquad \text{(3.14)}$$

where $p_{tot,probe}$ and $p_{stat,probe}$ are the total- and static pressure, respectively, measured by the traversing probe, y is the distance along the line perpendicular to free stream at traverse station (mid-span).

As indicated in Equation (3.14) the integral needs to be evaluated only over the wake, because beyond the wake boundaries the total pressure $p_{tot,probe}$ becomes equal to $p_{tot,pitot}$ (see Figure 17) so the second term in the bracket becomes unity and the integrand becomes zero.
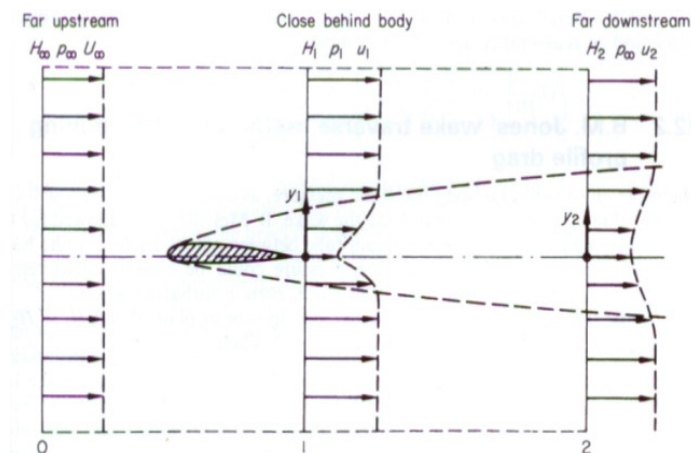
Figure 20: Two-dimensional control volume fixed in space of unit width

Maskell's method takes into consideration the non-zero flow angularity. The components of the total drag can be differentiated, namely profile drag and lift induced drag. Lift induced drag only occurs with three-dimensional flow and thus is not considered in this project. With a five-hole probe all necessary variables for the drag and lift analysis are available for this method. The total drag $D_{P,Maskell}$ and total drag coefficient $C_{D_{Maskel}}$ are calculated from (for the formulation of u_2^* and u_e refer to [1972MAS]):

$$D_{Maskell} = \int_w \left(P_{tot,pitot} - P_{tot,probe} \right) dy + \frac{1}{2} \rho \int_w (u_2^* - u_2)(u_2^* + u_2 - 2u_e) dy$$

<div align="right">(3.15)</div>

$$C_{D_{Maskel}} = \frac{D_{Maskell}}{\left(P_{dyn,pitot} \right) c}$$

The lift $L_{Maskell}$ follows from a surface integral of axial vorticity and a surface integral involving the downwash in the wake (refer to [1972MAS] for derivations):

$$L_{Maskell} = \rho \int_{w,probe} (u_2^* - u_2)(w_2) dy$$

<div align="right">(3.16)</div>

$$C_{L_{Maskell}} = \frac{L_{Maskell}}{\left(P_{dyn,pitot} \right) c}$$

The results of this section are tabulated in Appendix D.

3.3.7 Experimental Uncertainty

The final section of this chapter is used to quantify the experimental uncertainty. This uncertainty is a prerequisite when the results of this chapter are compared to the two-dimensional CFD modelling of Section 4.1 [1993CEL], [1986ROA]. This comparison is done in Section 5.1. Firstly the repeatability of the experiments is presented, followed by a section which quantifies the experimental uncertainty.

3.3.7.1 Repeatability
The repeatability of the experiment was verified by comparing the two sets of data acquired from step 15 of Section 3.3.5. Additionally this comparison is used to investigate the influence of the location of

the probe on the measured data. The pressure coefficients, along the blade section surface, calculated from the measured data of repetitive tests are presented in Figure 21, below.

(a)

(b)
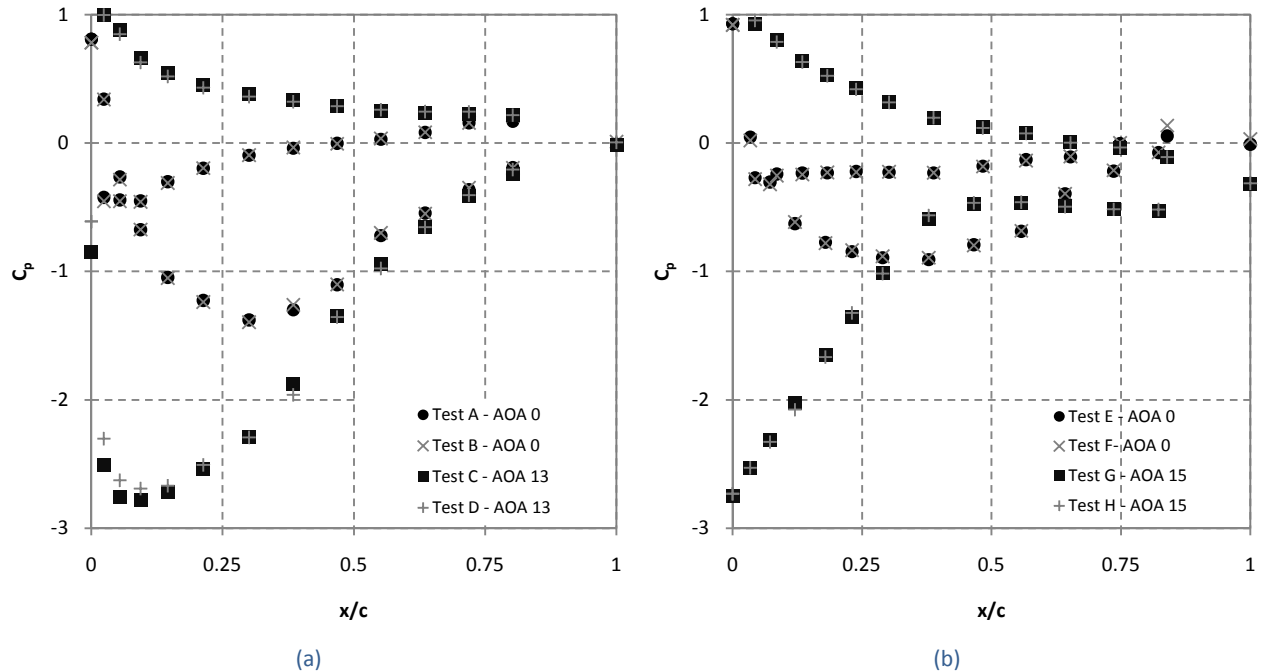
Figure 21: Pressure coefficients along the surface of (a) root and (b) tip blade section at different test setups

For each test setup the two sets of data are essentially the same. This established the experiment to be repeatable and that the probe had a negligible influence on the flow around the model. Nevertheless, the data with probe located outside the wake is favoured. The repeatability and the effect of the probe location were also considered independently but for brevity are not discussed.

3.3.7.2 Error Estimation

Every measurement is subject to some uncertainty. A measurement result is only complete if it is accompanied by a statement of the uncertainty in the measurement [2001BEL]. This section attempts to quantify the uncertainty of the experimental lift and drag coefficient measurements.

The blade section forces from the pressure distribution are evaluated with Equation (3.13). The two measurements which can introduce noteworthy experimental error to this equation are the setting of the angle of attack (Equation (3.12)), and the measurement of the pressure difference between pressure orifices on the surface of the blade sections and the upstream static pressure (Equation (3.10)).

A brief investigation of the effect of the variance of the attack angle on the blade section forces from the pressure distribution is now presented. The variance of the attack angle is estimated to be ± 0.5 °. This

estimate is relatively high, but human error is introduced as the angle of attack is manually set with the actuated mechanism.

The experimental data is processed as before but the assumed angle of attack is altered with ± 0.5 °. The root blade section was found to be the most sensitive to the variance of the angle of attack in terms of blade section forces from pressure distribution (other blade sections showed similar sensitivity). Hence, the root blade section is used as the case study for this investigation. The effect of the variance of the angle of attack on the lift and drag coefficients obtained from the pressure distribution is documented in Figure 22. The percentage difference, Figure 22(b), is determined by considering the difference between the lift or drag coefficient calculated with the assumed and altered angle of attack. As can be seen, this variance of the angle of attack has a significant influence on the calculated value of the drag coefficient; as high as 38 %. The average difference is approximately 22 %. It should be noted that the angle of attack offsets (see Figure 22 (a)) and therefore the error estimate is not as severe as reported. The lift coefficient remains essentially unaltered; less than 0.06 % difference.

(a)   (b)
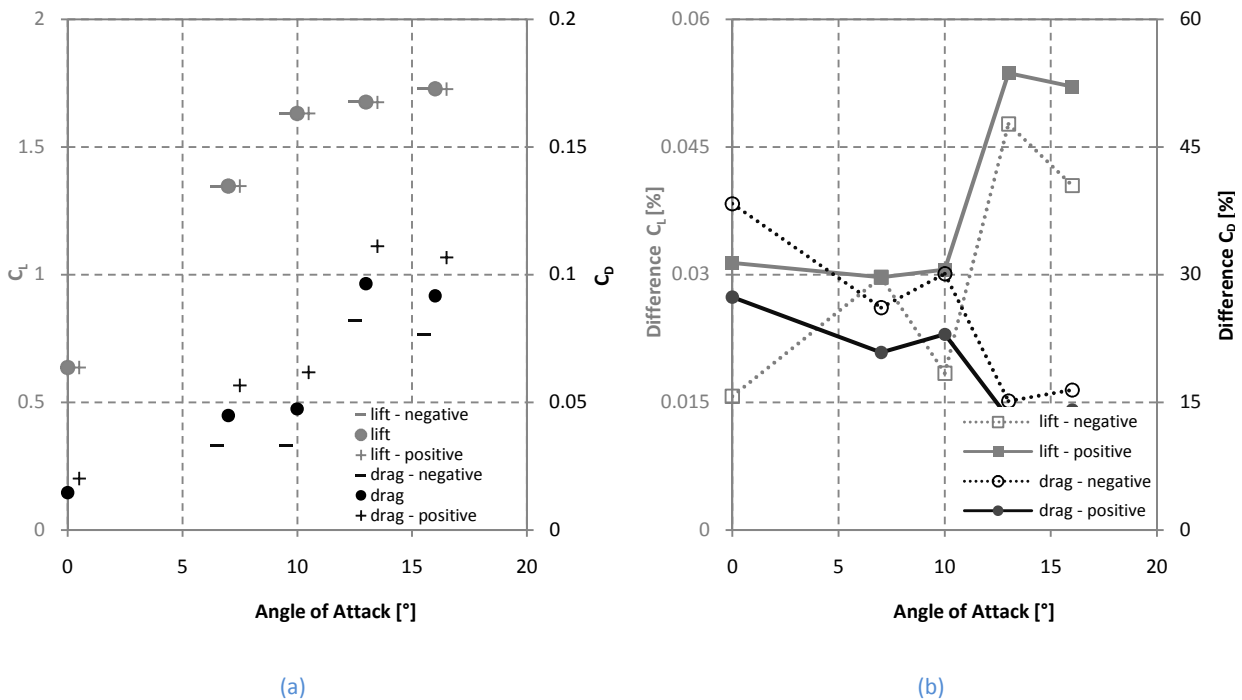
Figure 22: Effect of variance of angle of attack: (a) lift and drag coefficients (root) and (b) differences calculated

The error with regards to pressure measurement is quantified by considering the measurement setup. Only the possible error introduced by the pressure transducers is considered. As mentioned, the pressure transducers are claimed by Endress+Hauser™ to have an accuracy of better than 0.1 % of the set span.

An estimate for the overall error is computed from root-mean-square (rms) of the known errors. The results of this section are summarised in Table 4, below.

Table 4: Respective error estimates

	Error Estimate [%]		
	Pressure Difference	Angle of Attack	Total
C_L	0.1	0.06	0.117
C_{D_p}	0.1	22	22.0

The error estimate for the drag coefficient is alarmingly high. By decreasing the variance of the angle of attack to ± 0.1 ° this error estimate is decreased to approximately 5 % (this would depend on, *inter alia*, the geometry of the blade section). This is recommended for further studies and could be achieved by upgrading or replacing the mechanism used to set the angle of attack.

The values obtained for C_L from experimental pressure distribution can be used with considerably more confidence than the corresponding C_{D_p}. Fortunately, the far-field methods of Section 3.3.6 do not have this inherent sensitivity to the variance of the angle of attack.

The probable probe error for the pressures of a similar probe to the one used in this investigation to capture the wake survey data was estimated by Kirstein [2004KIR] to be 3.6 Pa. This gives an error estimate of less than 3 % (dependent on, *inter alia*, the free stream velocity and the angle of attack) when compared to the averaged total pressure difference measured in the wake. It should be noted that eight samples, instead of the six samples measured in [2004KIR], were recorded for each probe location and that simple curve fitting was implemented, instead of optimisation techniques as was done in [2004KIR]. Therefore, the error estimate for the C_D obtained with the wake survey data is less than the stated 3 %.

Summary

This chapter dealt with the experimental setup as well as the procedure and analysis of experimental data followed to determine the lift and drag coefficients of the blade sections over a range of attack angles. The repeatability of the experiment was established. The experimental uncertainty was quantified and found to be 0.12 and 22.0 % for the lift and drag coefficients obtained from the pressure distribution over the blade section surface, respectively. The experimental uncertainty for the drag coefficients obtained from the wake survey data was found to be less than 3 %.

4. Computational Fluid Dynamics (CFD)

This chapter consists of two sections, namely (4.1) two-dimensional and (4.2) three-dimensional CFD modelling. The wind tunnel tests performed are modelled in FLUENT [2006FLU], [2008FLU] as a two-dimensional problem as this was shown to be valid. The ultimate goal of this project is to predict the performance of the designed wind turbine blade. Hence, three-dimensional modelling is required, and for this the CFD package FINE Turbo 8.4-3 [2007FIN] of NUMECA is utilized.

4.1 Two-Dimensional CFD Modelling

The modelling process followed for this section is shown in Figure 23. This process needs to be dealt with as a whole as the elements are inter-dependent. For this discussion each process and decision will be dealt with individually.
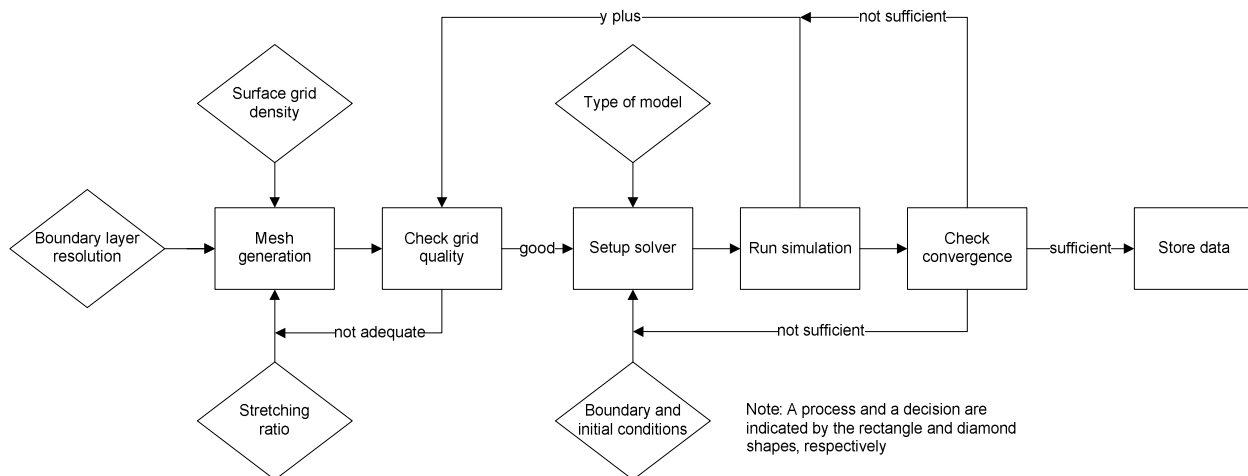
Figure 23: Flowchart of two-dimensional CFD modelling process

Two grid domains are considered, namely free and wind tunnel, Figure 28. The free domain is a typical grid used to simulate field conditions (free flow). Flow conditions in the wind tunnel test section differ from those in free flow. Hence, wind tunnel boundary corrections are traditionally applied to wind tunnel data to account for the differences. This approach is not followed. Instead, wind tunnel grid

domain results are verified with the wind tunnel data. Then the free-grid domain can be utilized with confidence to predict the field conditions flow.

4.1.1 Mesh Generation

The universal goal of a grid is to accurately resolve the flow domain numerically. This is achieved by ensuring sufficient grid density in the regions of interesting flow phenomena while preventing deterioration of grid density and smoothness in other areas. The boundary layer has steep velocity gradients owing to the presence of turbulence and the no-slip condition at the wall and thus is considered a region of interest. The steep velocity gradients of the turbulent flow are illustrated in Figure 24, below.
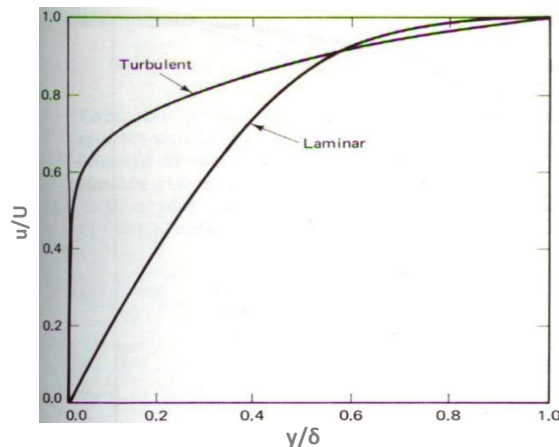
Figure 24: Comparison of the shapes of typical laminar and turbulent boundary layer profiles [1993SCH]

The three principal areas of interest in the grid system are the resolution of the boundary layer, the growth factor applied to the boundary layer grid known as the stretching factor, and the grid density on the surface of the geometry.

Before these factors are discussed a few grid parameters that were initially determined are stated. The structured curvilinear grid arrangement is used. It has been shown that the scatter band of drag prediction is greater in unstructured grid computation than in structured grid computation because of the larger numerical diffusion [2006YAM]. The o-mesh meshing scheme is employed and quadrilateral cells are used.

As can be seen from Figure 23 mesh generation is an iterative process. The grid needs to be evaluated before and after simulations. The latter is quantified with the resultant y^+ values and other flow parameters.

The mesh is generated in Fluent's pre-processor Gambit 2.4.6 [2006FLU].

4.1.1.1 Boundary Layer Resolution

Boundary layer resolution is affected significantly by the approach to modelling the near-wall region. The near-wall region consists of the viscous sublayer (viscous stresses dominate the flow adjacent to the wall) and the buffer layer (viscous and turbulent stresses are similar). These layers are indicated in Figure 25. There are two traditional approaches with modelling the near wall region. In one approach, the near-wall region is not resolved. Instead, semi-empirical formulas called wall-functions are used to bridge the viscosity affected region between the wall and the fully turbulent region.
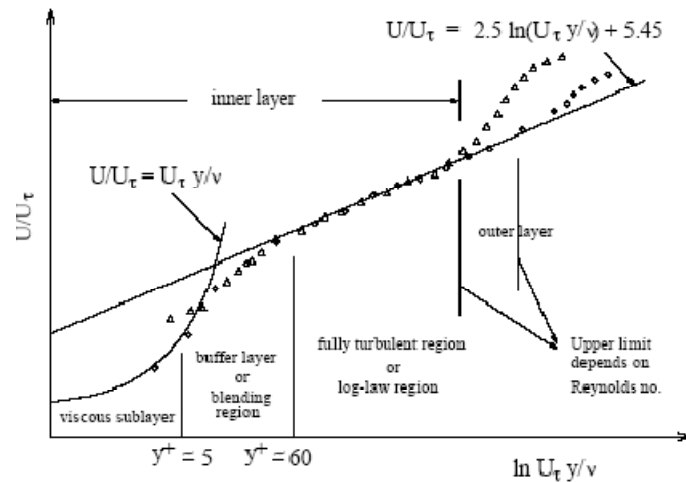
Figure 25: Subdivisions of the near-wall region [2006FLU]

In another approach, the turbulence models are modified to enable the near-wall region to be resolved with a mesh all the way to the wall, including the viscous sublayer. This is termed the low-Reynolds number approach. The reader is referred to Fluent documentation [2006FLU] for further details.

Proper resolution of the mesh for turbulent flows is important. Due to the strong interaction of the mean flow and turbulence, the numerical results for turbulent flows tend to be more susceptible to grid dependency than those for laminar flows. The wall-function approach should be avoided in situations where the wall effects are pervasive in the flow domain, and the hypothesis underlying the wall-functions cease to be valid [2006FLU]. The additional computational costs with regards to resolving the near-wall region were manageable and thus the low-Reynolds number approach is implemented.

Grid resolution requirements are well established for boundary layers which are to be resolved [2000MOI]. Initial normal spacing at the surface must be small enough to provide at least three points in the viscous sublayer [2002MOI] defined as the region bounded by $y^+ < 5$. This is achieved by enforcing

an upper bound on y^+ of approximately 1.5. A y^+ plot of the mid section analysis of the fine grid is presented in Figure 26. The y^+ values of the medium and fine grid used in the grid convergence study (Section 4.1.4) are similar to Figure 26 as the boundary layer resolution for the three grids are the same.
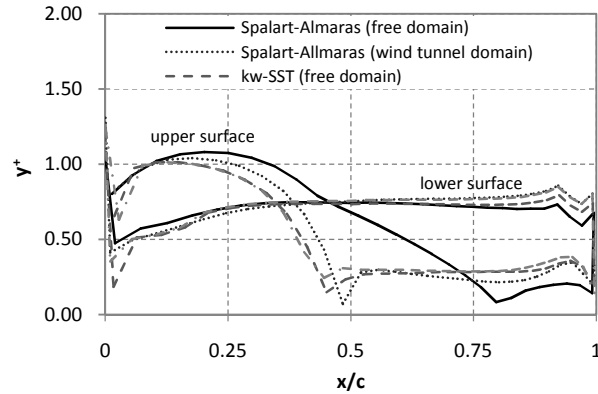
Figure 26: The variation y^+ along surface of mid section (α = 15° (fine grid))

4.1.1.2 Stretching Ratio

The grid is divided into three regions, namely the near-wall, the inner- and outer region, Figure 27. The near-wall is considered as the first mesh row. The profile is expanded by approximately one-quarter chord length creating the border between the inner- and outer region. The outer region extends to the grid domain boundary (not shown in Figure 27).
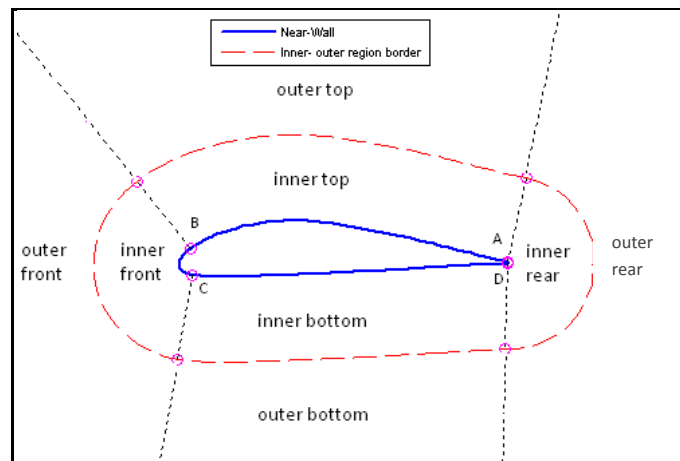
Figure 27: Grid domain (centre section)

An upper limit on the value of the stretching ratio has been established based on an analysis of optimal grid distribution with regard to truncation errors [2000SPA]. This upper limit is 1.2. It should be noted

that this upper limit is relevant to a one-equation turbulence model, namely the Spalart-Allmaras. However, it is still used as a guideline for the stretching ratio of the outer region. This two-dimensional problem necessitates relatively low computational cost and therefore a more conservative stretching ratio of approximately 1.15 is favoured for the outer region. This stretching ratio was not investigated in terms of grid sensitivity. The maximum allowable spacing between node points is set to one chord length (this was never reached).

The stretching ratio for the inner region is taken as 1.1. A brief grid sensitivity study of this stretching ratio was performed. No noteworthy change in flow parameters of interest transpired when ratio was altered to 1.05. The number of grid points increased dramatically. This was also found by Moitra [2002MOI]. Hence, the stretching ration of 1.1 for inner region was deemed to be suitable.

4.1.1.3 Surface Grid Density

The distribution of points on the surface is traditionally controlled by clustering points in the regions of high curvature and limiting the maximum allowable spacing between any two adjacent points to a specified value. Grid densities in the leading- and trailing edge require special attention.

A grid sensitivity study, Section 4.1.4, is performed to determine adequate distribution of points on the surface. As mentioned, only the surface grid density is altered with this study.

4.1.2 Grid Quality

It is vital to assess the grid quality, as a poor quality grid can cause inaccurate solutions and/or slow convergence. The quality of each grid generated is checked. An important grid quality metric is equi-angle skew (Q_{EQS}). Q_{EQS} is the measure of the orthogonility of the elements within the grid. Q_{EQS} ranges from 0 (best) to 1 (worst). Best describes a perfectly orthogonal element (for a quad element this would be a square). For quadrilateral cells this skewness should be less than 0.85 [2006FLU]. The worst Q_{EQS} found in all the meshes generated is 0.75. This is found in the root section grid.

As mentioned, the y^+ values also need to be considered when the grid is evaluated. The y^+ values of all the simulations were less than 1.5 as explained in Section 4.1.1.1.

4.1.3 Flow Solver

FLUENT 2ddp (two-dimensional with double precision) 6.3.26 flow solver is employed. The flow medium, air, is assumed to be incompressible. The pressure-based coupled solver (PBCS) is employed to solve simulations in the steady state domain. The PBCS is chosen as it is applicable for most single phase flows, and yields superior performance to the pressure based segregated solver. It should be noted that PBCS requires 1.5 - 2 times more memory than the segregated solver. The implicit solution approach is selected as it is generally preferred to the explicit approach, which has a very strict limit on the time step size. The bi-conjugate gradient stabilized method (BCGSTAB) [1994BAR] is implemented to improve the convergence of the linear solver. The Courant number is kept at the default value of 200. The relaxation factors selected are displayed in Table 5, below.

Table 5: Relaxation factors used in solver

Explicit relaxation factor		Under relaxation factors	
Momentum	0.5	Density	1
Pressure	0.5	Body forces	1
		Turbulent kinetic energy	0.8
		Specific dissipation	0.8
		Turbulent viscosity	0.8

The flow is not always aligned with the grid. Hence, the second-order-upwind interpolation schemes for the convection terms are used for all nodes. The computational expense of second order methods is more expensive (per grid point) than first order schemes, but the computational efficiency (accuracy per overall cost) of this higher order method is much greater. And it has been demonstrated many times that, for first order methods, the effect of numerical diffusion on the solution can be devastating [1993CEL], [1986ROA].

Stopping criteria for iterative calculations is based on monitoring both the residual history and the lift- and drag coefficients. Convergence is considered to occur only when both criteria are met in addition to grid sensitivity studies.

4.1.3.1. Boundary and Initial Conditions

The flow inlet and exit boundaries are set as velocity inlet- and outflow boundary conditions, respectively, Figure 28. The turbulence length scale ℓ is a physical quantity related to the size of the large eddies. For flow downstream of an obstacle it is more appropriate to base the turbulence length scale on the characteristic length of the obstacle rather than on the duct size. This is a typical approach when the wind tunnel utilized has guide vanes and wire mesh(es) upstream of the test section (wind tunnel utilized has one wire mesh upstream of the test section) [2006FLU]. The velocity inlet allows

turbulence input into the system by specifying the turbulence intensity and the hydraulic diameter (length scale). The turbulence intensity used for simulations is stipulated by the wind tunnel's test section turbulence intensity data, Figure 11 (a). The length scale is based on the wire mesh's pitch of 0.01 m. The walls of the wind tunnel are set as wall boundary condition (no-slip).

(a)   (b)
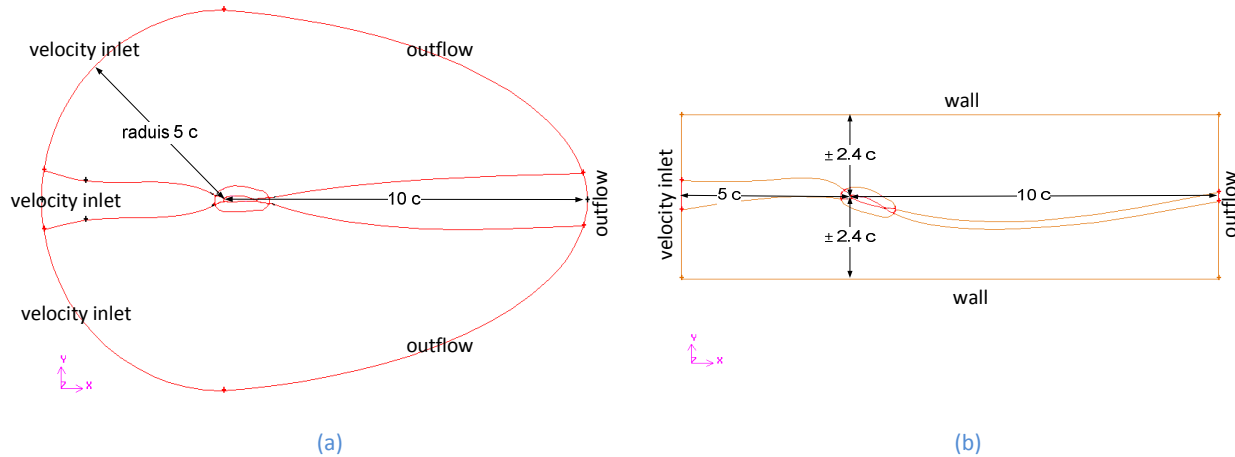
Figure 28: Boundary conditions for (a) free and (b) wind tunnel grid domain

The solution variables are initialized with the velocity inlet boundary condition.

4.1.3.2 Model Type

The type of model is dependent on the classification of the flow, namely laminar or turbulent. The transition from laminar to turbulent is the result of complex phenomena, which depend on numerous factors, such as Reynolds number, pressure gradient, wall temperature, wall mass transfer, disturbance environment, etc. A typical approach found in previous studies is to assume that the flow is fully turbulent. This assumption can be considered suitable when transition is close enough to the leading edge. Nevertheless, this assumption needs to be noted when the results are presented. A model which can deal with the transition from laminar to turbulent flow would be more well-founded.

Five turbulence models are selected: four fully turbulent and one transitional model. A comprehensive study by Celic *et al.* [2006CEL] compared 11 eddy-viscosity turbulence models frequently employed for computing aeronautical flows. This study provided a platform to select appropriate fully turbulent models. The turbulence models selected are eddy-viscosity turbulence models:

1. Spalart-Allmaras [1992SPA]
2. *k-ω* SST [1994MEN]
3. *k-ε* standard [1972LAU]
4. *k-ε* realizable [1995SHI]
5. Transition SST

The performance of the Spalart-Allmaras and *k-ω* SST turbulence model in [2006CEL] for the separated airfoil flow case was noted as poor- and medium-performance, respectively. It should be noted that no turbulence model was classified as good-performance. It cannot be stated that the *k-ω* SST model would more accurately predict the flows than the Spalart-Allmaras model for this project as the conditions are different to [2006CEL].

The *k-ε* standard is selected as it is widely used in industry. It was not considered in [2006CEL] as it has been shown to have deficiencies for predicting aerodynamic flows with adverse pressure gradients [1998WIL], [1997BAR], [1992MEN]. Therefore it was suspected that this model would predict the flows the least accurately.

Studies have shown that the *k-ε* realizable model provides the best performance of all the *k-ε* model versions for several validations of separated flows and flows with complex secondary flow features [2006FLU].

FLUENT 12.0 [2008FLU] provides two transitional models, namely the *k-kl-ω* transition and the transition SST model. The transition SST model is based on the coupling of the *k-ω* SST transport equations with two other transport equations, one for the intermittency and one for the transition onset criteria, in terms of momentum-thickness Reynolds number. An ANSYS proprietary empirical correlation has been developed to cover standard bypass transition as well as flows in low free-stream turbulence environments. The literature with regards to these two young models is limited. The transition SST model is the more computationally expensive of the two. Nevertheless, in industry the transition SST model is favoured [2008DEK]. Hence, this model was selected.

Two-dimensional simulations of the blade sections implementing the RSM turbulence model were performed. The model became unstable at high angles of attack, and, hence the respective results were not included in this thesis. It is recommended that further investigation into the implementation of the RSM turbulence model be performed, as to investigate the effect of the Boussinesq hypothesis (Section 2.2.2.1)

4.1.4 Grid Convergence Study

Sensitivities of the computed solution belong to two categories: those dependent on the grid and those influenced by attributes of the flow solver. Unfortunately the latter is beyond the scope of this study. The former is now investigated.

A grid sensitivity analysis is performed to determine adequate distribution of points on the surface by increasing this parameter until no discernable changes in the computed results are noticeable. The root section is used as a case study. Outcomes from this case study are simply applied to the three other profile sections. This is anticipated to be a valid approach as the four blade sections' profiles and test conditions are similar.

Three grid cases for the free-grid domain are considered. The inner region for free-grid domain and wind tunnel-grid domain are the same. Hence, it is thought acceptable to apply this grid convergence study results to the wind tunnel-grid domain as well. The only difference(s) between the three grid cases is the surface grid density. The approach to distribution of points on the surface in this project is based on the ratio of the number of surface points and the maximum allowable aspect ratio. Three maximum allowable aspect ratios are identified, namely 100 (rough), 75 (medium) and 50 (fine) [2007SCH]. Two points on the profile surface, points B and C of Figure 27, are identified to impose these parameters. Consequently from the low y^+ values a relatively large number of surface points are required.

The grid parameters used in the grid convergence study are summarized in Table 6. The spacing between surface points at the trailing and leading edge as well as the maximum spacing between points for the three cases are also indicated in the table. As mentioned, the stretching ratio of the inner and the outer region for all three cases are 1.1 and 1.15, respectively.

Table 6: Grid parameters used in grid convergence study of free-grid domain

Grid Case	Number of surface points	Number of grid points	Maximum aspect ratio	Spacing between surface points [% chord]		
				Leading edge	Maximum	Trailing edge
Rough	766 (n)	70794	100	0.26	0.40	0.07
Medium	1149 (1.5n)	98421	75	0.20	0.27	0.04
Fine	1532 (2n)	166988	50	0.13	0.20	0.03

Each grid case is simulated at required angles of attack with the selected turbulence models. The two-dimensional wind tunnel experimental setup stipulates the angles of attack, Table 3, for the simulations of this section.

Integrated performance parameters, lift- and drag coefficients, are monitored in order to establish grid convergence of the solution. The solver calculates the lift- and drag coefficients with near-field methods. The results of this convergence study are presented in Appendix E. The drag and lift results, considering only attack angles 0 and 16 °, are presented in the Table 7 and Figure 8, respectively.

Table 7: Drag coefficients used to investigate grid convergence (root section)

	Turbulence model	Spalart-Allamaras		$k\omega$-SST		$k\varepsilon$-standard	
	AOA [°]	0	16	0	16	0	16
Grid	Rough	0.0223	0.1325	0.0207	0.1417	0.0280	0.1438
	Medium	0.0221	0.1333	0.0203	0.1419	0.0275	0.1448
	Fine	0.0224	0.1297	0.0206	0.1380	0.0277	0.1337
	Variance	**2.0E-08**	**3.4E-06**	**3.5E-08**	**4.9E-06**	**7.1E-08**	**3.8E-05**

Table 8: Lift coefficients used to investigate grid convergence (root section)

	Turbulence model	Spalart-Allamaras		$k\omega$-SST		$k\varepsilon$-standard	
	AOA [°]	0	16	0	16	0	16
Grid	Rough	0.574	1.204	0.532	0.996	0.583	1.472
	Medium	0.577	1.215	0.528	1.016	0.589	1.453
	Fine	0.582	1.206	0.534	1.017	0.591	1.480
	Variance	**1.5E-05**	**3.1E-05**	**1.1E-05**	**1.4E-04**	**1.9E-05**	**1.9E-04**

From the low variances shown in the previous two tables the solutions can be considered grid independent. However, it should be noted that the results did not always converge as expected. For instance, consider the lift coefficient of the root blade section at 16 ° angle of attack obtained with the Spalart-Allmaras model (Table 8), the value for the rough grid is 1.204 then 1.215 for the medium grid and then unexpectedly 1.206 for the fine grid. This could be due to numerical error. Considering computational costs, the rough grid of each blade section is selected to be used for succeeding simulations. The rough grid of the tip blade section is shown in Figure 29.

4.1.5 Simulations

The five turbulence models are employed on both the free- and wind tunnel domain. The angles of attack for each blade sections' simulations are displayed in Table 3. For convenience, 180 cases were simulated with the use of batch and journal files. The results of these simulations are presented in Section 5.1.

(a)

(b)

(c)

(d)
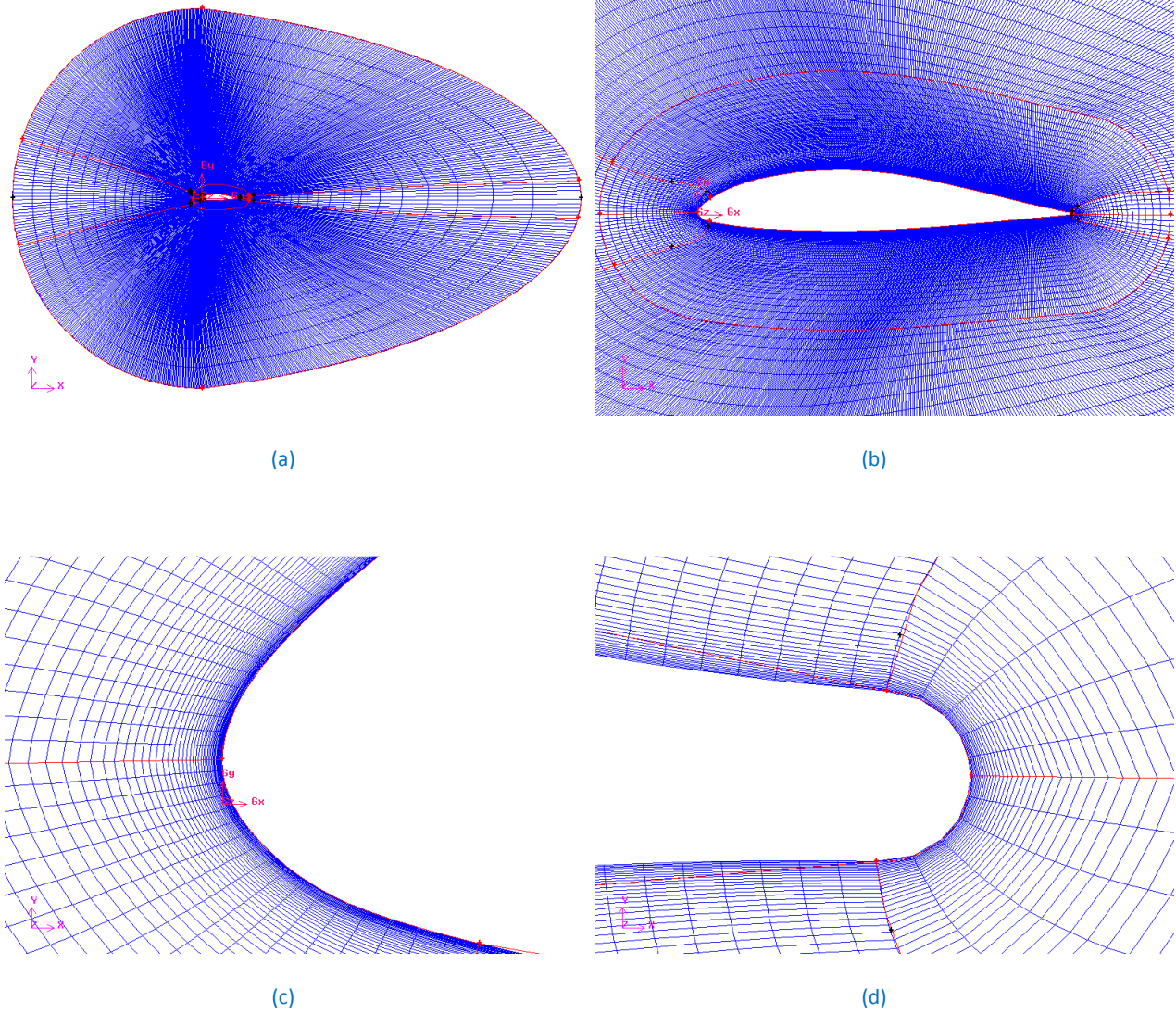
Figure 29: Grid display of (a) whole free-domain, (b) inner region of both free and wind tunnel-domain, (c) leading edge and (d) trailing edge

4.1.6 Transition to Three-Dimensional Flow

Traditionally, the design and analysis methods for wind turbines are based on relatively simple models of rotor blade aerodynamics, such as two-dimensional blade element momentum theory (BEMT). With the BEMT-type code the aerodynamic forces are represented by sectional airfoil characteristics, i.e. lift- and drag coefficients. These coefficients are typically obtained through analysis of experimental data such as the work done in Chapter 3. The results from this approach have been found wanting when compared to measured performance. For example, the NREL Combined experiment (Phase II) turbine exceeded predictions by approximately 15-20 % [1993HAN]. These discrepancies could be expected as BEMT is a two-dimensional theory and the aerodynamics of a rotating wind turbine rotor is highly three-dimensional [2004JOH] (refer to bullet 3, below).

It has been known since the 1940s that the lift force on rotating blade experiences higher values compared with a non-rotating blade when Himmelskamp [1947HIM] investigated the aerodynamics of an aeroplane propeller. This same lift enhancement was seen in measurements on wind turbines only in the late 1980s/early 1990s by, amongst others, Rasmussen *et al.* [1988RAS], Madsen and Rasmussen [1988MAD], Ronsten and Bruining [1991RON] with their field experiments on wind turbines.

Du *et al.* [1999DU] studied the effect of rotation on the boundary layer of a wind turbine blade. The focus of [1999DU] study was the separation location. The following main conclusions were obtained:

1. The separation point on the surface of the blade is slightly postponed, which can give rise to, as already mentioned, higher lift forces as well as lower drag forces as compared to two-dimensional conditions.
2. Increasing $\Omega r/V$ and Re and decreasing r/c result in delay of the separation point.
3. The three-dimensional effects are essentially the consequences of the centrifugal acceleration causing radial flow in the boundary layer and Coriolis forces tending to accelerate the flow in the chordwise direction toward the trailing edge (a reduction in the adverse pressure gradient). This delays the occurrence of separation further downstream.

From this brief literature review, discrepancies can be expected between, firstly the sectional airfoil characteristics (rotating blades) and two-dimensional airfoil characteristics (non-rotating), and secondly the performances predicted by BEMT method and the three-dimensional methods described in Section 4.2. These discrepancies are investigated in Section 5.3.

4.2 Three-Dimensional CFD Modelling

Three-dimensional simulations of the wind turbine rotor with NUMECA [2007FIN] will now be presented. A similar outline as used in Section 4.1 is followed.

The CFD package FINE Turbo 8.4-3 [2007FIN] of NUMECA is used for the simulations. FINE Turbo consists of the grid generator IGG Autogrid [2007AUT], the three-dimensional flow solver EURANUS [2007FIN] and the post processing tool CFView [2007CFV].

4.2.1 Mesh generation

NUMECA's fully or semi automatic grid generator for turbomachinery, AutoGrid, is employed to generate the grid. The grid is of the structured type. A skin-topology was chosen for the blade row, i.e. the blade row is surrounded by an O-mesh block, a skin block and four H-mesh blocks, which connect the skin block to the periodic boundaries as well as the inlet and outlet boundaries of the blade row (see Figure 33). Additional H-mesh blocks extend the flow domain to the upstream and downstream boundaries.

The additional package designated for propellers and wind turbines, Wind Turbine Wizard, is utilized. To obtain the semi-automatic grid with an optimal quality control, AutoGrid creates blade to blade grids onto surfaces of revolution. The generation based on a conformal mapping between the three-dimensional Cartesian space (XYZ coordinates) and the cylindrical surfaces of the two-dimensional blade to blade space (dm/r-θ plane) follows four main steps [2007AUT]. The final step is the generation of the three-dimensional mesh. This step is not dealt with in this project as it is automatically performed by AutoGrid. The first three steps are presented as subheadings.

4.2.1.1 Definition of the Geometry

The complete geometry of the wind turbine needed to be established. The turbine rotor was defined in [2006CEN] from 20 % (root) to 90 % (tip) radius as well as the radius of the hub. This leaves three regions of the wind turbine undefined, namely the hub, hub-to-root and tip-to-end region.

A circular cross section at the hub intersection is favoured as it is a typical feature found in industry. Simple calculations with assumptions are used to determine the radius of this section (r_{hub_insert}) for a worst case scenario.

The hub is divided into three axis-symmetric divisions, namely the front and rear bulb and the transition section. The shape of the front and rear bulb is defined by a one-half ellipsoid and a one-half sphere, respectively. The ellipsoid length is equal to two hub radii r_{hub}. The front bulb and the rear bulb are located $1\,r_{hub\_insert}$ upstream and $8\,r_{hub}$ downstream of the rotational plane of the rotor, respectively.

A tip with all sections located around the pitch axis (tip that ends at the pitch axis) is selected. This is a typical shape found in industry and was found by Ferrer and Munduate to be the best tip shape of the three considered (square and swept-back tip being the other options) [2007FER]. The end and tip section profiles are the same, with the end section having a chord length of 20 mm.

In-house blending functions incorporating sinusoidal and elliptical functions shown in Figure 30 are used to create a smooth transition for the both hub-to-root and tip-to-end region, respectively.
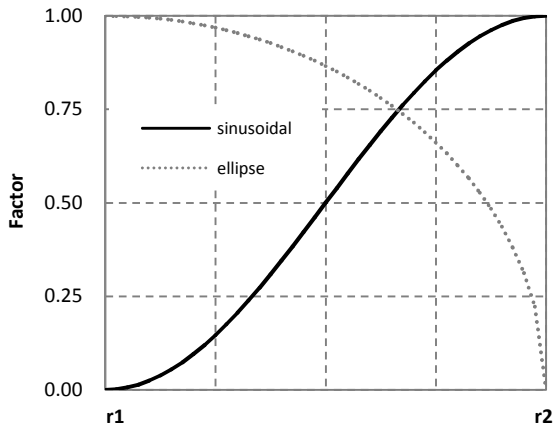
For the hub-to-root region using the sinusoidal function

$$x\left(r\right) = x_{hub}\big(1 - Factor(r)\big) + x_{root}Factor(r)$$

$$y\left(r\right) = y_{hub}\big(1 - Factor(r)\big) + y_{root}Factor(r)$$

(4.1)

For the tip-to-end region using the ellipse function

$$x\left(r\right) = x_{tip}Factor(r) + x_{end}\big(1 - Factor(r)\big)$$

$$y\left(r\right) = y_{tip}Factor(r) + y_{end}\big(1 - Factor(r)\big)$$

(4.2)

Figure 30: Blending functions used to generate smooth transitions for the hub-to-root and tip-to-end regions

The geometry is shown in Figure 31, below.
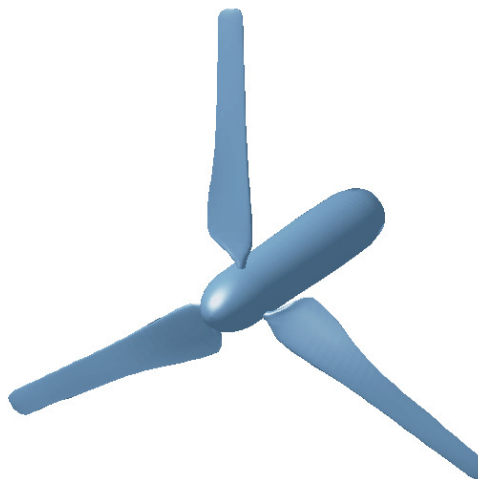
Figure 31: Geometry of the wind turbine rotor

4.2.1.2 Generation of Meridional Flow Paths

The wind turbine wizard creates two meridional divisions within the grid, namely the blade and the far field meridional domain, Figure 32. The latter's inner and outer boundaries are 1 and 5 rotor radius (R_{rotor}), respectively. The grid inlet and outlet are located 5 R_{rotor} upstream and 5 R_{rotor} downstream of the rotational plane of the rotor, respectively. These grid boundaries ensure an undisturbed flow field near the domain boundaries.

(a)   (b)
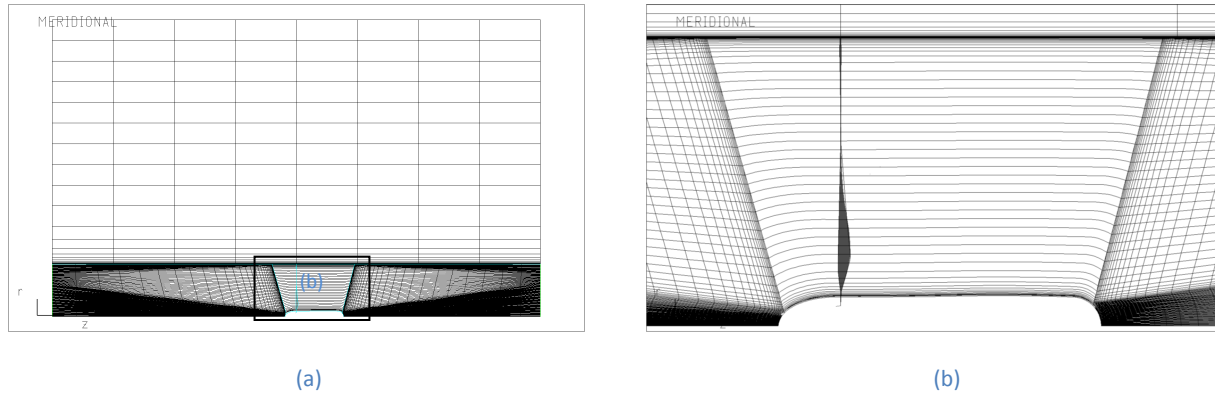
Figure 32: Meridional view of (a) whole and (b) blade row domain

The meridional flow paths define the trace of the surfaces of revolution on which the three-dimensional mesh will be built. A total of 73 flow paths for the blade meridional domain are selected with 33 % constant cell and clustering at hub and blade tip. This clustering is controlled by setting the spacing at both the hub and the tip to 1 x 10^{-4} m.

A total of 33 flow paths for the far field meridional domain are selected with 33 % constant cell. Clustering of 1 x 10^{-4} m at the blade tip ensures a smooth transition between the two meridional domains.

4.2.1.3 Generation of Two-Dimensional Meshes on Spanwise Surfaces

The highly staggered wind turbine mesh topology composing of six blocks is used, Figure 33, namely the O-mesh block (thin layer on the blade wall (not discernible in the figure)), the skin block (DEIH) and four H-mesh blocks. Ideally, the surface grid density would be similar to the two-dimensional grid of Section 4.1. Unfortunately the elevated computational cost of these three-dimensional simulations forced a more conservative number of surface points to be used. However, a grid convergence study is performed to ensure sufficient grid resolution. The spacing of the grid points is shown in Figure 33 (a) and grid block boundaries in Figure 33 (b). In Figure 33 (b) the wind direction of the free stream is indicated.
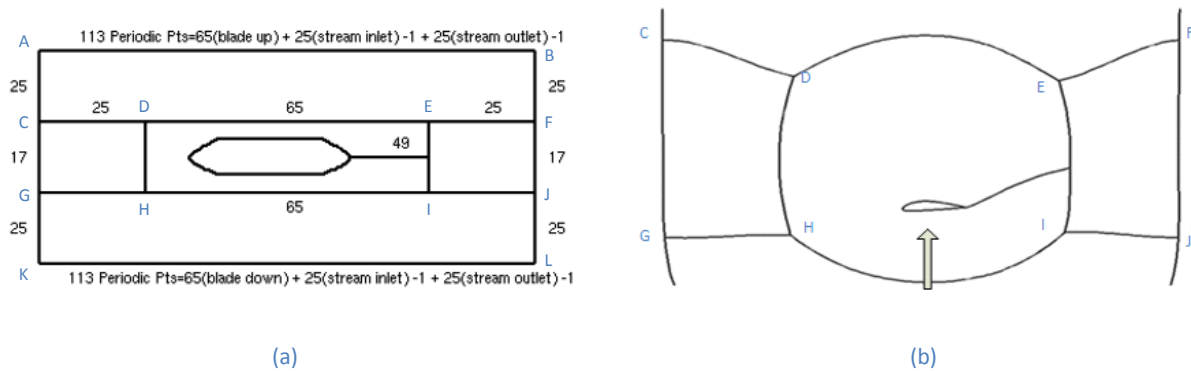
Figure 33: Grid (a) point spacing of the rotor blade row, (b) block boundaries of rotor blade row (mid section)

4.2.2 Grid Quality

As mentioned, it is vital to assess the grid quality as a poor quality grid can cause inaccurate solutions and/or slow convergence. Orthogonality is used to gauge the grid quality. Orthogonality is the measure of the minimum angle between the edges of the element. It ranges from 0 – 90 °, with 0 ° being the worst. The orthogonality of a few cells near the tip of the rotor was poor. Fortunately this could be rectified by neglecting 0.03 % of the outer radius of the rotor. This improved the minimum value of the orthogonality from 5.6 to an acceptable 15 ° and was deemed to have negligible effect on the performance of the wind turbine.

AutoGrid is employed to generate the grid semi-automatically. Therefore, when compared to the two-dimensional CFD modelling of Section 4.1, less user input is required. Thus, a more thorough grid quality assessment is required for this section. Hence, an additional two parameters are used for this assessment, namely aspect ratio and expansion ratio. The grid quality metrics for the near blade and the remainder grid regions are presented in Table 9, below.

Table 9: Assessment of the grid

	Blade	Remainder	Typical limits [2008HIL]
Orthogonality - minimum [°]	14.8	35	> 20
Expansion ratio - maximum	2.55	2.64	< 2
Aspect ratio - maximum	14345	2128	< 5000

According to Table 9 all the grid quality metrics are, in theory, violated. However it should be noted that these values pertain to only a few cells in the flow domain and thus is not so severe. For instance only 0.1 % of the cells have a value of less than 20 for orthogonality, only 0.3 % of the cells have an aspect

ratio of higher than 5000 and only 0.1 % of the cells have an expansion ratio higher than 2. Consequently, from the decision to have a tip with all sections located around the pitch axis (refer to Section 4.2.1.1), the geometry of this section induces the poor orthogonality. This is simply unavoidable. The expansion ratio of slightly more than 2.5 is deemed acceptable. The worst cells with regards to aspect ratio are relatively far downstream of the blade row and their improvement would require considerably more points. Additionally, this is the least important quality criterion. The grid is not ideal, but considering the challenging application and the considerable increase in computational costs required to improve the grid, the grid is deemed adequate [2008HIL].

The y^+ values of all the simulations on the blade and hub of the rotor were less than 1.5 and 7, respectively. The grid of the blade row is shown in Figure 34, below

(a)   (b)   (c)
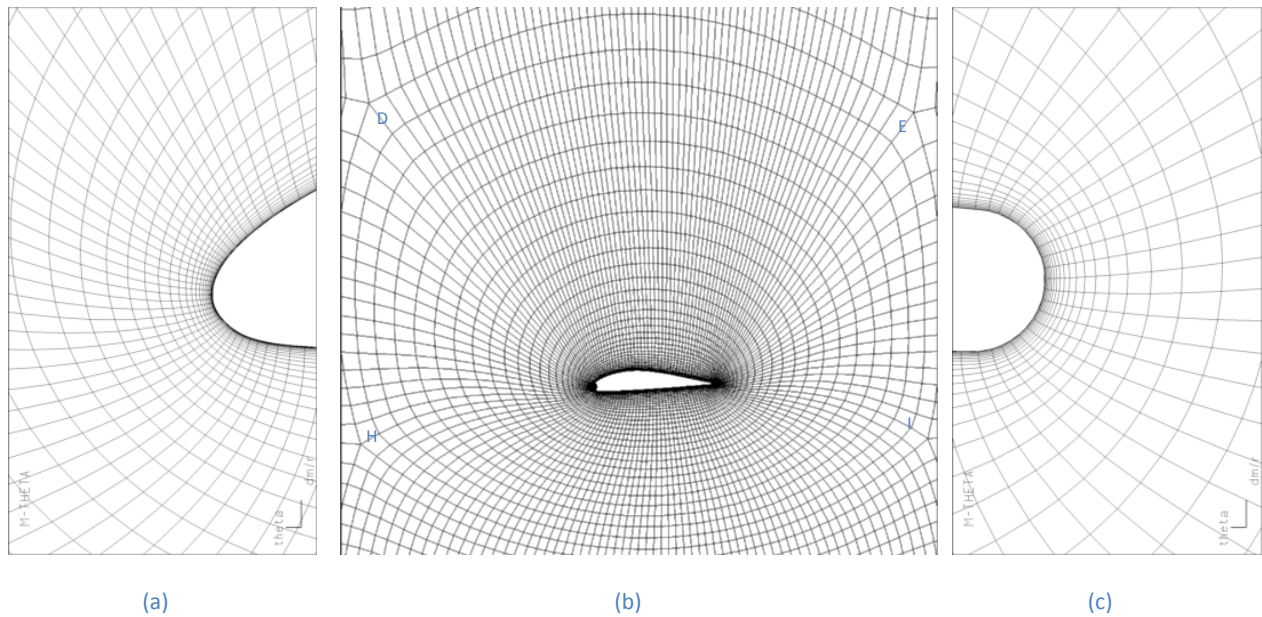
Figure 34: Typical grid (fine) at the (a) leading edge, (b) skin block (DEIH) and (c) trailing edge

4.2.3 Flow Solver

The Fine Turbo 8.4-3 flow solver EURANUS is employed. The flow medium is air and is considered to be an ideal gas. The simulations are computed in the steady state domain implementing the turbulent type mathematical model to solve the RANS equations.

The Courant-Friedrich-Levy (CFL) number globally scales the time-step sizes used for the time-marching scheme of the flow solver. A conservative value of two was implemented for the CFL number so as to avoid possible divergence (a higher value of the CFL number results in a faster convergence, but will lead to divergence if the stability limit is exceeded).

Stopping criteria for iterative calculations are based on monitoring both the residuals and the performance parameter of interest, namely the torque. Convergence on the fine grid is usually achieved within 300 iterations; with the residuals diminished by more than four orders of magnitude and the torque not varying to four significant numbers.

4.2.3.1 Model Type

The turbulent models selected are:

1. Spalart-Allmaras
2. Spalart-Allmaras-Transition
3. k-ω SST
4. k-ε Yang-Shih (Low Reynolds number)
5. k-ε non linear (Low Reynolds number)

The only transitional turbulence model available with Fine Turbo 8.4-3 is that of Spalart-Allmaras. The implemented transition model is based on correlations obtained by Abu-Ghannam and Shaw [1980ABU]. These correlations are derived from experimental data from transition on a flat plate with pressure gradients. The fully turbulent Spalart-Allmaras model is also incorporated as to investigate the effect of transitional modelling.

It has been shown that the k-ω SST model correctly predicts wind turbine rotor stall [2004PAP].

From the investigation of Benjanirat and Sankar [2003BEN] it was shown that the k-ε model with near wall effects gave the best agreement with measurements (Section 2.2.2.1). The k-ε non linear model which is based on the k-ε Yang-Shih model has been shown to give improved prediction of separated flows when compared to linear models [1987SPE].

4.2.3.2 Low-Speed Preconditioning

In the low subsonic Mach number regime, time-marching algorithms designed for compressible flows show a pronounced lack of efficiency. The development of a low speed preconditioner was motivated in order to provide fast convergence characteristics and accurate solutions as the Mach number approaches zero.

Pape and Lecanu [2004PAP] found that low-speed preconditioning is seemingly essential for wind turbine aerodynamic solutions when a compressible Navier-Stokes solver is used to compute a very-low-Mach-number flow field.

The highest and lowest Mach number experienced by the blade sections for a wind speed of 5.5 m/s is 0.09 and 0.016. These values are less than the Mach numbers reported in [2004PAP]. Therefore, low

speed preconditioning is applied. The numerical preconditioning proposed by Merkle [2007FIN] is implemented.

4.2.3.3 Boundary and Initial Conditions

Three boundary conditions are used, namely periodic, solid and external. Boundary conditions are stipulated in the cylindrical coordinate system. The mesh generator automatically establishes all connecting and periodic boundary conditions and the corresponding information is transmitted to the Fine interface. Hence, no user input is required.

The hub and the blade are classified as solids.

The external boundary is non-directional as opposed to inlet or outlet boundary conditions. Hence external boundary conditions are used as the flow direction (in or out) is not known throughout the flow domain prior to simulations. The free stream velocity of the fluid of 5.5 m/s in the streamwise (k) directions is defined with the external boundary conditions.

The rotation of the wind turbine is set to 80 rpm as prescribed by [2006CEN].

The simulations are initialized with the results of the grid convergence study's fine grid (Spalart-Allmaras turbulence model is used (refer to the following section)).

4.2.4 Grid Convergence Study

The sensitivities of the computed solutions as dependent on the grid will now be investigated. As with the two-dimensional CFD simulations of Section 4.1 the influence of the flow solver on the computed solution is beyond the scope of this study. The Spalart-Allmaras turbulence model is used for this investigation.

Multigrid parameters are implemented to allow simulations to be run on several sub-meshes with one grid. Three sub-meshes were generated, namely a rough, medium and a fine. The generation of the fine mesh is described in Section 4.2.1. The medium and rough grids are generated semi-automatically from the original grid. The number of grid points are reduced in the i (azimuthal) , j (spanwise), and k (streamwise) directions to generate a rougher grid with half the number of cells in the three directions (in Figure 33, DE and DH are in the i and k directions, respectively). For instance, the one grid boundary, DE, of the skin mesh block (DEIH) has 65 grid points for the fine grid. Hence it has 64 cells. The medium and rough grid will then have 32 and 16 cells for DE, respectively.

Initial simulations are performed on the rough grid. The rough grid is initialized with the free stream velocity of 5.5 m/s. The results of this simulation are then used to initialize the next simulation on a finer grid, and so forth.

The grid parameters used in the grid convergence study are summarized in Table 10, below.

Table 10: Grid parameters used in grid convergence study

Grid Case	Number of grid points	Wall height on blade [mm]	Maximum y^+ on blade
Rough	54012	0.04	10
Medium	380144	0.02	4
Fine	2845704	0.01	1.5

The integrated performance parameter, torque, is monitored to establish grid convergence of the solution. The torque is calculated from the pressure and the velocity fields on the walls. The results of this convergence study are presented in Table 11. The method used to calculate the solution for an infinite number of cells is presented in Appendix B.3. The error is determined by considering the difference between the fine grid and the infinite cells estimation. The n used in the calculations of Appendix B.3 is the order of the numerical scheme and is found to have a value of 0.91; indicating a near linear convergence.

Table 11: Torques predicted

Grid case	Torques [Nm]
Rough	216.1
Medium	224.8
Fine	229.4
Infinite cells	235.6
Error	2.2 %
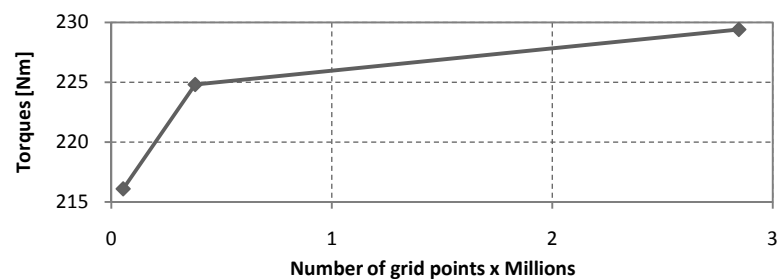
Figure 35: Torques predicted versus number of grid points

The grid convergence index (GCI) method presented by Celik [2004CEL] is used to for the calculation and the reporting of the discretization error estimates in CFD simulations. This method is an acceptable and recommended method that has been evaluated over several hundred CFD cases [2004CEL]. This method was employed to investigate the numerical uncertainty of the fine grid solution and is presented in Appendix B.4. This uncertainty was found to be 2.8 %. From this and the relatively low error presented in Table 11, the numerical solution(s) of the fine grid can be considered to be similar to the exact solution.

However, it should be noted that the y^+ values are dependent on the grid but not directly proportional. This dependency is depicted by the spacing of the first grid points from the wall boundary. With the multigrid parameters, this spacing is altered by a factor of two and four for the medium and rough grid, respectively. By varying the y^+ values the turbulent models could break down to a lesser or greater degree and thus affect the solution. As mentioned the y^+ values on the blade for the fine grid were all less than 1.5, for the medium and rough grid the values were less than 4 and 10, respectively (Table 10). Therefore, this grid convergence study is not presented as conclusive verification of grid convergence.

4.2.5 Numerical Data Analysis

The following section illustrates the analysis procedure and the equations used to convert the output of the CFD computations into the relevant data in the form of performance parameters. The performance is assessed in terms of C_P , which is calculated as follows:

$$C_P = \frac{Power}{0.5\rho AV^3} \qquad \text{(4.3)}$$

where $Power$ is the power extracted by the wind turbine and given by equation below

$$Power = T_q\Omega \qquad \text{(4.4)}$$

where Ω is the rotational speed and T_q is the torque generated by the wind turbine from the available wind stream. The torque is the output of the CFD computations.

Data Presentation and Discussion

5. Results

In chapter 3 (EFD) & 4 (CFD) the tools and methods were described whereby required data was respectively collected and generated.

The confidence levels of both the experimental and numerical (CFD) results have been presented in the respective chapters and need to be noted when comparisons are made [2000ERC], [1998AIA].

Oberkamp and Trucano [2002OBE] stated that the ultimate test of a CFD model is a comparison between its output and reliable experimental data, provided experimental uncertainty is established. Hence, the comparison of the results of chapter 3 & 4 will provide validation of the two-dimensional CFD modelling and is presented in the first section of this chapter.

As mentioned, the flow field around the wind turbine was not investigated experimentally in this investigation, as the necessary experimental work was beyond the scope of this thesis. Thus, the three-dimensional CFD results are not validated. However, this project forms the second part of a larger research project (initial work done in [2006CEN]). The third component will be the collection of reliable three-dimensional experimental data which can be used to validate the three-dimensional CFD results which are presented in the final section of this chapter.

The effect of rotation of the wind turbine blade on the aerodynamic characteristics is presented in the final section of this chapter

5.1 Experimental Comparison: Two-Dimensional CFD Validation

In this section the two-dimensional CFD model is validated. This is achieved by comparing the performance parameters, the lift and drag coefficients of the four blade sections, collected with EFD and those generated by CFD. A brief description on the result types is given to gain a better understanding of which data should be compared and how it should be interpreted before the results are presented.

The experimental data is compared to the results of the CFD simulations run on the wind tunnel grid domain, as this more accurately represents the physical wind tunnel testing environment than the free grid domain does.

The XFOIL code uses a panel method to predict the outer (potential) flow and accounts for viscous effects using an integral boundary-layer approach. The code assumes that the flow domain boundaries are infinitely far from the airfoil. Therefore, the results of the CFD simulations on the free grid domain are compared to the XFOIL results, as the free grid domain more accurately represents an infinite domain than does the wind tunnel grid domain. The XFOIL results are also compared to wind tunnel measurements as this type of comparison was found in literature [2002MAU], [1998FUG].

Two types of drag forces were calculated from the experimental work of Chapter 3, namely pressure drag from the integration of the pressure distribution over the blade section surface and the total drag from the wake survey data.

With the wind tunnel testing, the probe used to capture the wake survey data was located at mid span and approximately one chord length behind the trailing edge of the model. This was done to comply with the requirements of the B. M. Jones' wake transverse method [1936JON]. Unfortunately, this distance behind the trailing edge was too great to obtain the lift force from the Maskell method [1972MAS]. It is recommended for future studies that additional wake measurements be taken closer to the trailing edge. This supplementary data can be used to calculate the total lift.

As mentioned, the CFD computations performed in Chapter 4 implement the near-field method to compute the aerodynamic forces. Therefore, the total drag is decomposed into pressure and viscous (skin friction) drag. The viscous lift contribution to the total lift force is negligible (less than 0.1 % of the pressure lift force (this is dependent on, *inter alia*, the angle of attack)). Hence, the pressure lift force is considered to be the total lift force.

With XFOIL, the total drag coefficient C_D is obtained by applying the Squire-Young formula [1938SQU] at the last point in the wake and is computed as follows:

$$C_D = 2\theta \left(\frac{u_{edge}}{U_\infty}\right)^{\left(\frac{H+5}{2}\right)}$$

(5.1)

where θ is the momentum thickness, u_{edge} is the edge velocity, H is the shape parameter.

In addition to calculating the total drag coefficient C_D from the wake momentum thickness, XFOIL also determines the friction (C_{Df}) and pressure (C_{Dp}) drag components of C_D. These are calculated with:

$$C_{Df} = \oint C_f \, d\bar{x} \tag{5.2}$$

$$C_{Dp} = C_D - C_{Df} \tag{5.3}$$

where C_{Df} is the skin friction coefficient defined with the free stream dynamic pressure and $\bar{x} = x\cos(\alpha) + y\sin(\alpha)$

The integrals are performed in the counter-clockwise direction around the airfoil contour. Note that C_{Dp} is not calculated via surface pressure integration but is deduced from C_D and C_{Df}. This is done as the surface pressure integration is typically swamped by numerical noise.

The lift coefficient C_L is calculated by direct surface pressure integration:

$$C_L = \oint C_P \, d\bar{x} \tag{5.4}$$

The pressure coefficient C_p is calculated using the Karman-Tsien compressibility correction. Transition prediction in XFOIL is accomplished using a simplified envelope procedure for the e^n-method [2001DRE].

Data of the same type is compared. The types of data are presented in Table 12.

Table 12: Summary of the types of data collected with EFD and generated by numerical methods

		Drag			Lift
		Viscous	Pressure	Total	Total
EFD	Pressure distribution		x		x
	Wake survey			x	
Numerical	XFOIL	x	x	x	x
	CFD – 2D	x	x	x	x

The columns of Table 12 will be used as sub-headings and will be presented in the order, as seen in the table, from left to right. The pressure drag results are not presented as they are similar to the total drag. Furthermore, the pressure drag can be deduced from the total and viscous drag. Only the results of the root and tip blade section are presented in this chapter. These two sections are seen as the extreme cases in terms of both Reynolds number (refer to Table B.1) and curvature of the blade section profile (see Figure A.1).

The computational predictions were obtained by solving the RANS equations in combination with turbulence models. Henceforth, predictions will be stated as if solved solely by turbulence models. For

instance "*k-ε* standard turbulence models best predicts" implies "simulation results implementing the *k-ε* standard turbulence model best predicts"

Figure 36 to Figure 40 present the results obtained for the force coefficients of the two blade sections. It should be noted that the figures, (a) and (b), have different horizontal scales.

5.1.1 Drag

Firstly the viscous and then the total drag results are presented in Figure 36, and Figure 37 to Figure 38, respectively.

5.1.1.1 Viscous Drag

In Figure 5.1, the viscous drag coefficients at various angles of attack are presented. Both XFOIL and the Trans-SST turbulence model do not assume flow to be fully turbulent but model the laminar flow before transition onset. The viscous drag (skin friction) coefficient is less for laminar flow than for turbulent flow. Therefore, the viscous drag computed is less for transitional models than fully turbulent models as shown in Figure 5.1. Trans-SST turbulence model best describes XFOIL's computations of the viscous drag. The *k-ε* realizable and Trans-SST turbulences models, respectively predict the highest and lowest computed viscous drag of the turbulence models.

(a)   (b)
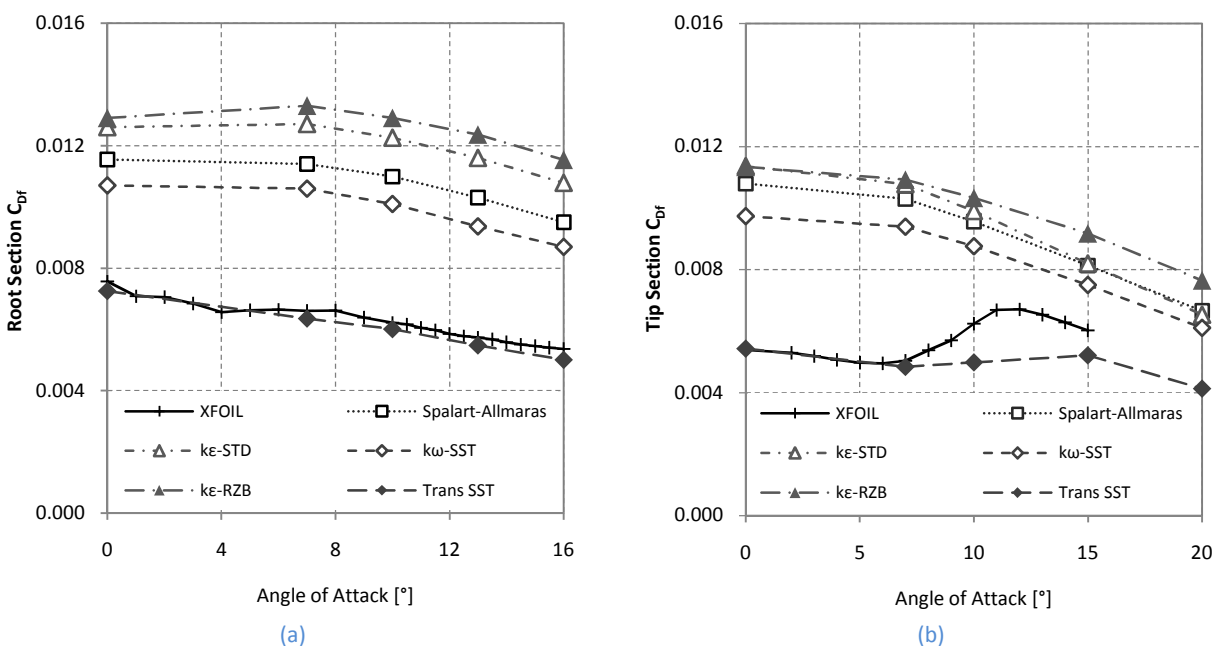
Figure 36: Viscous drag (skin friction) coefficient of the (a) root and (b) tip blade section (free domain)

5.1.1.2 Total Drag

In Figure 37 and Figure 38 the total drag coefficients at various angles of attack are presented. The correlation between CFD and XFOIL computations improve with increasing Reynolds number and decreasing curvature of the blade section profile, as seen in Figure 37. XFOIL constantly under predicts the total drag when compared to the CFD and experimental results. The Trans-SST turbulence model best describes the XFOIL computations of the total drag. The k-ε standard and the Trans-SST turbulence models, respectively predict the highest and the lowest computed total drag of the turbulence models.

(a)   (b)
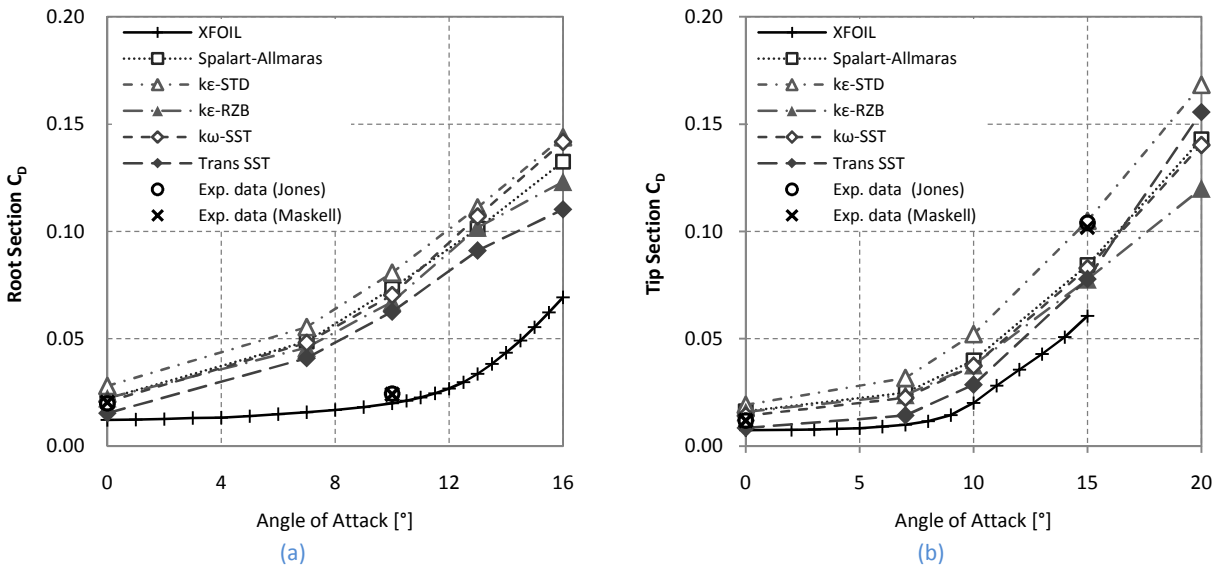
Figure 37: Total drag coefficient of the (a) root and (b) tip blade section (free domain)

In Figure 38, the Trans-SST and the k-ε standard turbulence models best predict the experimental data for the root and tip blade section, respectively. It is interesting to note that for both blade sections for angles of attack less than approximately 13 °, the Trans-SST turbulence model predicts the lowest total drag and above this angle of attack the k-ε realizable turbulence model does so.
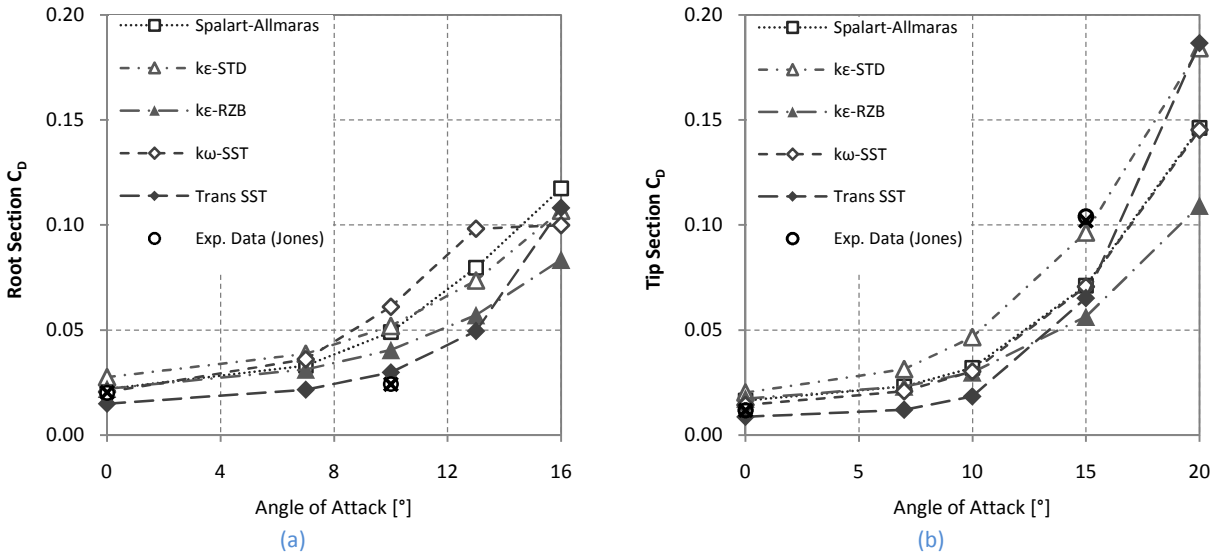
Figure 38: Total drag coefficient of the (a) root and (b) tip blade section (wind tunnel domain)

5.1.2 Lift – Total

In Figure 39 and Figure 40, the total lift coefficients at various angles of attack are presented. The correlation between CFD and XFOIL computations improve with increasing Reynolds number and decreasing curvature of blade section profile, as seen in Figure 39. XFOIL calculations show a too high C_{Lmax} and a too steep C_L slope when compared to experimental data. This was shown by Madsen and Filippone [1995MAD] to be a typical feature of XFOIL. Generally the highest and the lowest computed total lift is with the *k-ε* realizable and the *k-ω SST* turbulence models implemented, respectively.

In Figure 40, for the root blade section, the Splalart-Allmaras and the *k-ω SST* turbulence models perform poorly. Rumsey and Spalart [2008RUM] explained this poor performance by noting that at low chord Reynolds numbers it is likely that the turbulence models do not become activated over much of the airfoil surface. For the root blade section CFD under predict the total lift whilst over predicting the total lift for the tip blade section. The Trans-SST turbulence model best predicts the experimental data of the root blade section, however, prematurely predicting stall. The Trans-SST turbulence model, however correctly predicts the onset of stall for the tip blade section exclusively, although it underestimates the severity of the stall.

To evaluate the turbulence models, the deviation of the CFD results from the experimental data is summarized in Table 13. The computed and the measured lift and drag coefficients at certain angles of attack are presented. The values for the experimental lift coefficient and the experimental drag coefficient in the table were determined with the near-field and the far-field methods, respectively. The far-field method was favoured for determining the drag coefficient as the error estimate is significantly less than that of the near-field method (refer to Section 3.3.7.2).
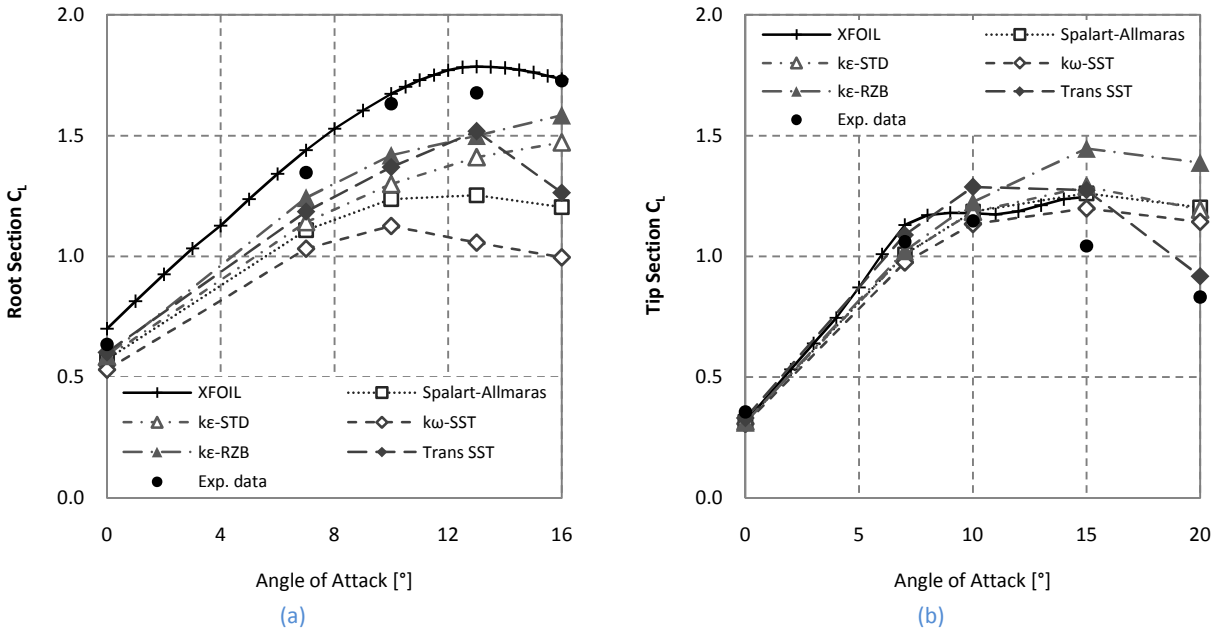
Figure 39: Total lift coefficient of the (a) root and (b) tip blade section (free domain)
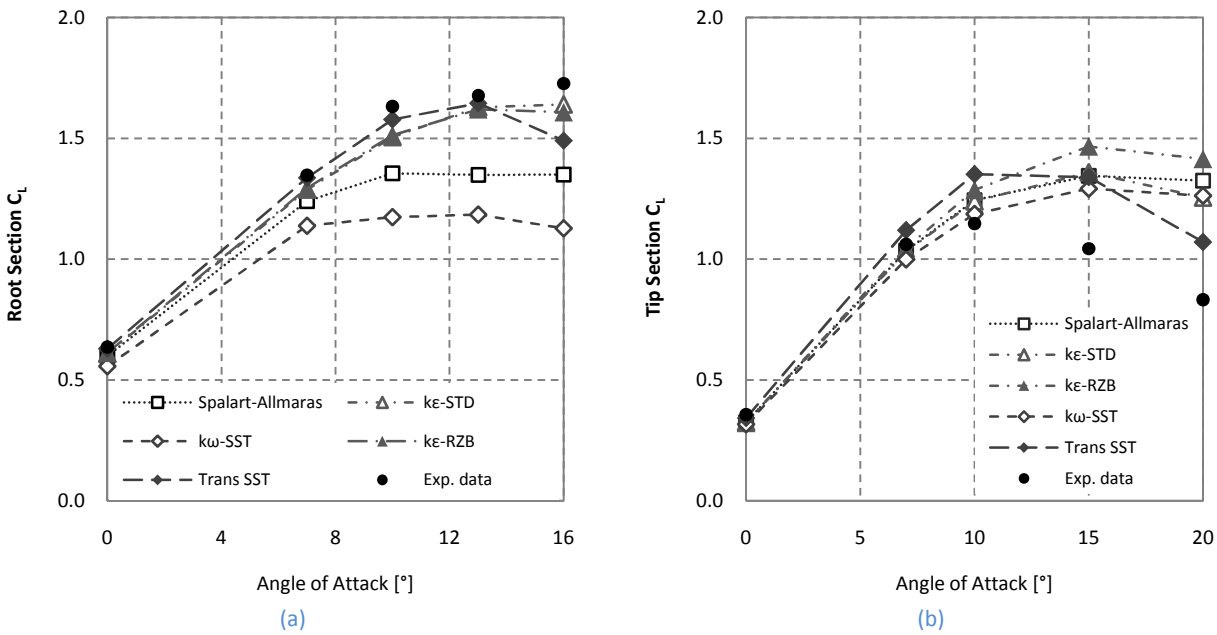
Figure 40: Total lift coefficient of the (a) root and (b) tip blade section (wind tunnel)

A threshold of 5 % of the deviation from the experimental data is taken to evaluate the influence of the turbulence model. The CFD results for each blade section are ranked in terms of their deviation from the experimental lift coefficient (best model on top). The deviations within the threshold are highlighted.

Table 13: Computed and measured aerodynamic coefficients for the blade sections (wind tunnel domain)

Blade section	Turbulence model	CFD C_L	C_D	Experiment C_L	C_D	Deviation $\Delta C_L < 5\%$	$\Delta C_D < 5\%$
Root	Trans SST	1.337	0.0298	1.347	0.024	-0.7	19.1
For C_L AOA = 7°	k-ε RZB	1.295	0.0405			-3.9	40.5
C_D AOA = 10°	k-ε STD	1.288	0.0519			-4.4	53.6
	S-A	1.240	0.0490			-8.0	50.8
	k-ω SST	1.138	0.0610			-15.5	60.5
Mid	k-ε RZB	1.339	0.0384	1.335	0.021	0.3	45.3
For C_L AOA = 9°	k-ε STD	1.325	0.0558			-0.8	62.3
C_D AOA = 12°	S-A	1.298	0.0462			-2.8	54.5
	Trans SST	1.418	0.0238			5.8	11.7
	k-ω SST	1.219	0.0541			-8.7	61.2
Semi	k-ω SST	1.086	0.0608	1.076	0.067	0.9	-9.3
For C_L AOA = 7°	S-A	1.121	0.0672			4.0	0.2
C_D AOA = 15°	k-ε STD	1.123	0.0945			4.2	29.1
	k-ε RZB	1.135	0.0945			5.2	29.1
	Trans SST	1.202	0.0566			10.5	-15.6
Tip	k-ε RZB	1.047	0.0563	1.062	0.102	-1.4	-44.8
For C_L AOA = 7°	S-A	1.035	0.0711			-2.5	-30.3
C_D AOA = 15°	k-ε STD	1.030	0.0965			-2.9	-4.9
	Trans SST	1.119	0.0651			5.2	-36.2
	k-ω SST	0.999	0.0706			-5.9	-30.7

The lift is well predicted with almost ¾ of the results within the threshold but the drag is poorly predicted with less than 10 % of results within the threshold.

The XFOIL results were not included in Table 13, as the CFD results presented in the table were computed on the wind tunnel grid domain. However, the deviation of XFOIL results from experimental data is presented in Table 14 to access the performance of XFOIL. XFOIL only provides one prediction within the threshold. This might indicate poor performance, but upon further investigation, the lift predictions are all within 10 %. Additionally, for the root and mid blade sections, XFOIL's drag predictions are considerably better than CFD's.

Table 14: Aerodynamic coefficients computed with XFOIL and measured for the blade sections

Blade section	XFOIL C_L	C_D	Experiment C_L	C_D	Deviation $\Delta C_L < 5\%$	$\Delta C_D < 5\%$
Root	1.441	0.0200	1.347	0.0241	6.5	-17.1
Mid	1.410	0.0216	1.335	0.0210	5.3	2.9
Semi	1.195	0.0554	1.076	0.0670	9.8	-17.3
Tip	1.130	0.0607	1.062	0.0570	6	-40.5

To further investigate the turbulence models' prediction of the flow domain, the best and worst turbulence models, in terms of their correlation with the experimental lift of Table 13, were selected. These models' predicted pressure distributions are compared to measured data in Figure 41 and Figure 42. The experimental data point at the trailing edge, indicated by a hollow circle, was not measured but assumed to be the mean value of adjacent pressure orifices of the blade section. CFD results showed this to typically be a valid assumption.
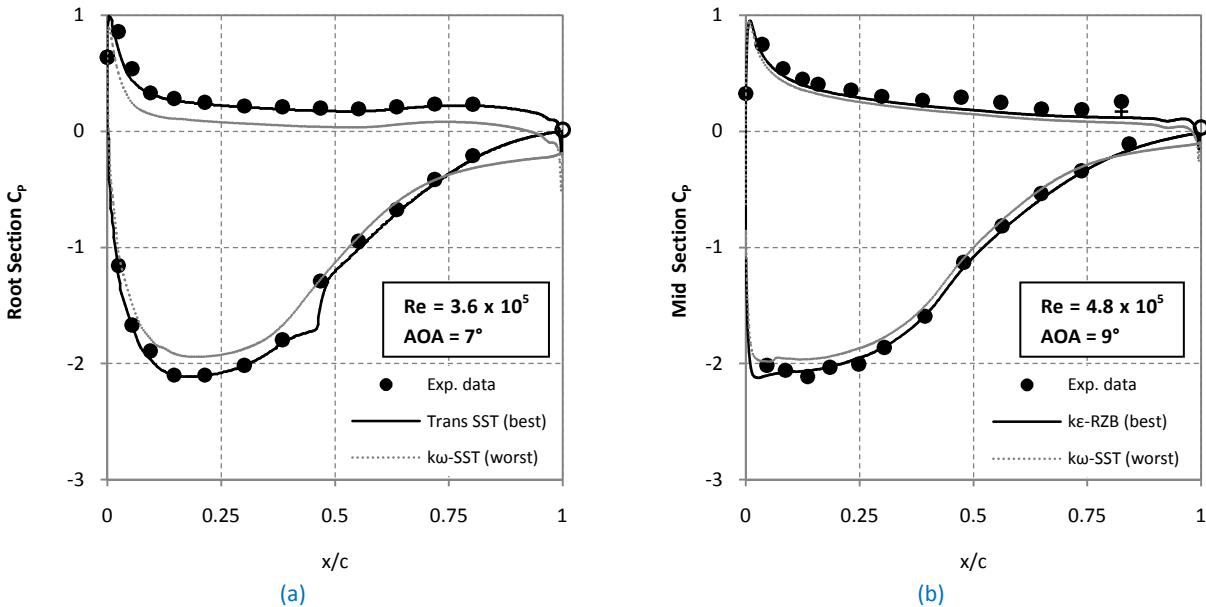
Figure 41: Measured and computed pressure distributions of the blade sections: (a) root and (b) mid

In general, the shapes of the measured pressure distributions are well predicted for both surfaces. The scatter of the computed results decrease with, increasing Reynolds number and decreasing curvature of the blade sections. Additionally, the computed pressure distributions move from "inside" to "outside" of the experimental data. This trend explains the under prediction and the over prediction of lift at the root and the tip blade section (Figure 40), respectively.

A laminar separation bubble (region between laminar separation and turbulent reattachment) is predicted in Figure 41 (a) by the Trans-SST turbulence model. As expected, the other turbulence models did not predict this as the respective flow is considered to be fully turbulent over the entire blade section surface. The laminar separation and the turbulent reattachment occur at approximately 37 and 48 % chord length, respectively. Unfortunately, the spacing of the pressure orifices on the surface of the root blade section at 7 ° angle of attack of did not allow for the presence of the bubble to be validated.

Fortunately, the pressure distributions at other angles of attack, namely 0 and 10 °, also obtained with the Trans-SST turbulence model of the root blade section, shown in Figure 43, could be used for validation purposes. The existence of a bubble is also revealed with the experimental data. Hence, the

Trans-SST model correctly predicts the presence of the laminar separation bubble of the root blade section.
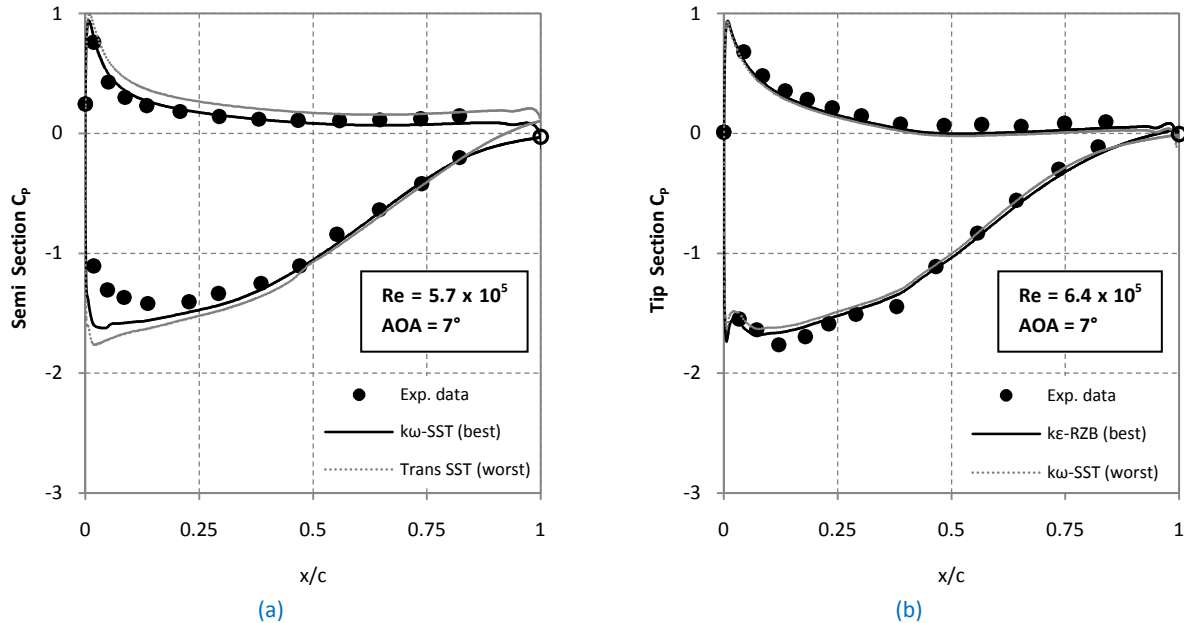
Figure 42: Measured and computed pressure distributions of the blade sections: (a) semi and (b) tip

On many airfoils with relatively large upper-surface curvatures, high local curvature over the forward part of the chord may initiate laminar separation. Small disturbances grow much more readily at low Reynolds numbers in separated, as compared to attached boundary layers. Consequently, the separated laminar boundary layer may well undergo transition to turbulence with characteristic rapid thickening. This rapid thickening may be sufficient for the lower edge of the, now-turbulent, shear layer to reattach as a turbulent boundary layer on the surface [2005HOU]. The root section has a relatively large upper-surface curvature as seen Table A.1 (d). This coupled with the relatively low chord Reynolds number flow at which the wind tunnel tests of the root blade section model were performed elucidate the presence of the measured laminar separation bubble not to be unusual.

If the Reynolds number is increased sufficiently, the transition location moves forward of the point where the laminar separation would occur. In effect, a turbulent boundary layer is formed and this prevents a bubble from forming. Additional CFD simulations implementing the Trans-SST model were performed at sufficiently high Reynolds number (2×10^6) as noted by [2002MAU] to ensure that the separation bubble is suppressed. This data is used to assist with establishing the boundaries of the bubble as seen in Figure 43. Laminar separation and turbulent reattachment occur at approximately 40 and 55 % chord length, respectively for 0 ° angle of attack and at approximately 32 and 42 % chord length, respectively for 10 ° angle of attack. With increasing angles of attack, the bubble moves towards

the leading edge and decreases in length. This was also found by Maughmer *et al*. [2002MAU] with the wind tunnel testing of a winglet at similar Reynolds number.

(a)   (b)
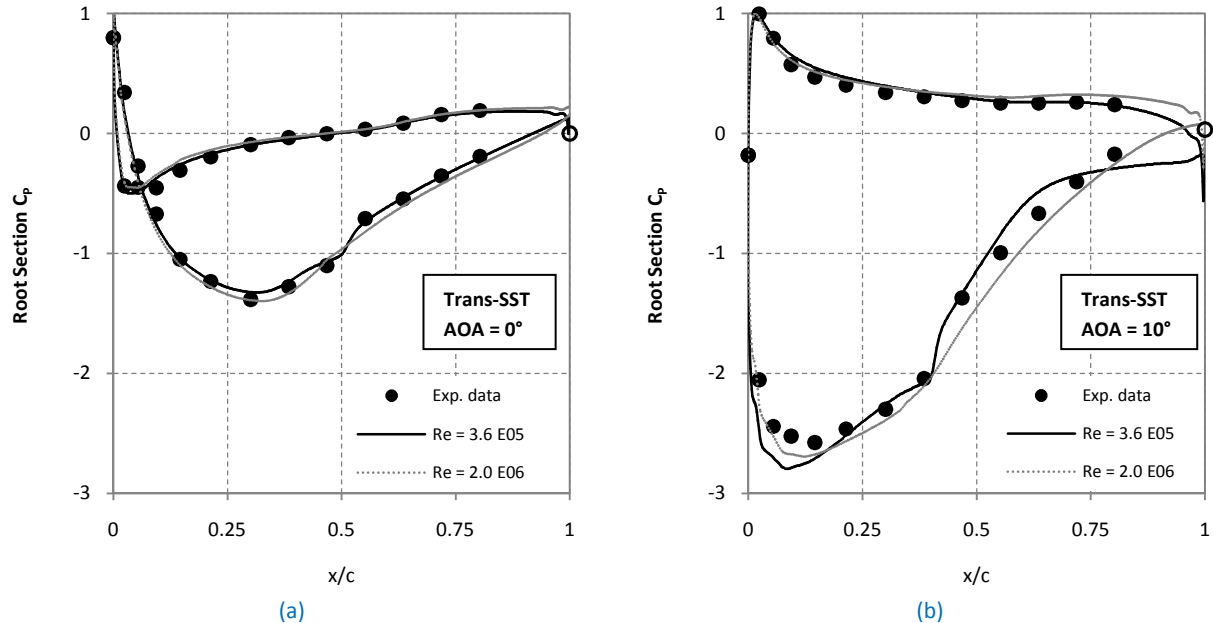
Figure 43: Measured and computed pressure distributions of the root blade section at (a) 0 ° and (b) 10 ° angle of attack

As mentioned, the laminar separation usually induces transition. This induced transition allows the flow to remain attached for larger angles of attack [1982MUE]. This feature of laminar separation bubbles may explain the delay of stall as seen in Figure 40 (a).

To investigate the predictive accuracy of the turbulence models in the wake region, the corresponding predictions are compared with the experimental wake survey data. This is achieved by comparing the measured and computed wind velocity deficit in the free stream direction, $\Delta V_x = V - V_{wake,x}$. To reduce the influence of the experimental uncertainty, the wake survey data of the tip blade section was favoured as the mean value for ΔV_x was the highest. This comparison is shown in Figure 44. The horizontal axis, Δy_{te}, is aligned with the trailing edge of the blade section (y = 0), and is positive in the direction of the lift force (refer to Figure 2.1).

The crest (location of maximum $|\Delta V_x|$) of the computed results is not modelled, as can be seen in Figure 44 (a), as a result of inadequate grid spacing, Therefore, for future studies grid refinement needs to be performed in the wake region of the blade sections. It is recommended that grid points coincide with the locations of the traverse measuring points. The grid point spacing for the 15 ° angle of attack case was adequate and crests were modelled, however, the experimental crest was not captured.
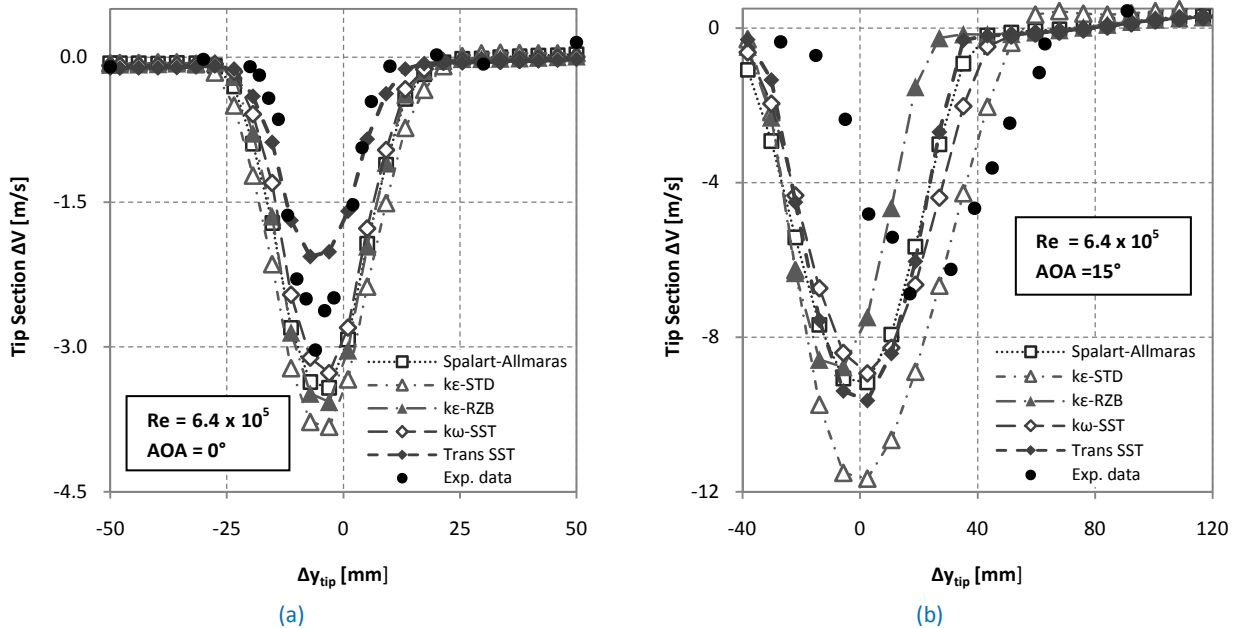
Figure 44: Measured and computed $V_{deficit,x}$ for the tip blade section at (a) 0 ° and (b) 15 ° angle of attack

The shape of the wake and the maximum $|\Delta V_x|$ are reasonably well predicted. However, the difference between the measured and computed location of ΔV_x is considerable. The CFD results predict the wake crest location to be approximately aligned with the trailing edge of blade section, whilst the measurements show the crest location to be positive in terms of the convention used for Δy_{te} (downstream of model).

As mentioned, for both blade sections for angles of attack less than approximately 13 °, the Trans-SST turbulence model predicts the lowest total drag and above this angle of attack the the k-ε realizable turbulence model does so. This is also evident in Figure 44 as the areas under the graphs are proportional to the total drag.

5.2 Performance Prediction

The ultimate goal of this investigation is to predict the performance of a wind turbine comprising of the blade design from [2006CEN]. The turbine rotor was defined from 20 % (root) to 90 % (tip) radius as well as the radius of the hub. The undefined sections were determined in Section 4.2.1.1; resulting in the definition of the complete geometry of the wind turbine (see Figure 31). The performance predictions of the wind turbine utilizing CFD are presented in this section.

The predicted flow is fully attached. This is shown in Figure 46. The performance is assessed in terms of C_P. The C_P predictions of Section 4.2 are presented in Table 15, below.

Table 15: C_P predictions of the wind turbine (CFD)

Spalart-Allmaras		k-ω SST	k-ε Yang-Shih (Low Re)	k-ε non linear (Low Re)
Fully Turbulent	With Transition	Fully Turbulent	Fully Turbulent	Fully Turbulent
0.440	0.449	0.564	0.565	0.480

The C_P predictions presented vary considerably, with a 22 % difference between extremes. This seems high when considering the flow is attached but Benjanritat and Sankar [2003BEN] found that most of the turbulence models implemented had problems with modelling, *inter alia*, the low speed shaft torque (LSSTQ) even for attached flows. For instance, at 7 m/s wind speed the lowest and highest LSSTQ predictions obtained with various eddy-viscosity models (Baldwin-Lomax zero equation model not included) differed by 42 %. Also see Figure 2. The C_P predicted during the original design process was 0.51 [2006CEN]. This is within the predicted range.

The small difference, 2 %, between the C_P predicted implementing the Spalart-Allmaras turbulence model in fully turbulent and transitional mode is investigated by considering the intermittency over the wind turbine rotor, Figure 45. The white line on the rotor represents the transition location.

Figure 45: Intermittency plot of wind turbine rotor as seen from upstream (top) and downstream (bottom)

The transition location varies from approximately ⅙ chord at the hub to approximately ⅓ chord at the tip. With transitional modelling, the viscous drag predicted is less than predictions obtained with modelling the flow as fully turbulent over the entire airfoil surface. This is evident when comparing the relative differences between the viscous and total drag computed by the *kω*-SST and Trans-SST

turbulence models, as shown in Figure 36 and Figure 37. The viscous drag was found with two-dimensional CFD modelling to typically be one order of magnitude less than the pressure drag. Thus, the influence of the reduction of viscous drag on the performance of the wind turbine is relatively small.

To investigate the effect of transitional modelling on the wind turbine rotor's performance across the span, sectional airfoil characteristics were extracted from the computations. The C_p distributions obtained with Spalart-Allamaras in fully turbulent and transitional mode at the four blade sections were shown to be similar. Transitional modelling was found to be detrimental in terms of lift at the root blade section, with increasing radii this transitioned to higher lift predicted at the tip blade section. At the semi blade section, the distribution was essentially the same. Therefore, the difference between the C_P predictions implementing Spalart-Allmaras in fully turbulent and transitional mode is minimal.

The k-ω SST and k-ε Yang-Shih (Low Re) turbulence models predicted C_P suspiciously high, 4.5 % less than the Betz limit. The measured C_P of Enercon's $E33$ blade, at 56 % [2007REF], shows that these high C_P 's are attainable.

Relevant experimental data is required to access the predictive accuracy of the turbulence models. However, in Section 5.3.2 an estimate for the lower limit of C_P is established.

5.3 Transition to Three-Dimensional Flow

As noted in Section 4.1.6 discrepancies can be expected between, firstly the sectional airfoil characteristics (rotating blades) and two-dimensional airfoil characteristics (non-rotating), and secondly the performances predicted by the BEMT method and the three-dimensional methods described in Section 4.2. In this section these discrepancies are investigated.

5.3.1 Effect of Rotation

The effect of rotation on the blade sections is investigated by considering the CFD results for both the rotating and non-rotating (static) case. The Spalart-Allmaras and the k-ω SST turbulence models are used for both the two- and three-dimensional CFD modelling. Therefore, the respective results obtained with these models are compared. For brevity, only the results of the Spalart-Allmaras turbulence model are presented. The sectional characteristics are extracted from the three-dimensional computations of the rotating wind turbine and compared to corresponding two-dimensional airfoil characteristics.

The free grid domain of the two-dimensional CFD modelling represents the flow domain of the three-dimensional CFD modelling of the wind turbine better than the two-dimensional wind tunnel grid

domain. Therefore, the results of the two-dimensional CFD modelling simulations on the free grid domain are used for comparison.

The local angle of attack for the rotating case is determined by considering the relative angle of the upstream flow, Figure 46 (figure is not drawn to scale). The similar non-rotating case in terms of angle of attack is also shown at the bottom of the figure. Equivalence in terms of angle of attack for the root blade section could not be attained as the local angle of attack for the rotating case is greater than the respective maximum angle of attack simulated.It is evident that separation is suppressed in the rotating case. As mentioned, this was also found by [1999DU]. To investigate the effect of the delayed separation the pressure distributions, Figure 47 and the resultant lift, Figure 48 are compared for the rotating and non-rotating cases. In Figure 48, the respective lift coefficients, including the k-ω SST turbulence model results, of the non-rotating and rotating blade sections are indicated with lines and markers, respectively.
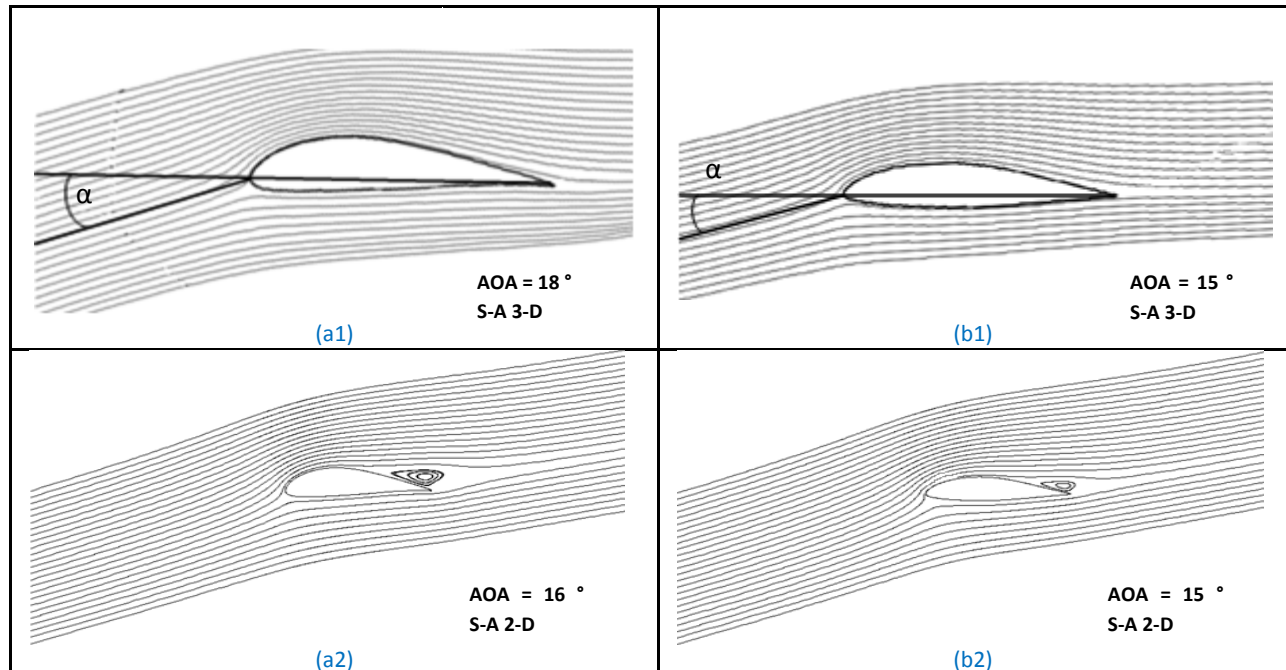
Figure 46: Streamlines of (a) root and (b) tip blade section (rotating case on top)

The beneficial effects of rotation are most evident at the inner section of the wind turbine blade. These beneficial effects diminish with increasing radii, with a relative decrease in lift near the tip induced by the tip vortices. As mentioned, these findings were also noted by [1999DU]. Additionally, the beneficial effects of rotation are more prevalent with the k-ω SST turbulence model predictions than those of the Spalart-Allmaras turbulence model.
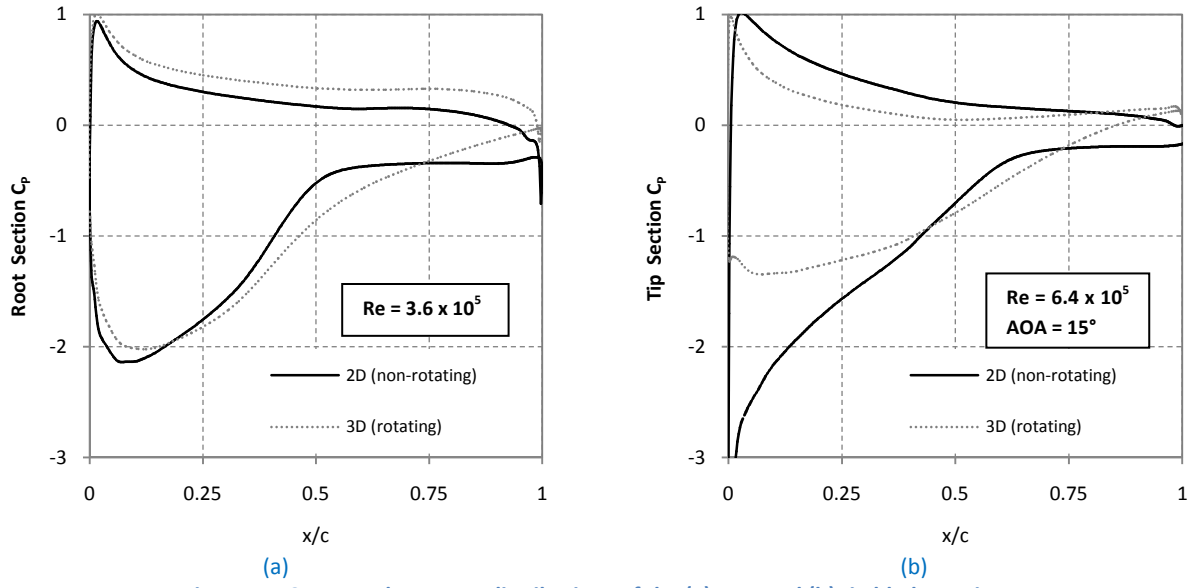
Figure 47: Computed pressure distributions of the (a) root and (b) tip blade section
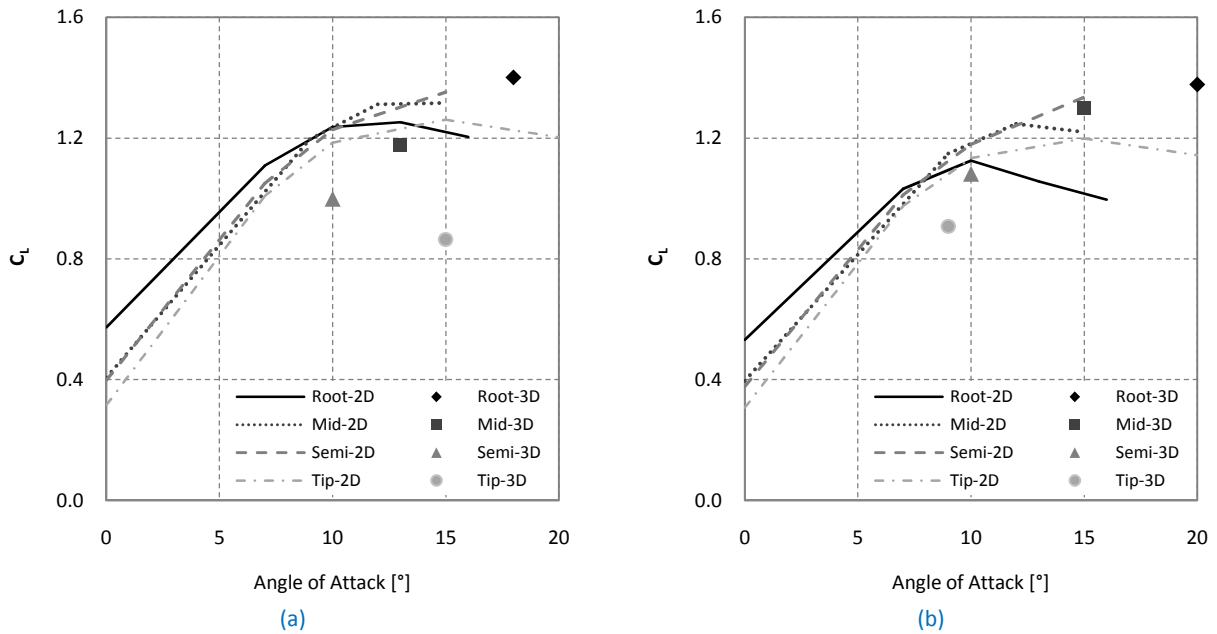
Figure 48: Lift coefficients from CFD 2D (lines) and CFD 3D (markers) with (a) Spalart-Allmaras and (b) *k-ω* SST

5.3.2 Blade Element Momentum Theory (BEMT) Method

BEMT is described in [1993HAN]. This section deals with the application of this method to the wind turbine blade.

A Matlab © program was written based on the BEMT model of Glauert [1935GLA]. The cases with and without the traditional corrections are considered. Two corrections are applied to the algorithm, namely Prandtl's tip- loss factor and the Glauert correction for high values of the axial induction factor. The former corrects the assumption of an infinite number of blades. It has been shown that the simple momentum theory breaks down with axial induction factors larger than a critical value (a_c), of approximately 0.4. The second correction compensates for this with the empirical evaluation of the thrust coefficient given by Spera; utilizing a value for a_c of 0.2.

Required data for BEMT is available for the majority of the rotor blade; from 20 to 90 % R_{rotor}. The lift- and drag coefficients obtained from the CFD simulations on the free-domain grid are used.

The effect of the traditional corrections and the influence of the inner blade sector (hub (10 % R_{rotor}) to 20 % R_{rotor}) with regards to mechanical shaft power output are investigated. The tangential force at hub radius is considered zero and a linear variation between the radial stations is assumed, Figure 49. The resultant power predictions are presented in Table 16.
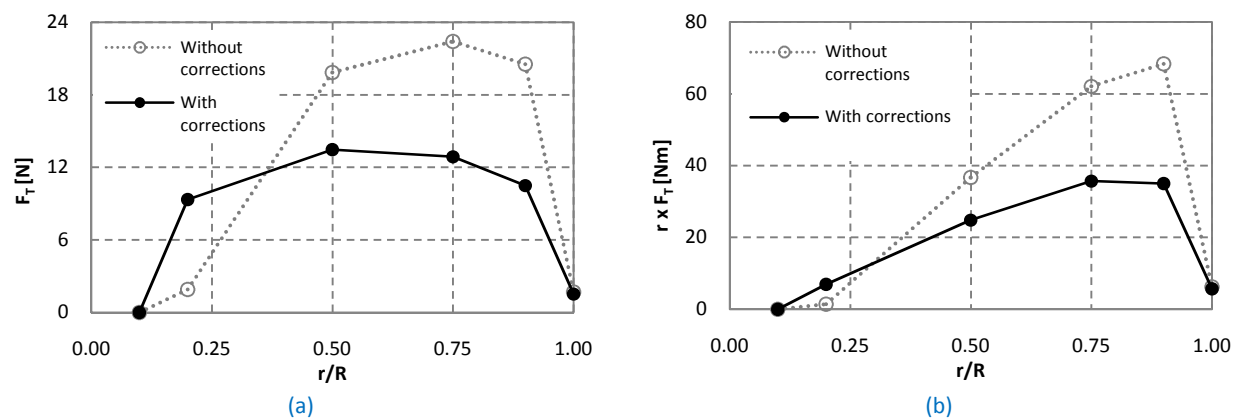
Figure 49: BEMT calculations with and without corrections (a) tangential force at radial sections, (b) product of the radial arm and tangential force

Table 16: Power prediction with BEMT (S-A)

Blade section [%]	Corrections Applied	
	No	Yes
20 to 100	3.043	1.818
10 to 100	3.049	1.859
Difference [%]	0.20	2.21

The applied corrections have a significant effect on the power predictions. As expected, the inner region has minimal influence on the mechanical shaft power output. Nevertheless, the results of 10 to 100 % blade section case are used. With the corrections applied, the BEMT power predictions implementing the respective force coefficients are calculated. The resultant C_P, calculated with Equation (4.3), is compared to the results of the three-dimensional CFD modelling of the rotating wind turbine in Table 17, below.

Table 17: Comparison of C_P predictions using BEMT and CFD-3D

	Exp. Data	XFOIL	S-A	k-ω SST	$k\varepsilon$-STD	$k\varepsilon$-RZB	Trans-SST
BEMT	0.481	0.514	0.429	0.430	0.399	0.418	0.477
CFD -3D			0.440	0.564			

Table 17 shows the beneficial effects of rotation with the higher C_P predictions of the three-dimensional CFD modelling of the rotating wind turbine compared to those obtained with BEMT. As mentioned, the beneficial effects of rotation are more prevalent with the CFD simulations employing the k-ω SST turbulence model than those utilizing the Spalart-Allmaras turbulence model. This, as expected, was also found in Table 17.

In this section BEMT is found to pessimistic in terms of C_P predictions when compared to the three-dimensional CFD simulation results. The predicted turbine performance with BEMT has also been found to be pessimistic compared to that encountered in the field [2002TAN]. For example the, NREL Combined Experiment (Phase II) turbine exceeded predictions by approximately 15-20 % [1993HAN]. From these findings, the prediction of BEMT utilizing the experimental data can be considered a lower limit for C_P. It should be noted that the experimental data was obtained in a wind tunnel, and, hence field conditions were not precisely represented.

From the two-dimensional CFD results, the lift and drag predicted utilizing the wind tunnel domain grid is, respectively, higher and lower than the predictions implementing the free domain grid. This is considerable at the root blade section but with increasing Reynolds number and decrease in curvature of the blade section profile the solutions become less dependent on the choice of grid domain. Most of the torque is produced at around ¾ span (refer to Figure 49 (b)). Thus, field conditions not being precisely represented does not have a significant effect on the torque prediction with BEMT incorporating wind tunnel experimental data and, hence, the proposed lower limit of C_P is valid.

6. Conclusions and Recommendations

6.1 Conclusions

The aerodynamic characteristics of a wind turbine blade were investigated.

The two main objectives of this thesis as noted in Section 1.2 were to attain the aerodynamic characteristics of the blade sections which constitute the proposed wind turbine blade of [2006CEN] and to predict the C_P of a wind turbine incorporating the proposed blade design at operating conditions. The conclusions with regards to the two objectives will be dealt with, in the order presented.

Aerodynamic Characteristics

The predictive accuracy of five eddy-viscosity models is compared to each other and to experimental data. In general, the shapes of the measured pressure distributions are well predicted when implementing the various turbulence models but the corresponding values for the lift and drag differ sometimes considerably. The lift was better predicted than the drag. For the root blade section (Re = 3.6 x 10^5), the lift was under predicted and with increasing Reynolds number (Re = 6.4 x 10^5) and decreasing curvature of the blade section profile toward the tip blade section the lift was over predicted.

For the root blade section, the importance of transitional modelling was highlighted with the Trans-SST shown to be superior to the fully turbulent models considered. With the Trans-SST turbulence model the presence of laminar separation bubbles was correctly predicted. With increasing angles of attack the bubbles were shown to move towards the leading edge and decrease in length. For the tip blade section, the computations implementing the kε-realizable turbulence model best agreed with experimental measurements.

The correlation between the turbulence models' and XFOIL's results were better for the tip blade section than for the root blade section. From the turbulence models considered, the simulations results implementing the Trans-SST turbulence model best agreed with XFOIL computations. XFOIL typically under predicted the drag and constantly over predicted the lift. This has a significant effect on the lift-to -drag ratio.

Coefficient of Power

The coefficient of power predictions varied considerably with turbulence model utilized, varying from 0.440 to 0.565. The C_P predicted during the original design process was 0.51 [2006CEN]. Relevant experimental data is required to access predictive accuracy of the turbulence models.

The effect of rotation was investigated by extracting sectional airfoil characteristics from the three dimensional modelling computations and comparing to two-dimensional airfoil characteristics (non-rotating). The delay of stall is found for the rotating case; resulting in beneficial effects which diminish with increasing radii of the wind turbine rotor.

A lower limit of 0.481 for the coefficient of power of the wind turbine is proposed, based on the Blade Element Momentum method implementing the results the of two-dimensional wind tunnel testing of the blade sections.

6.2 Recommendations

As mentioned, this thesis forms part of a larger research project. It is recommended that three-dimensional experimental testing of the simulated wind turbine be realized. This could be used to validate the findings presented in Section 5.2.

Further recommendations with regards to EFD and CFD are given next.

EFD

Upgrade or replace the manual actuated mechanism utilized for adjusting and setting the angle of attack in the low-speed wind tunnel used for experimental testing. This will reduce the uncertainty of the angle of attack and, thus, the corresponding experimental uncertainty. For convenience and reduction of the wind tunnel operational time, the traverse mechanism used to traverse the probe in the wake of the models could be automated. The effect of free stream turbulence and surface finish of the blade sections on the performance characteristics of the blade sections could be investigated. This would provide valuable data with regards to the operation of the wind turbine in field conditions.

CFD

Two-dimensional simulations of the blade sections implementing the RSM turbulence model were performed. The model became unstable at high angles of attack, and, hence the respective results were not included in this thesis. Further investigation into the implementation of the RSM turbulence model needs to be performed, as to investigate the effect of the Boussinesq hypothesis applied to turbulence models used. Grid refinement needs to be achieved in the wake region of blade section as to model this region more accurately. This data could be used to determine lift and drag from the far-field drag decomposition method.

Perform three-dimensional simulations of the wind turbine implementing the detached eddy simulation (DES) turbulence model with near-wall treatment. DES with near wall treatment with $k\omega$-SST has been shown to be superior for this application to other classical turbulence models such as the $k\omega$-SST [2007MEN]. Investigate the sensitivity of the wind turbine, in terms of C_P, to varying wind speeds. Attempts could be made to isolate the spurious drag from the flow data of Section 4.2 by applying the mid-field drag decomposition methods. This could decrease computational costs by reducing the required grid points, as shown by [2008YAM].

List of References

[1915LAN]   Lanchester, F. W., A Contribution to the Theory of Propulsion and the Screw Propeller, Trans Inst Naval Archi, 1915: p. 57 – 98

[1935GLA]   Glauert, H., Aerodynamic Theory, Vol. 4, Berlin, Germany, Julius Springer, 1935: p. 169 - 360

[1936GOL]   Goldstein, S., A Note on Measurement of Total and Static Pressure in a Turbulent Stream, Proceedings of the Royal Society, 155, p.570, 1936

[1936JON]   Jones, B. M., The Measurement of Profile Drag by the Pitot-Traverse Method. Reports and Memoranda No. 1688, (British) Aeronautical Research Committee, January 1936.

[1938GOL]   Goldstein, S., Modern Developments in Fluid Dynamics, Vol. 2, p. 331, Oxford University Press, NY, 1938

[1938SQU]   Squire, H. B., Young, A. D., The Calculation of the Profile Drag of Airfoils, ARC RM 1838, (1938).

[1947HIM]   Himmelskamp, H., Profile Investigations on a Rotating Airscrew, Dissertation, Göttingen, 1945, (Reports and Translations No. 832, 1947)

[1970WRI]   Wright, M. A., The Evaluation of a Simplified Form of Presentation for Five-Hole Spherical and Hemispherical Pitotmeter Calibration Data, Journal of Physics E., Scientific Instruments, Volume 3, pp.356-362, 1970

[1972LAU]   Launder, B. E., Spalding, D. B., Lectures in Mathematical Models of Turbulence, Academic Press, London, England, 1972

[1972MAS]   Maskell, E.C., Progress Towards a Method for the Measurement of the components of Drag of a Wing of Finite Span, RAE Technical Report 72232, 1972

[1972TEN]   Tennekes, H., Lumley, J. L., A First Course in Turbulence, MIT Press, Cambridge, MA

[1975HIN]   Hinze, J. O., Turbulence, McGraw-Hill Publishing Co., New York, 1975

[1980ABU]   Abu-Ghannam, B.J., Shaw, R., Natural Transition of Boundary layers – The Effects of Turbulence, Pressure Gradient and Flow History. J. of Mech. Eng. Sci. 22, pp. 213–228, 1980

[1981SIT]   Sitaram, N., Lakshminarayana, B., Ravindranath, A., Conventional Probes for the Relative Flow Measurement in a Turbomachinery Rotor Blade Passage, Department of Aerospace Engineering, Pennsylvania State University, 1981

[1982MUE]   Mueller, T. J., Batill, S. M., Experimental Studies of Separation on a Two-Dimensional Airfoil at Low Reynolds Numbers, AIAA Journal, Vol. 20 No. 4, 1982

[1986GOR]   Gorski, J. J., A New Near-Wall Formulation the k-ε Equations of Turbulence, AIAA 24th Aerospace Sciences Meeting, January 6-9, Reno, Nevada, AIAA-86-0556, 1986

[1986ROA]   Roache, P. J., Ghia, K. N., White, F. M., Editorial policy Statement on the Control of Numerical Accuracy, ASME Journal of Fluids Engineering, 108, p.2, 1986

[1987SPE]   Speziale, C. G., On Non-Linear K-l and K-ε Models of Turbulence, Journal of Fluid Mechanics 178 : 459-475, 1987

[1988MAD]   Madsen, H. A., Rasmussen, F., Derivation of Three-Dimensional Airfoil Data on the Basis of Experiment and Theory, AWEA Conference, Honolulu, HI, 1988

[1988RAS]   Rasmussen, F., Petersen, S. M., Larsen, G., Kretz, A., Andersen, P. D., Investigations of Aerodynamics, Structural Dynamics and Fatigue on Danwin 180 kW, Riso-M-2727, Risø National Laboratory, Riskilde, 1988

[1991RON]   Ronstein, G., Static Pressure Measurements on a Rotating and Non-Rotating 2.375 m Wind Turbine Blade-Comparison with 2-D Calculations, EWEC 1991, Amsterdam, 1991;214-220

[1992MEN]   Mentor, F. R., Performance of Popular Turbulence Models for Attached and Separated Adverse Pressure Gradient Flow, AIAA, Vol. 30, pp. 2066-2072, 1992

[1992SPA]   Spalart, P., Allmaras, S., A One-Equation Turbulence Model for Aerodynamic ows, Technical Report AIAA-92-0439, 1992.

[1993CEL]   Celik, I., Numerical Uncertainty in Fluid Flow Calculations: Needs for Future Research, ASME Journal of Fluids Engineering, 115, pp. 194-195, 1993

[1993HAN]   Hansen, A. C., Butterfield, C. P., Aerodynamics of Horizontal-Axis Wind Turbines, Annu. Rev. Fluid Mech. 1993; 25:155-49

[1993SCH]   Schetz, J. A., Boundary Layer Analysis, Prentice Hall, New Jersey, U.S.A., 1993

[1994BAR]   Barrett, R., Berry, M., Chan, T. F., Demmel, J., Donato, J., Dongarra, V., Eijkhout, V., Pozo, R., Romine, C., Van der Horst, H., Templates for the Solution of Linear Systems: Building Blocks for Iterative Methods, SIAM, Philadelphi, Pennsylavania, 2nd Edition, 1994

[1994MEN]   Mentor, F. R., Two-Equation Eddy-Viscosity Turbulence Models for Engineering Applications. AIAA Journal, 32(8):1598{1605, August 1994.

[1994WIL]   Wilcox, D. C., Turbulence Modelling for CFD, DCW Industries, California, U.S.A., 1994

[1995MAD]   Madsen, H. A., Filippone, A., Implementation and Test of the XFOIL Code for Airfoil Analysis and Design, Risø-R-644(EN), Risø National Laboratory, Denmark, 1995

[1995RAM]   Ramsey, R. R., Hoffman, M. J., Gregorek, G. M., Effects of Grid Roughness and Pitch Oscillations on the S809 Airfoil, NREL TP-442-7817, 1995

[1995SHI]   Shih, T. H., Liou, W. W., Shabbir, A., Yang, Z., Zhu, J., A New k-ε Eddy-Viscosity Model for High Reynolds Number Turbulent Flows - Model Development and Validation, Computers Fluids, 24(3):227{238, 1995.

[1995WOL]   Wolfe, W. P., Ochs, S., CFD Calculations of S809 Aerodynamic Characteristics, 1997 ASME Energy Symposium, 1997

[1997BAR]   Bardina, J. E., Haung, P. G., Coakley, T. J., Turbulence Modeling Validation, AIAA Paper 97-2121, 1997

[1998AIA]   AIAA, Guide for the Verification and Validation of Computational Fluid Dynamics Simulations, AIAA Guide G-077-1998, 1998

[1998FUG]   Fuglsang, P., Antoniou, I., Søreson, N. N., Madsen, H. A., Validadation of a Wind Tunnel Testing Facility for Blade Surface Pressure Measurements, Risø National Laboratory, Roskilde, Risø

[1998WIL]   Wilcox, D. C., Turbulence Modeling for CFD, 2nd Edition, DCW Industries, La Cānada, CA, 1998

[1999BAR]   Barlow, J. B., Rae, W. H., Pope, A., Low-Speed Wind Tunnel Testing, Wiley, New York, 1999

[1999DU]   Du, Z., Selig, M. S., The effect of rotation on the boundary layer of a wind turbine blade, Renewable Energy 20, 167-181, 1999

[2000ERC]   ERCOFTAC, Best Practice Guidelines, Version 1.0, M. Casey, T. Wintergerste (eds), ERCOFTAC Special Interest Group on Quality and Trust Industrial CFD, 2000

[2000MOI]   Moitra, A., Unstructured Grid Issues in 2-D High-Lift Computations, Proceedings of the 7th International Conference on Grid Generation in Computational Field Simulations, International Society of Grid Generation, Whistler, BC, Canada, September 2000, pp 263-274

[2000SPA]   Spalart, P. R., Allamaras, S. R., A One-Equation Turbulence Model for Aerodynamic Flow, AIAA Paper 92-0439, January 1992

[2001BEL]   Bell, S., A Beginner's Guide to Uncertainty of Measurement, Centre for Basic, Thermal and Length Metrology, National Physical Laboratory, 2001

[2001DRE]   Drela, M., Youngren, H., XFOIL 6.9 User Primer, MIT Aero. & Astro., 2001

[2001FIN]   Fingersch, L. J., Simms, D., Hand, M., Jager, D., Cortell, J., Robinson, M., Schreck, S., Larwood, S., Wind Tunnel Testing of NREL's Unsteady Aerodynamics Experiment, AIAA Paper 2001-0035, 39th Aerospace and Sciences Meeting, Reno, NV, Jan, 8-11, 2001

[2001SIM]   Simms, D., Schreck, S., Hand, M., and Fingersh, L., NREL Unsteady Aerodynamics Experiment in the NASA-Ames Wind Tunnel: A Comparison of Predictions to Measurements, NREL/TP-500-29494, June 2001

[2002LEI]   Leishman, J. G., Challenges in Modeling the Unsteady Aerodynamics of Wind Turbines, AIAA-2002-0037, 2002.

[2002MAU]   Maughmer, M. D., Swan, S. S., Willits, S. M., Design and Testing of a Winglet Airfoil for Low-Speed Aircraft, Journal of Aircraft, Vol. 39, No. 4, July-August 2002

[2002MOI]   Moitra, A., Automated CFD Analysis of Two-Dimensional High-Lift Flows, Journal of Aircraft, Volume 36, No.4, July-August 2002, pp 662-667

[2002OBE]   Oberkamp, W. L., Trucano, T. G., Verification and Validation in Computational Fluid Dynamics, Prog. Aerosp. Sci., Vol. 38 pp. 209 -272, 2008

[2002TAN]   Tangler, J. L., The Nebulous Art of using 2D Wind Tunnel Results for 3D Performance Prediction, NREL/CP-500-31243, 2002

[2003BEN]   Benjanirat, S., Sankar, L. N., Evaluation of Turbulence Models for the Prediction of Wind Turbine Aerodynamics, AIAA-2003-0517, 2003

[2003MEN]   Mentor, F. R., Kuntz, M., Langtry, R., Ten Years of Industrial Experience with the SST Turbulence Model, Proceedings of the Fourth International Symposium on Turbulence, Heat and Mass Transfer, Begell House, Reddings, CT, 2003

[2004CEL]   Celik, I. B., Procedure for Estimation and Reporting of Discretization Error in CFD Applications, Internal Report, Mechanical and Aerospace Engineering Department, West Virgina University, Morgantown Wv, USA, 2004

[2004ECK]   Eck (van Eck), H., Modellering van Horisontale Stabiliseerder van die Oryx Helikopter (Modelling of the Horizontal Stabilizer of the Oryx Helicopter), Undergraduate Project, Department of Mechanical Engineering, University of Stellenbosch, 2004

[2004HEM]   Hemsch, M. J., Morrison, J. H., Statistical Analysis of CFD Solutions from 2nd Drag Prediction Workshop, AIAA Paper 2004-0556, 2004.

[2004JOH]   Johansen, J., Sorenson, N. N., Aerofoil Characteristics from 3D CFD Rotor Computations, Wind Energ. 2004; 7:283-294

[2004KIR]   Kirstein, C., Flow Through a Solar Chimney Power Plant Collector-to-Chimney Transition Section, Master's Thesis, Department of Mechanical Engineering, University of Stellenbosch, 2004

[2004PAP]   Pape, A. L., Lecanu, J., 3D Navier-Stokes Computations of a Stall-Regulated Wind Turbine, Wind Energ. 2004; 7:309-324

[2005HOU]   Houghton, E. L., Carpenter, P. W., Aerodynamics for Engineering Students, Fifth Edition, Elsevier Butterworth-Heinemann, 2005

[2005TON]   Tongchitpakdee, C., Benjanirat, S., Sankar, L. N., Numerical Simulation of the Aerodynamics of Horizontal Axis Wind Turbines under Yawed Flow Conditions, School of Aerospace Engineering, Georgia Institute of Technology, Atlanta, 2005

[2006CEL]   Celić, A., Hirschel, E. H., Comparison of Eddy-viscosity Turbulence Models in Flows with Adverse Pressure Gradients, Universität Stuttgart, Germany, 2006

[2006CEN]   Cencelli, N.A., Aerodynamic Optimisation of a Small-Scale Wind Turbine Blade for Low Windspeed Conditions, Master's Thesis, Department of Mechanical Engineering, University of Stellenbosch, 2006

[2006CHA]   Chao, D. D., Dam, C. P., Wing Drag Prediction and Decomposition, Journal of Aircraft, Vol. 43, No. 1, 2006

[2006COE]   Coertzer, E., H., Designing and Building of a Horizontal-Axis Model Turbine for a Solar Chimney, Final Year Project, Department of Mechanical Engineering, University of Stellenbosch, 2006

[2006FLU]   Fluent 6.3, Documentation, Fluent Inc., Lebanon, USA, 2006

[2006YAM]   Yamazaki, W., Matsushima, K., Nakahashi, K., Unstructured Mesh Drag Prediction Based on Drag Decomposition, European Conference on Computational Fluid Dynamics, 2006

[2007AUT]   AutoGrid™ v8, Documentation v8b, NUMECA International, Brussels, Belgium, 2007

[2007CFV]   CFView™ v8, Documentation v8a, NUMECA International, Brussels, Belgium, 2007

[2007FER]   Ferrer, E., Munduate, X., Wind Turbine Blade Tip Comparison using CFD, Journa of Physics: Conference Series 75 012005, 2007

[2007FIN]   FINE™/Turbo v8, Documentation v8a, NUMECA International, Brussels, Belgium, 2007

[2007GIJ]   Gijs, A. M., The Lanchester-Betz-Joukowsky Limit, Wind Energ., 2007; 10:289-291

[2007MEN]   Meng, F., van Rooij, P., CFD Investigation with respect to Model Sensitivity for the Non-Rotating Flow around the NREL Phase VI Blade, Proceedings of the European Wind Energy Conference EWEC, 2007

[2007REF]   Renewable energy focus, Patently Innovative, Elevier Ltd, (www.renewableenergyfocus.com), March-April 2007

[2007SCH]   Schmitt, S., Qfinsoft (Pty) Ltd, South Africa (private communication), 2007

[2007VAL]   Valerio, V., Huang, G., Bradshaw, P., Numerical Study of Stress-Transport Turbulence Models: Implementation and Validation Issues, Computers & Fluids 36, 1373–1383, 2007

[2007VER]   Versteeg, H. K., Malalasekera, W., An Introduction to Computational Fluid Dynamics – The Finite Volume Method 2nd Edition, Pearson Education Limited, England, 2007

[2008DEK]   De Kock, D., Director of Qfinsoft (Pty) Ltd, South Africa (private communication), 2008

[2008FLU]   Fluent 12.0, Documentation, Fluent Inc., Lebanon, USA, 2008

[2008HIL]   Hildebrandt, T., NUMECA – Ingenieurbüro, Altdorf b. Nürnberg, Germany, (private communication), 2008

[2008HOU]   Houkema, M., Siccama, N. B., Lycklama à Nijeholt, J. A., Komen, E. M. J., Validation of the CFX4 CFD Code for Containment Thermal-Hydraulics, Nuclear Engineering and Design 238 (2008) 590–599

[2008RUM]   Rumsey, C. L., Spalart, P. R., Turbulence Model Behavior in Low Reynolds Number Regions of Aerodynamic Flowfields, AIAA-2008-4403, 2008

[2008YAM]   Yamazaki, W., Matsushima, K., Nakahashi, K., Drag Prediction, Decomposition and Visualization in Unstructured Mesh CFD Solver of TAS-Code, Int. J. Numer. Meth. Fluids, 57:417–436, 2008

A. Discussion of Base Study

A brief discussion of the base study in which the wind turbine blade geometry was generated is presented.

The main objective of Cencelli's MSc [2006CEN] was to conduct the analytical design of a small scale, stall regulated, horizontal axis wind turbine blade for low wind speed conditions. The design problem was divided into the two-dimensional optimisation of the airfoils used at radial stations, and the three-dimensional optimisation of the geometric features of the wind turbine rotor.

The global objective of the project was to obtain high C_P values over the design wind speed range. This was quantified by $C_{P,\mathrm{object}}$, which is the weighted sum of C_P at each design wind speed.

The radius and the rotational speed of the rotor are 3.7 m and 80 rpm, respectively (considered as constants). Design wind speed range is from 5 to 7 m/s, with a Weibull distribution (5.5 m/s having the highest weighting).

Four radial stations were selected for the two-dimensional optimisation. These stations are located at 20 % (root), 50 % (mid), 75 % (semi) and 90 % (tip) of rotor radius (R_{rotor}). The airfoil profiles of these stations were designed implementing optimisation methods which incorporated the two-dimensional airfoil analysis program XFOIL. The optimisation program, VisualDOC, drove the analysis program to generate the airfoil profiles with optimum aerodynamic characteristics. These characteristics are the maximum coefficient of lift ($C_{L,max}$), the relevant angle of attack and the summated lift-to-drag ratio (L/D_{area}). By blending various standard airfoil profiles a new optimal profile was fashioned for each radial station.

The chord length and pitch angle distribution were the variables altered with the optimisation of the geometric features of the wind turbine rotor to obtain optimal rotor performance. Optimal performance was quantified by the global objective.

From the base study the following data was presented:

- Blade section profiles at four stations.
- Pitch angle and chord distribution.

Models were generated from this acquired data. A summary of the wind turbine rotor specifications are given in Table A.1. The profiles of the blade sections are shown in Figure A.1.

Table A.1: Summary of the wind turbine rotor specifications

Rotor radius	3.7	m
Hub radius	0.37	m
Rotational speed	80	rpm
Wind speed range (Weibull weighting distribution)	5 to 7	m/s
Wind speed with highest weighting	5.5	m/s

Profile section	Root	Mid	Semi	Tip
Location along rotor radius [%]	20	50	75	95
Location along rotor radius [m]	0.74	1.85	2.78	3.52
Pitch angle [°]	13.2	2.6	0.3	-3.1
Chord [m]	0.711	0.456	0.375	0.335
Thickness [m]	0.141	0.075	0.057	0.054
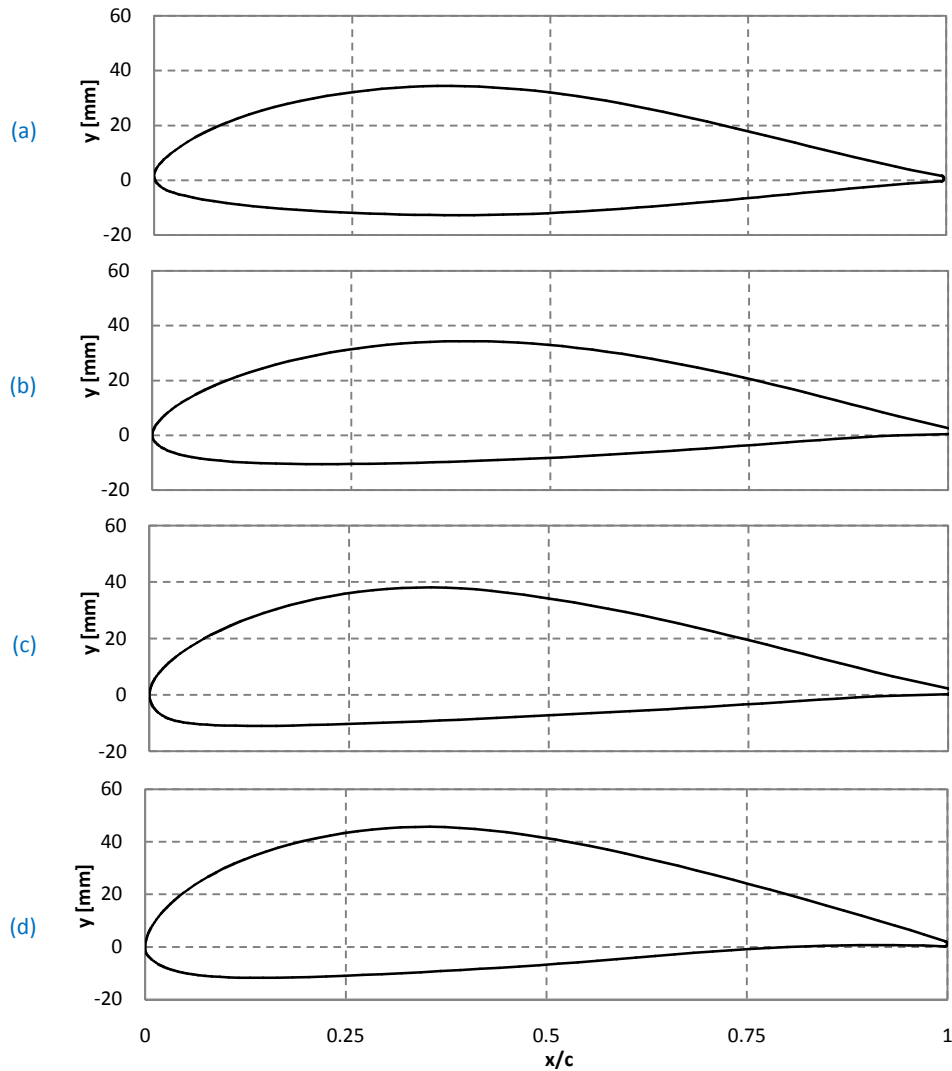
Figure A.1: Profile of the (a) tip, (b) semi, (c) mid and (d) root blade sections

B. Calculations

B.1 Scale Factors

The calculations used to determine the scale factors of the four models used for the two-dimensional wind tunnel testing of Chapter 3 are now presented.

From the axial and tangential velocity components, the relative velocity is calculated:

$$V_{rel} = \sqrt{V_a^2 + V_t^2} \tag{B.1}$$

V_a is taken as the wind speed with the highest Weibull weighting, 5.5 m/s. V_t is calculated as follows:

$$V_t = r\Omega \tag{B.2}$$

where r and Ω are the radius and the rotational speed in rad/s, respectively.

Equation (B.1) and (B.2) are used to calculate the respective Reynolds numbers (with and without induction factors), Table B.1.

B.1.1 Required Velocities

From the Reynolds numbers (with induction factor), the required free stream velocities for the wind tunnel testing are calculated:

$$V = \frac{Re \cdot v}{c} \tag{B.3}$$

where v and c are the kinematic viscosity and chord length, respectively. The v of air at 20 °C is used, 1.4E-05. The respective $V's$ are presented in Table B.1.

B.1.2 Wind Tunnel Blockage

From the cross-sectional area of the test section of the wind tunnel (0.104 m^2), the allowable blockage stipulated by [1999BAR] (7.5 %), and the stipulated chord lengths of the blade sections (Table A.1) the maximum angles of attack are calculated, Table B.1.

Table B.1: Velocity data and Reynolds number with without induction factor

Blade section	Root	Mid	Semi	Tip
V_t [m/s]	6.2	15.5	23.3	29.5
V_{rel} [m/s]	8.3	16.5	23.9	30.0
Reynolds number (no induction factor)	4.21E+05	5.36E+05	6.40E+05	7.17E+05
Reynolds number (with induction factor)	3.59E+05	4.75E+05	5.69E+05	6.39E+05
V [m/s]	7.1	14.6	21.3	26.7
$\pm \alpha_{max}$	8.4	13.1	16.0	18.0

It is evident from Table B.1 that certain criteria stipulated in Section 3.1.2 are violated. Hence, scale factors need to be considered. The influence of the scale factors on relevant parameters was investigated; the findings are presented in Table B.2 and Table B.3. The upper limit for the angle of attack range, 20 ° is used in determining an acceptable scale factor. Highlighted cells indicate violation of the stipulated criterion.

Table B.2: Summary of scale factor investigation (V and $\pm \alpha_{max}$)

Blade Section	Root		Mid		Semi		Tip	
Scale factors	V [m/s]	$\pm \alpha_{max}$ [°]	V [m/s]	$\pm \alpha_{max}$ [°]	V [m/s]	$\pm \alpha_{max}$ [°]	V [m/s]	$\pm \alpha_{max}$ [°]
0.25	28	36	58	65	85	> 90	107	> 90
0.375	19	23	39	37	57	47	71	55
0.5	14	17	29	27	43	34	53	38
0.625	11	13	23	21	34	26	43	30
0.75	9	11	19	18	28	22	36	24
1	7	8	15	13	21	16	27	18

Table B.3: Summary of scale factor investigation (c and t)

Blade Section	Root		Mid		Semi		Tip	
Scale factors	c [mm]	t [mm]	c [mm]	t [mm]	c [mm]	t [mm]	c [mm]	t [mm]
0.25	178	35	114	19	94	14	84	14
0.375	267	53	171	28	141	21	126	20
0.5	356	71	228	38	188	29	168	27
0.625	444	88	285	47	234	36	209	34
0.75	533	106	342	56	281	43	251	41
1	711	141	456	75	375	57	335	54

Note: t is the maximum thickness

Table B.2 and Table B.3 are used to identify acceptable scale factors for the respective blade sections. It was found that the material width was the limiting factor. The respective scale factors identified are presented in Table 2.

B.2 Sample Calculations for Effects of Pressure and Velocity Gradients

The flow was found to be essentially two-dimensional. Hence, the pitch angle(s) are ignored. The yaw angle is adjusted with the following equation [1981SIT]:

$$\epsilon = 13.2 \frac{d_p}{P_{tot,probe}} \left(\frac{d(P_{tot,probe})}{dn} \right)$$

(B.4)

where ϵ is error in degrees , d_p is the probe diameter and dn is in the traverse direction

The steepest pressure and velocity gradients were found with the wind tunnel testing of the tip section. Hence, this case is considered. The tested AOA considered is 0 ° as it proved to give the best goodness of fit results (Table B.4) of the AOA cases.

$\left(\frac{d(P_{tot,probe})}{dx} \right)$ is found by calculating the first derivative of the curve fitted through the experimental data, Figure B.1. The Gaussian curve fit type is utilized.
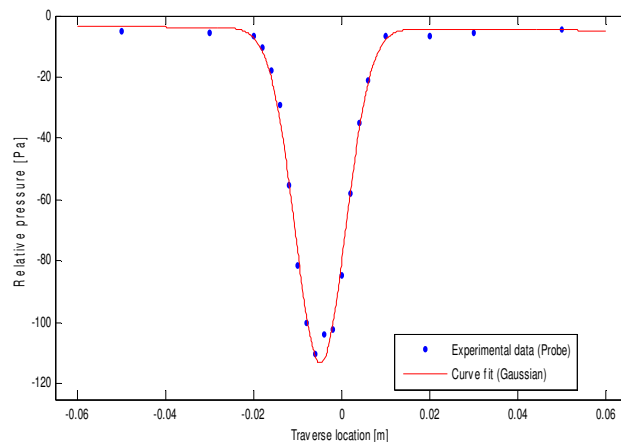
Figure B.1: Total pressure of the probe over wake relative to the total pressure of Pitot-static probe (tip section (α = 0°))

The goodness of fit analysis of the Gaussian type fit applied to experimental data is presented in Table B.4, below.

Table B.4: Goodness of fit analysis of Gaussian curve fit used to obtain $\left(\frac{d(P_{tot,probe})}{dx}\right)$

AOA case	α = 0°	α = 15°
SSE	175.6	1.72E+04
R-square	0.994	0.946
Adjusted R-sqaure	0.992	0.936
RMSE	2.041	25.72

As mentioned, the probe diameter is 4 mm. The respective ϵ for the yaw angle of the test case is presented in Table B.5, below.

Table B.5: Correction of tip section's wind tunnel test yaw angle (α=0°)

Traverse locations [mm]	$\left(\frac{d(P_{tot,probe})}{dx}\right)$ [Pa/m]	$P_{tot,probe}$ [Pa]	ϵ [°]
-50	-10	1.0129E+05	-5.E-06
-30	-15	1.0129E+05	-8.E-06
-20	-1502	1.0129E+05	-8.E-04
-18	-3103	1.0129E+05	-2.E-03
-18	-3103	1.0127E+05	-2.E-03
-16	-5548	1.0127E+05	-3.E-03
-14	-8494	1.0126E+05	-4.E-03
-12	-10953	1.0125E+05	-6.E-03
-6	-3771	1.0125E+05	-2.E-03
-4	2840	1.0125E+05	1.E-03
-2	8458	1.0125E+05	4.E-03
0	11339	1.0126E+05	6.E-03
2	11159	1.0126E+05	6.E-03
4	8881	1.0127E+05	5.E-03
6	5928	1.0127E+05	3.E-03
10	1656	1.0129E+05	9.E-04
20	-6	1.0129E+05	-3.E-06
30	-12	1.0129E+05	-6.E-06
50	-13	1.0129E+05	-7.E-06

As expected, the highest value of ϵ is found at the wake peak. From Table B.5 the effects of the pressure and velocity gradients have negligible effect on the yaw measurement of the probe.

B.3 Grid Sensitivity Analysis

The grid point spacing of the three grids differ from each other by a factor of two. If it is assumed that the error of the respective results is proportional to the grid spacing to some power n, then the result of a grid with infinite number of grid points can be determined from the three grid's results.

The order of the numerical scheme n is calculated as follows:

$$n = \log_2 \left[\frac{T_{q,medium} - T_{q,rough}}{T_{q,fine} - T_{q,medium}} \right] = 0.91 \tag{B.2}$$

The T_q simulated on a grid with infinite number of grid points is given by

$$T_{q,infinite} = T_{q,fine} + \frac{T_{q,fine} - T_{q,medium}}{2^n - 1} = 235.6 \; Nm \tag{B.3}$$

B.4 Estimation of Discretization Error

Define a representative grid size h, for three-dimensional calculations

$$h = \left[\frac{1}{N}\right]^{1/3}$$

(B.4)

where N is the number of cells

Let $h_1 < h_2 < h_3$ then the grid refinement factor r is calculated from

$$r_{21} = \frac{h_2}{h_1}$$
$$r_{32} = \frac{h_3}{h_2}$$

(B.5)

The apparent order p is calculated with

$$p = \frac{1}{\ln(r_{21})}\left|\ln\left|\frac{\epsilon_{32}}{\epsilon_{21}}\right| + q(p)\right|$$

(B.6)

$$q(p) = \ln\left(\frac{r_{21}^p - s}{r_{32}^p - s}\right)$$

(B.7)

$$s = 1 \cdot sign\left(\frac{\epsilon_{32}}{\epsilon_{21}}\right)$$

(B.8)

where $\epsilon_{32} = T_{q,rough}/T_{q,medium}$, $\epsilon_{21} = T_{q,medium}/T_{q,fine}$. Iteration is required to calculate p.

Calculate the extrapolated values from

$$T_{q,ext}^{21} = \frac{(r_{21}^p T_{q,fine} - T_{q,medium})}{(r_{21}^p - 1)}$$

(B.9)

Calculate the approximate relative error:

$$e_a^{21} = \left|\frac{T_{q,fine} - T_{q,medium}}{T_{q,fine}}\right|$$

(B.10)

The fine grid index is calculated from

$$GCI_{fine}^{21} = \frac{1.25 e_a^{21}}{r_{21}^p - 1}$$

(B.11)

C. Five-Hole Probe Procedure

The procedure used to obtain the flow parameters, from the experimental data is presented in this section. The output flow parameters are the total and static pressure, the total velocity and the yaw angle. From the calibration data the pressure coefficients are calculated (pitch angle = 0 °) with varying yaw angle:

$$\bar{P} = \frac{P_2 + P_3 + P_4 + P_5}{4} \tag{C.1}$$

$$C_{P_{yaw}} = \frac{P_4 - P_5}{P_1 - \bar{P}} \tag{C.2}$$

$$C_{P_{static}} = \frac{\bar{P} - P_{static,pitot}}{P_1 - \bar{P}} \tag{C.3}$$

$$C_{P_{total}} = \frac{P_1 - P_{tot,pitot}}{P_1 - \bar{P}} \tag{C.4}$$

The coefficients at various yaw angles implementing the calibration data for free stream wind speed of 29.5 m/s are presented in Figure C.1.
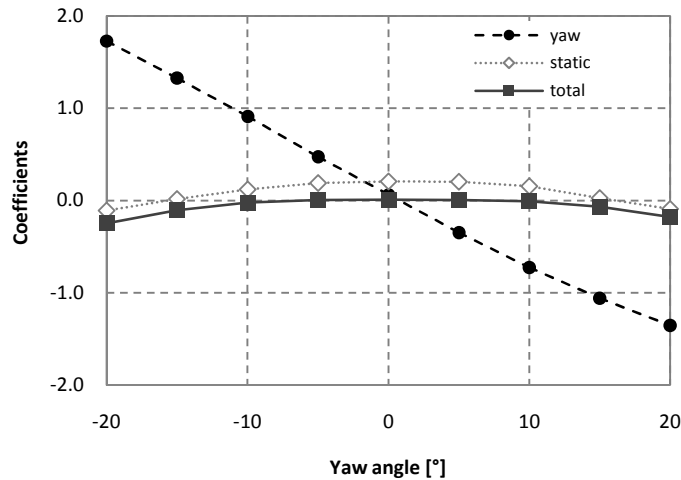
Figure C.1: Coefficients obtained with calibration data

By inputting the wake traverse data into Equation (C.2), $C_{P_{yaw}}$ is calculated. From Figure C.1, the corresponding yaw angle is determined with curve-fitting. By manipulating Equation (C.2) and (C.3), the static and the total pressure in the wake are calculated:

$$P_{static,wake} = \bar{P} - C_{P_{static}}(P_1 - \bar{P}) \qquad \text{(C.5)}$$

$$P_{total,wake} = P_1 - C_{P_{total}}(P_1 - \bar{P}) \qquad \text{(C.6)}$$

D. Tabulated Experimental Data

The experimental data obtained from the two-dimensional wind tunnel tests of Chapter 3 are analyzed, as described in Section 3.3.6. These results are presented in this section.

Table D.1: Drag coefficients of root and mid blade sections obtained with 2-D EFD modelling

Blade Section	Root			Mid		
AOA [°]	C_{D_p}	$C_{D_{Jones}}$	$C_{D_{Maskel}}$	C_{D_p}	$C_{D_{Jones}}$	$C_{D_{Maskel}}$
0	0.0146	0.02	0.0204	0.0015	0.0167	0.0166
7	0.0448					
9				0.0728		
10	0.0475	0.0244	0.0241			
12				0.0744	0.0232	0.021
13	0.0965					
15				0.1402		
16	0.0917					

Table D.2: Drag coefficients of semi and tip blade sections obtained with 2-D EFD modelling

Blade Section	Semi			Tip		
AOA [°]	C_{D_p}	$C_{D_{Jones}}$	$C_{D_{Maskel}}$	C_{D_p}	$C_{D_{Jones}}$	$C_{D_{Maskel}}$
0	0.0149	0.0161	0.0161	0.0146	0.0119	0.0119
7	0.0348			0.0275		
9						
10	0.0322			0.0231		
15	0.0659	0.0119	0.0119	0.0647	0.104	0.102
20				0.3331		

Table D.3: Lift coefficients of the four blade sections obtained with 2-D EFD modelling

AOA [°]	Blade Section			
	Root	Mid	Semi	Tip
0	0.636	0.346	0.374	0.356
7	1.347		1.006	1.062
9		1.335		
10	1.632		1.320	1.147
12		1.562		
13	1.677			
15		1.480	1.318	1.045
16	1.728			
20				0.832

Table D.4: Pressure coefficient distribution over root blade section surface (AOA indicated in bold)

	Suction						Pressure				
x /c	**0**	**7**	**10**	**13**	**16**	x/c	**0**	**7**	**10**	**13**	**16**
0.000	0.799	0.638	-0.182	-0.727	-2.115	0.000	0.799	0.638	-0.182	-0.727	-2.115
0.024	-0.437	-1.157	-2.054	-2.404	-3.219	0.024	-0.437	0.858	0.999	0.997	0.881
0.054	-0.447	-1.670	-2.440	-2.689	-3.231	0.054	-0.447	0.538	0.796	0.865	0.958
0.094	-0.454	-1.893	-2.525	-2.734	-3.082	0.094	-0.454	0.333	0.574	0.649	0.787
0.146	-0.306	-2.099	-2.578	-2.693	-2.852	0.146	-0.306	0.282	0.470	0.534	0.658
0.213	-0.193	-2.099	-2.461	-2.522	-2.564	0.213	-0.193	0.249	0.403	0.445	0.543
0.301	-0.093	-2.018	-2.301	-2.291	-2.027	0.301	-0.093	0.220	0.342	0.373	0.443
0.384	-0.035	-1.797	-2.044	-1.919	-1.521	0.384	-0.035	0.210	0.308	0.329	0.378
0.468	-0.002	-1.288	-1.371	-1.349	-0.987	0.468	-0.002	0.199	0.277	0.290	0.321
0.552	0.034	-0.948	-0.996	-0.958	-0.679	0.552	0.034	0.195	0.255	0.257	0.265
0.635	0.085	-0.674	-0.666	-0.651	-0.595	0.635	0.085	0.210	0.254	0.242	0.233
0.719	0.158	-0.416	-0.403	-0.405	-0.578	0.719	0.158	0.236	0.263	0.237	0.193
0.803	0.194	-0.208	-0.174	-0.224	-0.458	0.803	0.194	0.233	0.240	0.219	0.229

Table D.5: Pressure coefficient distribution over mid blade section surface (AOA indicated in bold)

	Suction					Pressure			
x /c	**0**	**9**	**12**	**15**	x/c	**0**	**9**	**12**	**15**
0.000	0.799	0.327	-0.892	-1.097	0.000	0.408	0.327	-0.892	-1.097
0.047	-0.437	-2.017	-2.912	-2.960	0.036	0.061	0.748	0.945	0.956
0.087	-0.447	-2.057	-2.703	-2.676	0.081	-0.322	0.543	0.747	0.767
0.135	-0.454	-2.114	-2.633	-2.520	0.124	-0.624	0.452	0.635	0.655
0.185	-0.306	-2.033	-2.445	-2.353	0.159	-0.795	0.407	0.569	0.623
0.248	-0.193	-2.005	-2.311	-2.106	0.231	-0.944	0.354	0.489	0.495
0.305	-0.093	-1.864	-2.066	-1.782	0.299	-0.977	0.302	0.412	0.421
0.394	-0.035	-1.591	-1.581	-1.386	0.388	-0.915	0.269	0.355	0.351
0.479	-0.002	-1.129	-1.176	-0.925	0.473	-0.775	0.293	0.359	0.341
0.563	0.034	-0.815	-0.786	-0.617	0.560	-0.535	0.249	0.295	0.268
0.649	0.085	-0.537	-0.478	-0.480	0.650	-0.353	0.195	0.221	0.176
0.738	0.158	-0.341	-0.333	-0.432	0.738	-0.227	0.189	0.192	0.127
0.842	0.194	-0.110	-0.154	-0.380	0.825	-0.068	0.259	0.163	0.056

Table D.6: Pressure coefficient distribution over semi blade section surface (AOA indicated in bold)

	Suction					Pressure			
x /c	**0**	**7**	**10**	**15**	x/c	**0**	**7**	**10**	**15**
0.000	0.839	0.245	0.839	-3.640	0.000	0.839	0.245	0.839	-3.640
0.018	0.550	-1.105	0.550	-3.696	0.018	-0.752	0.761	-0.752	0.953
0.048	0.059	-1.306	0.059	-2.704	0.050	-0.645	0.431	-0.645	0.896
0.085	-0.231	-1.367	-0.231	-2.364	0.087	-0.505	0.303	-0.505	0.743
0.137	-0.457	-1.417	-0.457	-2.034	0.135	-0.388	0.231	-0.388	0.605
0.228	-0.674	-1.405	-0.674	-1.646	0.208	-0.271	0.185	-0.271	0.490
0.292	-0.734	-1.336	-0.734	-1.387	0.294	-0.189	0.142	-0.189	0.371
0.386	-0.788	-1.248	-0.788	-1.081	0.381	-0.155	0.120	-0.155	0.290
0.471	-0.707	-1.107	-0.707	-0.722	0.467	-0.117	0.109	-0.117	0.228
0.553	-0.640	-0.841	-0.640	-0.528	0.558	-0.079	0.106	-0.079	0.172
0.646	-0.520	-0.635	-0.520	-0.447	0.647	-0.029	0.116	-0.029	0.129
0.739	-0.315	-0.420	-0.315	-0.461	0.736	0.011	0.122	0.011	0.077
0.821	-0.149	-0.199	-0.149	-0.450	0.822	0.090	0.147	0.090	0.046

Table D.7: Pressure coefficient distribution over tip blade section surface (AOA indicated in bold)

	Suction						Pressure				
x /c	**0**	**7**	**10**	**15**	**20**	x/c	**0**	**7**	**10**	**15**	**20**
0.000	0.927	0.011	-1.184	-2.737	-0.527	0.000	0.927	0.011	-1.184	-2.737	-0.527
0.034	0.035	-1.548	-2.239	-2.531	-0.852	0.043	-0.273	0.680	0.850	0.944	0.908
0.073	-0.312	-1.636	-2.129	-2.320	-0.793	0.085	-0.246	0.480	0.656	0.795	0.764
0.121	-0.620	-1.761	-2.136	-2.048	-0.792	0.135	-0.237	0.355	0.505	0.637	0.622
0.179	-0.775	-1.697	-1.878	-1.656	-0.800	0.183	-0.228	0.282	0.409	0.529	0.518
0.230	-0.838	-1.589	-1.704	-1.338	-0.791	0.238	-0.223	0.213	0.322	0.425	0.409
0.290	-0.886	-1.508	-1.551	-1.011	-0.792	0.302	-0.223	0.147	0.239	0.320	0.302
0.379	-0.897	-1.444	-1.389	-0.575	-0.822	0.388	-0.230	0.081	0.148	0.199	0.173
0.466	-0.793	-1.111	-0.881	-0.468	-0.835	0.483	-0.178	0.066	0.107	0.122	0.079
0.557	-0.684	-0.829	-0.492	-0.465	-0.848	0.567	-0.132	0.074	0.094	0.079	0.027
0.642	-0.391	-0.558	-0.316	-0.493	-0.854	0.653	-0.104	0.063	0.056	0.007	-0.066
0.736	-0.214	-0.296	-0.327	-0.513	-0.853	0.749	-0.002	0.085	0.050	-0.033	-0.132
0.822	-0.072	-0.112	-0.320	-0.522	-0.828	0.839	0.097	0.100	0.029	-0.106	-0.228

E. Grid Convergence Study

The results of the grid convergence study are presented in Table E.1. For brevity, only the results of the first three turbulence models presented in Section 4.1.3.2 are given. The latter two, namely the $k\varepsilon$-realizable and Tran-SST turbulence models results were similar. It was found that the $k\varepsilon$-standard turbulence model was the most sensitive to the varying surface grid density. The force coefficients of the root blade section obtained with this model on the various grids are presented in Figure E.1, below.

(a)   (b)
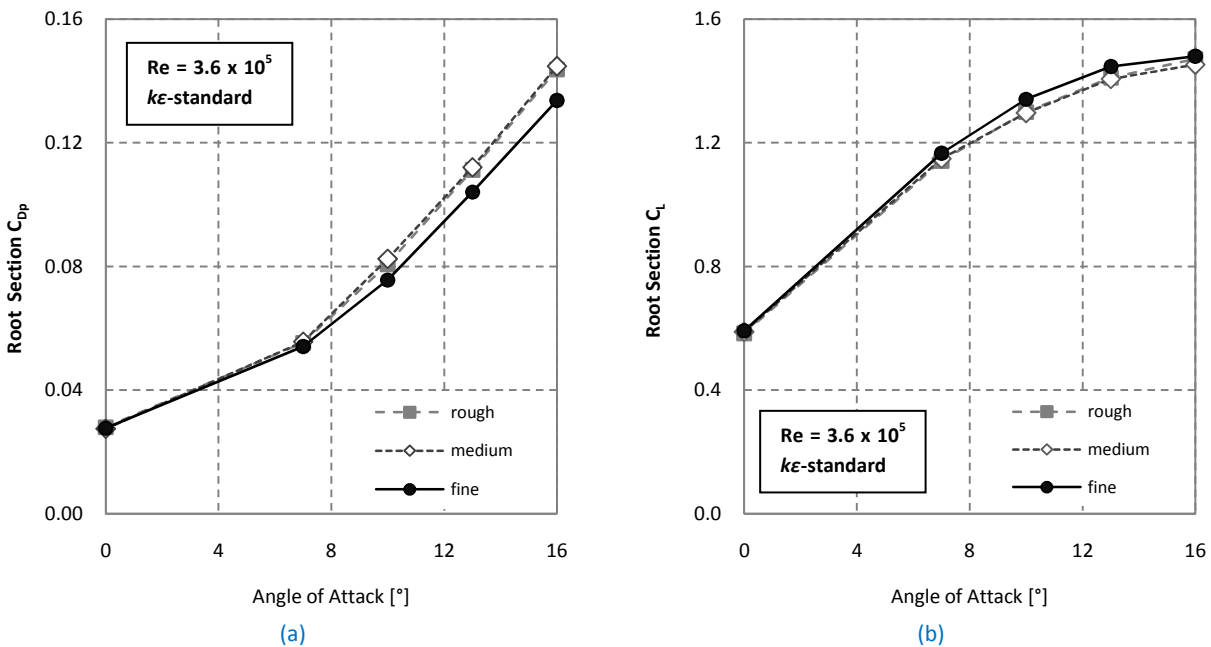
Figure E.1: Force coefficients, (a) pressure drag and (b) lift ($k\varepsilon$-standard turbulence model)

The results of the simulations utilizing the rough and medium grid are essentially the same. However, the fine grid computations differ from the rougher grid results. This could be due to numerical error. It should be noted that the $k\varepsilon$-standard turbulence model was an extreme case. The influence of the surface grid density on the other turbulence models was significantly less.

Table E.1: Lift and drag coefficients used for grid convergence study

Rough (Highest aspect ratio is 100)

	Drag									Lift		
	Spalart-Allmaras			k-ω SST			k-ε Standard			Spalart-Allmaras	k-ω SST	k-ε Standard
AOA [°]	Pressure	Viscous	Total	Pressure	Viscous	Total	Pressure	Viscous	Total	Pressure Total	Pressure Total	Pressure Total
0	.0107	.0116	.0223	.0100	.0107	.0207	.0154	.0126	.0280	.574	.532	.583
7	.0373	.0114	.0487	.0375	.0106	.0481	.0426	.0127	.0554	1.109	1.032	1.142
10	.0625	.0110	.0735	.0603	.0101	.0704	.0685	.0123	.0807	1.237	1.126	1.300
13	.0910	.0103	.1013	.0976	.0094	.1070	.0996	.0116	.1112	1.253	1.057	1.411
16	.1230	.0095	.1325	.1330	.0087	.1417	.1331	.0108	.1438	1.204	.996	1.472

Medium (Highest aspect ratio is 75)

	Drag									Lift		
	Spalart-Allmaras			k-ω SST			k-ε Standard			Spalart-Allmaras	k-ω SST	k-ε Standard
AOA [°]	Pressure	Viscous	Total	Pressure	Viscous	Total	Pressure	Viscous	Total	Pressure Total	Pressure Total	Pressure Total
0	.0105	.0116	.0221	.0096	.0107	.0203	.0149	.0126	.0275	.577	.528	.589
7	.0384	.0114	.0498	.0383	.0106	.0488	.0429	.0127	.0556	1.111	1.025	1.149
10	.0639	.0110	.0749	.0652	.0101	.0753	.0702	.0123	.0825	1.223	1.098	1.297
13	.0929	.0103	.1031	.0977	.0094	.1071	.1005	.0116	.1121	1.251	1.074	1.406
16	.1265	.0095	.1360	.1333	.0087	.1419	.1340	.0108	.1448	1.215	1.016	1.453

Fine (Highest aspect ratio is 50)

	Drag									Lift		
	Spalart-Allmaras			k-ω SST			k-ε Standard			Spalart-Allmaras	k-ω SST	k-ε Standard
AOA [degree]	Pressure	Viscous	Total	Pressure	Viscous	Total	Pressure	Viscous	Total	Pressure Total	Pressure Total	Pressure Total
0	.0108	.0116	.0224	.0099	.0107	.0206	.0151	.0126	.0277	.582	.534	.591
7	.0370	.0114	.0485	.0373	.0106	.0479	.0413	.0127	.0541	1.126	1.035	1.166
10	.0586	.0109	.0695	.0624	.0101	.0725	.0634	.0122	.0757	1.253	1.112	1.342
13	.0876	.0102	.0977	.0957	.0093	.1050	.0926	.0115	.1041	1.256	1.064	1.447
16	.1204	.0093	.1297	.1294	.0085	.1380	.1231	.0106	.1337	1.206	1.017	1.480